CONTROLLED RELEASE OF GLP-1 FROM AFFINITY-BASED PROTEIN MICROSPHERES AND QUANTITATIVE ANALYSIS OF THE ROLE OF FIBER LENGTH ON PHAGOCYTOSIS AND INFLAMMATORY RESPONSE BY MACROPHAGES

A Dissertation
Presented to
The Academic Faculty

by

Trudy J Padmore

In Partial Fulfillment
of the Requirements for the Degree
Doctor of Philosophy in the
School of Chemical & Biomolecular Engineering

Georgia Institute of Technology
December 2016

CONTROLLED RELEASE OF GLP-1 FROM AFFINITY-BASED

PROTEIN MICROSPHERES

AND

QUANTITATIVE ANALYSIS OF THE ROLE OF FIBER LENGTH ON PHAGOCYTOSIS AND INFLAMMATORY RESPONSE BY MACROPHAGES

Approved by:

Dr. Julie A. Champion, Advisor
School of Chemical & Biomolecular Engineering
Georgia Institute of Technology

Dr. Andrés García
School of Mechanical Engineering
Georgia Institute of Technology

Dr. Sven Behrens
School of Chemical & Biomolecular Engineering
Georgia Institute of Technology

Dr. Todd McDevitt
Dept. of Bioengineering & Therapeutic Sciences
Gladstone Institute, University of California San Francisco

Dr. Andreas Bommarius
School of Chemical & Biomolecular Engineering
Georgia Institute of Technology

Date Approved: November 14, 2016

Dedicated to my family

ACKNOWLEDGEMENTS

I would like to thank my thesis advisor, Dr. Julie Champion. Her support, encouragement, and advice were invaluable to the completion of my thesis work. I thank my committee members, Dr. Sven Behrens, Dr. Andreas Bommarius, Dr. Andrés García, and Dr. Todd McDevitt for their patience and feedback.

I am grateful to my Champion Lab members who have shared many late-night existential crises, Anusha Garapaty, Tim Chang, Kevin Ling, Adam Caparco, Alexis Tsoras. We've fostered great friendships over the years.

I would also like to express gratitude to my collaborators Dr. Leonid Turkevich and Carahline Stark for their project assistance. Thanks also to David Belair for his support with the mathematical modeling of peptide release.

Finally, I am especially grateful to my family, and my close friends, for keeping me uplifted with their unwavering support and love.

TABLE OF CONTENTS

LIST OF TABLES

LIST OF FIGURES

LIST OF SYMBOLS AND ABBREVIATIONS

BLI	BioLayer Interferometry
BTC-6	Beta-TC-6 mouse pancreatic insulinoma
CD	circular dichroism
Ci	concentration for species i
COX-2	Cylcooxygenase 2
Di	Diffusivity of species i
DLS	dynamic light scattering
DMSO	dimethyl sulfoxide
ECM	extracelluar matrix
ELP	Elastin-like polypeptides
FBS	fetal bovine serum
GLP-1	Glucagon-like peptide-1
GST	Glutathione S. Transferase
IL-1a	Interleukin-1alpha
IPTG	isopropyl β-D-1-thiogalactopyranoside
ITC	Inverse Transition Cycling
kf	Association contant
kr	Dissociation constant
L	characteristic length for systems
Lc	critical length

LDH	Lactate Dehydrogenase
LPS	Lipopolysaccaride
PBS	PBS phosphate buffered saline
PGE2	Prostaglandin E2
ROS	Reactive Oxygen Species
SBP	SH3 binding peptide
SDS-PAGE	sodium dodecyl sulfate polyacrylamide gel electrophoresis
SEM	Scanning Electron Microscopoy
SH3	Src Homology 3 Domain
TNF-a	Tumor Necrosis Factor-alpha
Tt	Transition Temperature

SUMMARY

CONTROLLED RELEASE OF GLP-1 FROM AFFINITY-BASED PROTEIN MICROSPHERES

Peptide drugs possess high specificity and potency compared to small molecule drugs. However they are plagued by rapid clearance and degradation *in vivo*. Type 2 diabetes affects approximately 26-27 million American adults and is projected to increase to 300 million globally by 2025. Glucagon-like peptide-1 (GLP-1), stimulates the glucose-dependent secretion of insulin from pancreatic beta cells, and serves as the main peptide therapeutic treatment for Type 2 diabetes. Bydureon™ is a commercially available formulation of GLP-1 peptide analog encapsulated in PLGA microspheres. The required dose for Bydureon is 14-28 times more than its soluble formulation due in part to the burst release from the PLGA microsphere. Thus controlling the release of the peptide drug is critical for delivery of therapeutically relevant doses and cost reduction. Affinity-based systems are strategically poised to overcome this challenge; the hallmark transient interactions between protein or peptide components allow for sustained release, while avoiding the diffusion-driven burst release of most delivery particles. Varying the strength of affinity interactions, ligand concentration, and system geometry can control the release rates of peptide from affinity-based systems. Here we describe a strategy that uses two binding domains, the Src homology domain 3 (SH3) and the SH3 binding peptide. SH3 was fused to an elastin-like polypeptide (ELP), which exhibits inverse phase transition behavior. SH3 functionalized microspheres were prepared by phase transition of the ELP-SH3 fusion proteins and subsequent crosslinking. The therapeutic

peptide, GLP-1, was modified with three different SH3 binding peptide to facilitate reversible binding to the microspheres and enable sustained release. SH3 binding peptides possessed a range of affinities ((K_D=10^{-6} – 10^{-8} M) that allows for immobilization and subsequent diffusion over several days. Release rates of GLP-1 were strongly dependent on the SH3 binding peptide affinity, with the weaker binder releasing 40% of its total cargo and the stronger binder releasing 20% over a 7-day period. Released GLP-1 stimulated significant increases in Beta cell number. Stimulation of insulin secretion by released GLP-1 was not significant. Use of established mathematical models qualitatively replicated affinity-dependent release trends. However, the model did not correlate well with the experimental release profiles. This can be attributed to the variation in apparent experimental diffusivity from estimated diffusivity, as well as estimation of kinetic parameters. Importantly, an affinity-dependent reduction in the burst release effect typically experienced by encapsulation systems was observed and microsphere preparation occurred under conditions favorable to retention of affinity domain function. These results suggest this system could be useful for sustained delivery of other types of therapeutic peptides modified with SH3 binding peptides.

CHAPTER 1.

INTRODUCTION

1.1 Affinity-Based Systems for Protein and Peptide Release

Since the early 1980s, with the advent of the first recombinant protein drug humulin, an insulin therapeutic, both protein and peptide biologics have gained prominence. This biologics market, valued at $200 billion in 2013, is predicted to expand to over $350 billion by 2019 [1]. Peptides and proteins are selective and potent, representing alternatives to traditional small molecule therapies that are plagued by tolerability and off-target effects. However, these therapeutics are not without its challenges[2]. The development of micro- and nano-scale delivery systems that protect peptide and proteins from degradation while controlling their release within the body has grown concurrently with the biologics market. The need to improve patient compliance through the administration of fewer therapeutic injections, reduce viscosity, and increase drug loading have also been driving forces behind the progression of therapeutic delivery technologies[3]. Platforms in which release is either dependent on polymer degradation or is diffusion-controlled e.g. PLGA have been successful in controlling delivery over long time frames (days-weeks)[4–6], however rapid burst limit them to applications in which high dose effects are tolerable. In stimuli-responsive release, polymers such as poly(N-isopropylacrylamide) (PNIPAm) undergo phase transitioning from low viscosity solutions to gels at temperatures above a lower critical solution temperature (LCST) making them attractive for in situ applications. Within this class are poly(N-vinylcaprolactam) (PVCL), poly(ethylene glycol) (PEG), poly(ethylene oxide) (PEO),

and poly(propylene oxide) (PPO). pH-sensitive swelling or reduction in LCST is imparted by incorporation of ionisable or H-bonding monomer units respectively. While the modularity of stimuli control make this class of polymers attractive for drug delivery applications, the rapid burst experienced when changing stimuli conditions means that more precision in monomer incorporation is required before fine control over release is achieved [7]. Traditional encapsulation systems with biodegradable polymers used in the sustained release of small molecules, are not easily translatable to peptides and proteins[8]. Their formulation typically involves organic solvents and harsh conditions that may lead to the disruption of structure and thus loss of therapeutic function[9]. More favorable alternative delivery systems exploit the non-covalent or affinity interactions between protein domains, protein-peptide domains, or protein- pendant monomer domains on polymers.

Affinity interactions abound in nature. The extracellular matrix (ECM) offers prominent examples of protein-protein interactions. The ECM exploits affinity binding of growth factors to heparin sulfate proteoglycan components to protectively bind and modulate bioavailability [10,11]. Affinity-bound molecules are subsequently released by gradients driven by diffusion, proteolytic activity during matrix remodeling [12], and receptor endocytosis [13].

ECM mimetic delivery focus on protein-peptide interactions to sequester and release growth factors through the incorporation of heparan sulfate biosimilar peptide, heparin, into delivery vehicles. Several drug delivery systems have utilized the binding interactions of heparan sulfate by developing heparinized hydrogels that slows the release of target molecules from the hydrogels. Tuned release of nerve growth factor (NGF) and

vascular endothelial growth factor (VEGF) from hydrogels for tissue repair has been accomplished through heparin-like binding interactions by Sakiyama-Elbert and colleagues [14–16]. Kiick et al has driven assembly of hydrogels through protein and heparin mediate interaction [17].

Protein-peptide interaction systems also incorporate other natural or synthetic affinity partners for slow release, encapsulation, and immobilization. Foo and colleagues designed mixing-induced two-component hydrogels or MITCHs using computationally-derived molecular recognition partner domains that delivered VEGF-mimetic peptide [18]. They controlled release through varying the affinity of the proline-rich peptide. Shoichet et al examined the use of natural Src homology 3 (SH3) domain interactions with two variable binding SH3 binding peptides (SBPs) to control the release of Fibroblast growth factor 2(FGF2) and Chondroitinase ABC (ChABC) proteins [19,20]. Martino et al discovered that growth factors; Brain-derived neurotrophic factor (BDNF), Transforming growth factor β (TGFβ), Bone morphogenetic protein 4 (BMP-4), Insulin like growth factor binding protein 5 (IGFBP-5), Basic fibroblast growth factor (bFGF), and Placenta growth factor (PGF), had varying affinities for the heparin-binding domain of fibrinogen. Distinct release rates of each growth factor were observed when experiments were reproduced on a fibrin matrix [21]. The above examples describe affinity interactions that were either natural or imparted to the protein through fusion with one of the affinity-binding partners. Fusion constructs may suffer from a partial loss of protein function after modification with affinity domains; despite this, protein-peptide interaction systems remain a smart alternative as it reduces interactions between other endogenous proteins and affinity domains on delivery particles. Belair and colleagues recently examined the

reduction of affinity immobilized VEGF (high binding affinity) in the presence of serum due to competition for binding domains by endogenous proteins, however the reduction rate was markedly lesser in comparison to the rates for VEGF-scramble peptide interactions (low binding affinity) [22].

Protein - polymer interactions are also common in delivery system design. Layer by layer (L-b-L) techniques, pioneered by Decher and colleagues [23], have allowed the directed assembly of therapeutic proteins with polymers through interactions between monomer domains. Interactions such as electrostatic, hydrophobic, hydrogen bonding, charge-transfer, and co-ordinate chemistry are non-covalent methods employed in this bottom-up assembly of alternating protein and polymer layers [24]. Lvov and colleagues demonstrated multilayered multicomponent protein assemblies through electrostatic adsorption with alternating charged polymers layers [25]. Caruso et al showed that electrostatic interactions are important to the stepwise assembly of multilayers of biomolecules with polymers on microparticle surfaces [26]. Other interactions such as the reducible disulfide interactions between proteins and polymers also successfully deliver protein therapeutics. For example, Ventura et al developed a delivery method that uses the reversible formation of disulfide bonds between exposed thiols on native protein surfaces and thiols functionalized on polymers. This led to self-assembly of the polymer forming a protective reversible shield around the Caspase protein that preserved protein function [27]. Covalent coupling of proteins to polymers dominates affinity-based drug delivery, since modular control over polymer functionalization can be achieved by changing the ratio of individual components. Peattie et al investigated the effects of reducing heparin quantities

on release rates of growth factors through simple component ratio adjustment in the Hyaluronic acid (HA) copolymerization reaction[28]. On the other hand similar adjustments in purely protein-protein interacting systems may call for extensive re-optimatization of individual components.

Affinity-based systems encompass aspects of all delivery strategies. In recent times, the range of affinities investigated and the tunability of release through variation in affinity, ligand density, and system geometry has deepened our ability to control affinity release systems. Mathematical modeling of release allows for additional examination of the contributions of system components on release rates. Sakiyama-Elbert et al illustrated the complex interaction of affinity release in tandem with enzymatic activity using mathematical models[14]. Belair et al modeled the effects of competitive interactions coupled with release[22]. Additionally, affinity-based delivery have progressed from the early heparin-based ECM mimetics to now include high affinity (K_D = nM) DNA Aptamers for 6-day delivery of Platelet-derived growth factor-BB (PDGF-BB)[29] from functionalized gels. The modularity of the affinity-based platforms has allowed for the delivery of both peptides and higher molecular weight growth factors. Binding matrices ranging from biopolymers fibrin and collagen to polymers such as PEG, PLGA, and HAMC have successfully delivered protein and peptide therapeutics.

In a recent review, Shoichet et al suggested the use of affinity-based systems for the combinatorial delivery of multiple therapeutics in which each therapeutic needs to possess independent release profiles as a promising direction for this emergent technology [30]. Mitragotri and colleagues also proposed the co-delivery of hyaluronidase to address problems associated with high drug viscosity at subcutaneous delivery sites [3].

This proposed system can be used to reduce therapeutic aggregation while controlling the sequential release of hyaluronidase for increased diffusion at the injection site.

In this work we exploit the affinity interactions of known protein and peptide domains to develop a controlled release system for the sustained delivery of a peptide therapeutic. Our system, prepared from the self-assembly of affinity- binding partner domains into microspheres, immobilizes and subsequently releases functionalized therapeutic peptides.

1.2 Motivation & Objectives

With more than 140 peptide drugs in advanced clinical trials[2], pharmaceutical research and development in peptide therapeutics is high. Peptide drugs possess increased specificity and efficacy in comparison to small molecule drugs, and interest in them persists despite the challenges of rapid clearance and proteolytic degradation[9]. To overcome these limitations peptide delivery systems must prolong release while protecting biological activity. Current peptide delivery systems are plagued with rapid burst release due to uncontrolled degradation of polymeric carriers, complex low-scalability encapsulation processes and low loading efficiencies. Here we describe an affinity-mediated delivery system that allows for tunable release of Type 2 diabetes therapeutic peptide through the interactions of peptide-protein binding partner domains. A 2014 report from the Center For Disease Control and Prevention (CDC) estimates that 29.1 million Americans have Type 2 diabetes with adults making up 90% of all diagnosed cases. $245 billion in medical treatment and lost wages has been attributed to Type 2 diabetes treatment [31]. Glucagon-like peptide 1 (GLP-1) stimulates insulin secretion from pancreatic β-cells and is used for treatment of Type 2 diabetes [32]. GLP-1

experiences proteolytic degradation and a 2-minute half-life *in vivo*. Current GLP-1 therapeutics on the market seeks to extend peptide half-life for immediate, once-daily, and once-weekly applications using several strategies. Strategies include; mutation of the amino acid sequence to evade proteolytic degradation (exenatide, lixisenatide), conjugation to larger molecules such as Human serum albumin (HSA) and Immunoglobulin G (IgG) (albiglutide, dulaglutide, liraglutide), as well as encapsulation within biodegradable polymeric microparticles (exenatide-LAR)[33]. Exenatide-LAR (marketed as Bydureon™) is comprised of Exendin-4 encapsulated in PLGA microspheres with a 2mg/ml weekly administered dose, a dose of 14-28 fold more than is required from the soluble twice-daily formulation was needed for similar efficacy from the microspheres. This suggests that a burst release from the PLGA microsphere necessitated high dosing [34]. More control over release is required to reduce microsphere dosage, cost, and injection frequency. In this thesis, I describe a strategy to prolong the release of active Glucagon-like peptide 1 (GLP-1) using Src homology 3 (SH3) domain protein microspheres that binds GLP-1 through affinity-mediated interactions when functionalized with SH3-binding peptides [35]. The system, comprised solely of protein and peptide components, has controlled loading efficiency. Additionally, sequestration is independent of therapeutic peptide hydrophobicity. Through the fusion of the SH3 domain with a self-assembling elastin-like polypeptide [36] we prepared ELP-SH3 microspheres. GLP-1 modified with SH3-binding peptides of micromolar and nano-molar affinities (GLP-1-SBPs) facilitates tunable release from SH3 microspheres. The objectives of this work are preparation of ELP-SH3 microspheres for optimal stability and loading efficiency of GLP-1-SBP, and to examine the release profiles of each GLP-1-

SBP from the same microspheres. We also seek to describe the release profile of multiple GLP-1-SBPs from the same microspheres. Finally, a comparison of a predictive model that uses measured kinetic parameters with the empirical release profiles will be performed.

1.3 Thesis Overview

Achievement of the abovementioned objectives is summarized in the chapters that follow. Chapter 2 describes the design and characterization of the protein and peptide domains used to develop the delivery system. Chapter 3 focuses on the preparation of protein microspheres, retention of function of protein domains after microsphere synthesis, loading efficiency, and quantification of *in vitro* release of peptides from prepared protein microspheres and particle surfaces. Additionally, the ability of the system to stimulate insulin secretion in mouse pancreatic cells *in vitro* is also described. Comparisons of experimental release profiles with those predicted by a mathematical model using measured kinetic parameters are also described in this chapter. Chapter 4 examines the limitations of the current system and provides recommendations for future work, and outlook for potential market translation. Finally, Chapter 5, describes the second project in this thesis work that quantifies the role of fiber length in the inflammatory response of alveolar macrophages. This work seeks to provide an in vitro model for single-parameter contributions to fiber-induced pathogenicity.

CHAPTER 2.

AFFINITY-BINDING PARTNER DOMAINS

Affinity systems that exploit the binding interactions between protein-protein domains for controlling the release of therapeutics have gained prominence in recent times. To achieve sustained release of our target therapeutic, GLP-1, we have identified complementary binding domains, Src Homology 3 (SH3) domain and SH3-binding peptides (SBPs). These SBPs possess a range of binding affinities (10^{-6} – 10^{-8}M) to the SH3 domain. Through functionalization with the SBP partner similar binding interactions can be imparted to GLP-1. The SH3 partner domain is then utilized in preparation of the delivery system on which GLP-1 is loaded and subsequently released.

2.1 Src Homology 3 (SH3) Domain and SH3-binding peptides

In the body signaling is typically facilitated by adaptor proteins that primarily serve as sites for protein-protein interaction. These adaptor proteins contain several protein interaction domains. One such domain is the Src homology 3 (SH3) domain, present in the Mona/Gads adaptor protein among other families of proteins including protein kinases [37,383940]. The β-barrel shape that is characteristic of SH3 domains was identified by Harkiolaki and colleagues to be ubiquitous among adaptor proteins [35]. The authors further demonstrated that the SH3-domain in Mona/Gads possesses high affinities to a short binding sequence on the SLP-76 signal transducer peptide, called the SH3-binding peptide. SH3-binding peptides are proline-rich and contain consensus motifs R-x-x-K [35]

or R-x-x-P-x-x-P [41], where x signifies two guest residues between arginine (R), lysine (K) and proline (P) positions. These peptides were found to bind with varying affinities Kd < μM. The SH3-binding peptide forms a 'clamp-like' shape that cups the Mona/Gads barrel (Figure 2.1). Isothermal titration calorimetry experiments conducted by Harkiolaki and colleagues revealed that modification of residues adjacent to the R-x-x-K motif resulted in changes in the interaction affinities between the peptide and SH3 domain.

Affinity interactions between the SH3 domain and SH3-binding peptide have been replicated with high fidelity in the literature [20]. SH3-binding peptides show similar hierarchy of binding affinities to the SH3 domain, though it has been presented in varied forms. We use these affinity-binding partners because the affinity interactions cover a wide range of affinities and thus can be adapted to our release system as well as for the consistency of affinity data from previous studies.

Figure 2-1 Crystal structure of the SH3 domain located at the C-terminal of Mona/Gads (SH3C--green β-strand) in complex with SH3-binding peptide 2 (orange strands). View looks down the length of the β- barrel of the SH3C structure (PyMOL rendered molecule from 1OEB RCSB protein data bank)

2.1.1 SH3 Fusion Protein ELP-SH3

Elastin-like polypeptides (ELPs) are synthetic biopolymers derived from the naturally occurring structural protein tropoelastin. ELPs are mainly composed of repeating units of Val-Pro-Gly-x-Gly amino acid residues $(V\text{-}P\text{-}G\text{-}x\text{-}G)_n$, where x denotes any guest amino acid except proline. The most common of these ELPs has the repeating units of $(V\text{-}P\text{-}G\text{-}V\text{-}G)_n$. The ELP expressed in this work is composed of $[V\text{-}P\text{-}G\text{-}V\text{-}G]_2$ $[V\text{-}P\text{-}G\text{-}F\text{-}G]_1[V\text{-}P\text{-}G\text{-}V\text{-}G]_4[V\text{-}P\text{-}G\text{-}F\text{-}G]_1[V\text{-}P\text{-}G\text{-}V\text{-}G]_4[V\text{-}P\text{-}G\text{-}V\text{-}G]_4[V\text{-}P\text{-}G\text{-}F\text{-}G]_1[V\text{-}P\text{-}G\text{-}V\text{-}G]_4[V\text{-}P\text{-}G\text{-}F\text{-}G]_1[V\text{-}P\text{-}G\text{-}V\text{-}G]_2$ repeating units. ELPs are able to undergo a reversible phase transition above a critical transition temperature, Tt. These transitions are characterized by increased hydrophobic interactions and aggregation between polypeptide units [42]. The phase transition temperature of ELPs is influenced by several factors including the polypeptide concentration, salt concentration, guest residue composition, polypeptide chain length, and the terminal at which ligation of fusion partners occur. ELPs has been used in particle preparation in recent times; with particles ranging in sizes from nano- to micro scale through inverse phase transition[434445]. Dreher et al created spherical micelles by heating solutions of ELPs above their Tt[46]. Indeed, ELPs have been widely used in hydrogel scaffold formation and in the preparation of in situ gel formation due to its bioresponsive properties[47,48]. Exploitation of these factors allows for the presentation of the SH3 domain on nano- and micro- particles.

2.1.2 Glucagon-like Peptide 1 (GLP-1)

Glucagon-like peptide-1 (7-37), GLP-1, is a truncated form of proglucagon, known to be highly conserved in mammals. This proglucagon-derived peptide is secreted from L-cells

in the intestinal mucosae and pancreatic A-cells, and is also found in the central nervous system. GLP-1 functions as an incretin hormone, known to modulate insulin secretion after nutrient ingestion [32].

GLP-1 binding to its G protein-coupled receptor on beta-cells leads to the activation of adenylate cyclase via the binding of conformationally-activated G_s alpha subunit. Adenylate cyclase then catalyzes the conversion of cyclic adenosine monophosphate, cAMP. A cascade of events in the cAMP pathway leads ultimately to the increases in insulin-containing granule size and mobilization followed by granule exocytosis. GLP-1 is reported to stimulate beta-cell proliferation [49,50], differentiation from progenitor cells [51], and inhibit beta-cell apoptosis [52,53]

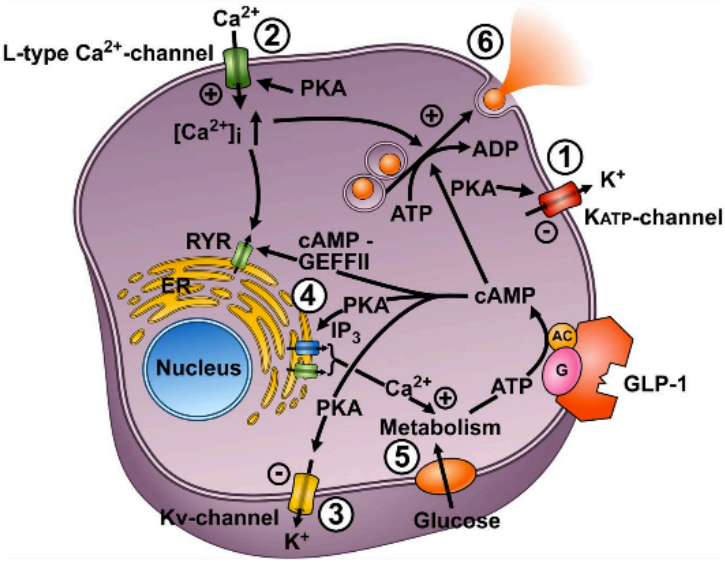

Figure 2-2 Cellular pathways of GLP-1 stimulation of insulin secretion. (Adapted from [32])Reproduced with copyright permission © 2016 The American Physiological Society

GLP-1 stimulated insulin secretion through the six pathways highlighted in Figure 2-2. These include 1) Glucose assisted GLP-1 closing of ATP-sensitive K^+ channels that

increases electrical activity initiating pathway 2) increasing influx of Ca^{2+} due to a slowing in Ca^{2+} inactivation 3) increased action potential via Kv-channel leading to Ca^{2+} influx 4) glucose assisted Ca^{2+} influx through cAMP-GEFII-dependent mechanisms. 5) Stimulation of mitochondrial ATP synthesis through Ca^{2+} mobilization from intracellular stores leading to K_{ATP} channel closure and 6) increased exocytosis of insulin granules pontentiated by high cAMP levels

GLP-1 is believed to inhibit glucagon secretion though the mechanistic understanding of its inhibitory action is in its infancy. Glucagon, a glucoregulatory hormone essential in maintaining glucose homeostasis, catalyzes the release of stored glucose. Importantly, the inhibitory effect of GLP-1 on glucagon secretion occurs only at glucose levels equal to or exceeding fasting levels -- GLP-1 does not promote a state of hypoglycemia [54].

GLP-1, secreted by neurons in the brain, interacts with GLP-1 receptors in the hypothalamic and extra hypothalamic regions in the brain to suppress appetite [55,56]. Administration of GLP-1 to the brain via intra cerebroventricular injection has proven to reduce food intake in rats in the absence of GLP-1 receptor antagonists [57,58]. In morbidly obese patients secretion of GLP-1 is non-detectable [59]. This correlates well with resultant insulin resistance from weight gain [60].

Type 2 diabetes is characterized by insensitivity to glucose-induced insulin secretion. While this insensitivity is due to the loss in effect of another insulinotropic peptide, GIP [ref 18], it has been found that exogenous GLP-1 delivery to patients is restorative [61,62]. However, GLP-1 activity is extremely short-lived with 1-2 minute *in vivo* rapid inactivation by the dipeptidyl peptidase IV enzyme, which cleaves off the N-terminal

histidine and alanine amino acids. This cleavage results in inactive GLP-1(9-37) [63] that potentially acts as a competitive antagonist of the GLP-1 receptor. Holst and colleagues estimates [64] that the active form constitutes less than 25% of all GLP-1 forms leaving the gut and 10-15% in systemic circulation. With a half-life of 4-5 minutes, the kidneys clear both active GLP-1 and its metabolite forms rapidly. Along with its non-hyperglycemia control of insulin secretion, GLP-1 serves to enhance beta-cell survival, inhibit glucagon secretion, reduce appetite along with food intake, and slow gastric emptying making it an ideal therapeutic target. Many GLP-1-based therapies are focused on circumventing its short half-life in vivo by proposing schemes for protease-resistance and the aforementioned extended release. Exendin 4 is protease resistant. It is derived from the venom of *Heloderma suspectum* lizard [65] and acts as a GLP-1 receptor agonist sharing similar potency to GLP-1. Exendin 4, commercially available as Byetta ™, has a half-life of ~30 minutes before renal clearance [66]. This extended half-life is due to the DPPIV-resistant substitution of amino acid Alanine (A) to Glycine (G) at the active N-terminal of the truncated peptide. This evasion of deactivation will be incorporated into the design of GLP-1 fusion peptide used in this work.

2.1.3 SBP Fusion Peptide GLP-1-SBP

Fusion of GLP-1 to SH3-binding peptides (SBPs) confers similar affinities to the therapeutic peptide. GLP-1 was mutated to resist DPPIV protease activity and reduce arginine-glycine protease cleavage at its C-terminal through the substitution of amino acid alanine at position 36 as shown in Figure 2-3 [67] To reduce disruption of GLP-1 secondary structure by SBPs, lysine/serine or glycine/serine repeat linkers incorporated in

the fusion peptide. Two strategies were employed to prepare GLP-1-SBP fusion peptides: recombinant expression, and peptide synthesis.

A $H^{7}\downarrow\underline{A}EGTFTSDVSSYLEGQAAKEFIAWLVKG\underline{R}G^{37}$

B $H^{7}\underline{G}EGTFTSDVSSYLEGQAAKEFIAWLVKG\underline{A}G^{37}$

Figure 2-3 Amino acid sequence of GLP-1 analogs (A) Original conserved GLP-1 sequence. The arrow (↓) marks the typical site of DPPIV inactivation. (B) modified amino acid sequence of GLP-1: amino acids (bold) are essential for GLP-1 binding; modified amino acids are underlined.

2.2 Experimental Details

2.2.1 ELP-SH3 Expression & Purification

ELP-SH3 fusion protein, previously cloned into pQE60 vector (5.1kbp)[68], was transformed in BL21 αF'I^{q} E.Coli cells (New England Biolabs) for expression. Cell cultures were grown at 37°C to an optical density of OD_{600nm} 0.9 in 2X yeast extract and tryptone (YT) with 1:1000 of ampicillin antibiotic stock (200mg/ml) before induction of protein expression with 1mM Isopropyl β-D-1-thiogalactopyranoside (IPTG). ELP-SH3 was expressed for 4 hours post-induction at 37°C. Cells were harvested by centrifugation at 5000 x g for 30 minutes. Cleared lysate containing the soluble fusion protein was collected after sonication on ice (pulse: 15s on, 30 s off, 15 minutes) after which ELP-SH3 was Ni-NTA resin-purified according to the denaturing protocols provided by Qiagen (CA, USA). Purification products were analyzed by sodium dodecyl sulfate polyacrylamide gel electrophoresis (SDS-PAGE) and western blot using anti-HIS Antibody conjugated to Alexa Fluor 488 as probe. Pure ELP-SH3 samples were re-

natured by dialysis in deionized water for 24 hours and concentrated by EMD Millipore centrifugal filter units (CA, USA).

2.2.2 ELP-SH3 Characterization

The concentration dependence of the inverse phase transitioning temperature or turbidity of ELP-SH3 was characterized using an Applied Photophysics Chirascan spectrometer (Leatherhead, UK) for concentrations (5, 10, 20, 30, 40, and 50μM in PBS) with temperature ramp rate at 1^{o}C/min. The transition temperature, T_t, was determined after calculating the maximum first derivative of the optical density (absorbance 350nm). The temperature-dependent phase transitioning was also investigated by dynamic light scattering using a Malven Zetasizer Nano ZS90 (PA, USA).

2.2.3 GLP-1-SBP Design & Production

GST-GLP-1-SBP2 was prepared by cloning GLP1-SBP2 insert into GST Tag containing vector pGEX-4t-2. Gene encoding for amino acid sequence, below was obtained from GenScript

AAH**G**^{8}EGTFTSDVSSYLE**E**^{22}QAAKEFIAWLVKG**A**^{36}GKSKSPAPSIDRSTKPPL.

Following induction with 1mM IPTG ($OD600_{nm}$ = 0.8) and expression in E.Coli for 2.5hrs, purification of Glutathione S-Transferase (GST) tagged GLP-1-SBP was performed natively using gluthatione sepharose resin according to manufacturer's specifications with no modifications. Lyophilized thrombin (GE Lifesciences, PA, USA) reconstituted in deionized water to a concentration of 1 unit/μl, was used to cleave the GST solubility tag from the purified fusion GLP-1-SBP. 1-10 units of thrombin were recommended per mg of recombinant protein. Cleavage products were analyzed with

18% Acrylamide-Bis SDS-PAGE and ESI mass spectrometry (LTQ Orbitrap XL ETD, Thermo Scientific, USA). In addition to recombinant expression, GLP-1-SBPs were synthesized by Genscript (NJ, USA). Characterization of the GLP-1-SBP peptide secondary structure was analyzed by circular dichroism.

2.2.4 Binding kinetics of SBP-SH3 by BioLayer Interferometry

The binding interactions of SBP to SH3 were performed using the Octet RED96 Biolayer Interferometer (ForteBio, CA, USA). ELP-SH3 was conjugated to biotin using a thiol coupling reaction; biotin-maleimide (Sigma-Aldrich, MO, USA) was reacted with the N-terminal cysteine on ELP-SH3. Streptavidin-coated biosensor tips were hydrated in assay buffer (PBS, 0.05% Tween 20, 0.01% BSA, pH 7.4) before assays. To optimize ligand-loading density on the surface of the streptavidin-coated biosensor, dilutions of biotinylated ELP-SH3 were prepared for loading and assayed against a constant concentration of GLP-1-SBP analyte. Kinetic screening of GLP-1-SBP analyte dilutions were conducted following ligand-loading optimization experiments. Briefly, streptavidin biosensors were transferred to the instrument and dipped in assay buffer for 10 minutes to allow for hydration before loading ELP-SH3 ligand for 30 minutes. Biosensors were then dipped in assay buffer for 300s to remove any ELP-SH3 not bound specifically. To establish a baseline the biosensors were transferred to fresh assay buffer for 300s under constant agitation. GLP-1-SBP analyte association with SH3 was measured for a range of concentrations (0, $0.1*K_D$, $0.5*K_D$, $1*K_D$, $5*K_D$, $10*K_D$) for 300s, followed by dissociation measurements for 300s in assay buffer. The assay was replicated three times after sensor regeneration (10mM Glycine, 0.1M NaCl, pH 3) and neutralization (PBS, pH 7.4) steps. New biosensors were used for each type GLP-1-SBP analyte. A reference

biosensor containing no immobilized ligand was used to determine buffer effects and non-specific association of analyte. Figure 2-4 shows a schematic of the protocol steps detailed above. Based on a monophasic analyte binding curve a classical 1:1 biomolecular interaction model was chosen to fit the data.

The association phase was described by an exponential function:

$$y = Rmax \frac{1}{1 + \frac{k_d}{k_a * [Analyte]}} (1 - e^{-(k_a * [Analyte] + k_d)x})$$

The dissociation phase was described by functions

$$y = y_0 e^{-k_d(x - x_0)}$$

$$y_0 = Rmax \frac{1}{1 + \frac{k_d}{k_a * [Analyte]}} (1 - e^{-(k_a * [Analyte] + k_d)x})$$

Association rate constants (k_a), dissociation rate constants (k_d) and equilibrium dissociation (K_D) were obtained from the fitted data.

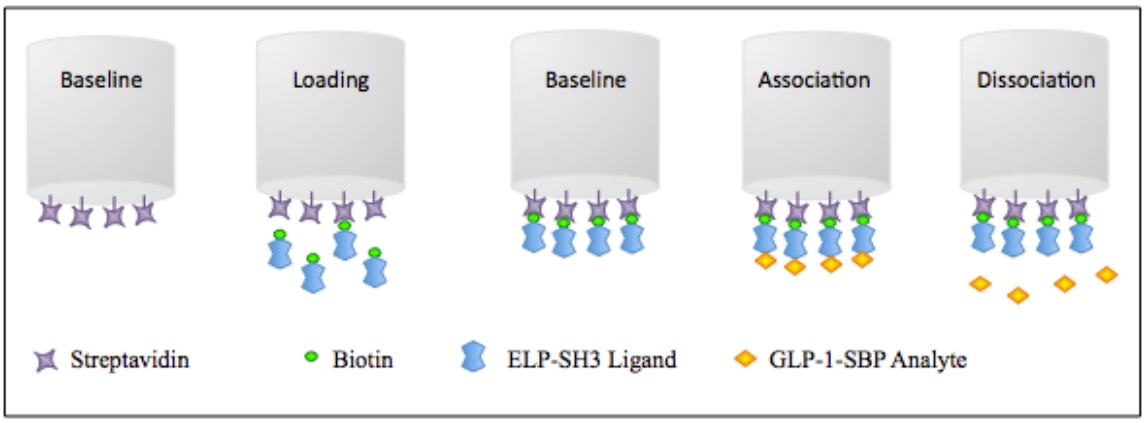

Figure 2-4 Schematic of BLI kinetic assay

2.3 Results & Discussion

Expression and denaturing purification of fusion protein ELP-SH3 was analyzed by SDS-PAGE and western blot (Figure 2-5). ELP-SH3 yielded 18mg per liter of culture. ELP-SH3 (20 kDa) ran slightly higher (~25kDa) in gels in both its monomeric and dimeric forms as confirmed by anti-6xHis antibody probe on western blot. Incomplete reduction of ELP-SH3 may have contributed to the dimers observed (~45 kDa) in the western blot.

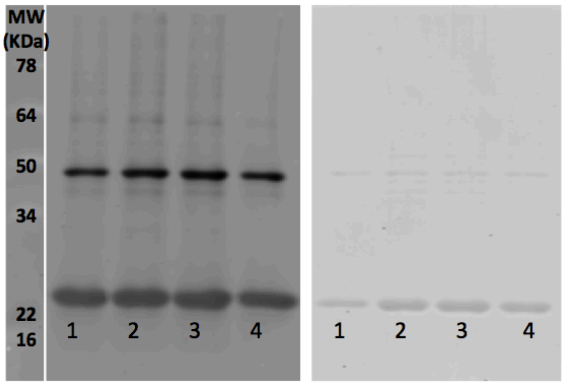

Figure 2-5 Representative images of ELP-SH3. Purification samples as analyzed by western blot (left panel) and coomassie blue stained SDS-PAGE (right panel). Lanes 1-4 are eluted samples of ELP-SH3 after denaturing purification.

ELP-SH3 showed increased solubility in deionized water in comparison to phosphate buffer saline as is expected due to the phase transitioning properties of the ELP. The inverse phase transitioning properties of ELP-SH3 were characterized under several conditions including temperature, protein concentration, and salt in order to determine suitable future assay conditions (e.g. kinetic binding assays) and facilitate delivery system preparation. The phase transitioning behavior exhibited by ELP-SH3 in water varied with concentration (Figure 2-6) but was less rapid than that experienced by ELP-SH3 in PBS. The transition temperature, T_t, for ELP-SH3 in water was calculated as 55^{o}C

for the 50μM. This indicates that the transition temperature may be further depressed by increasing protein concentration > 50μM in water.

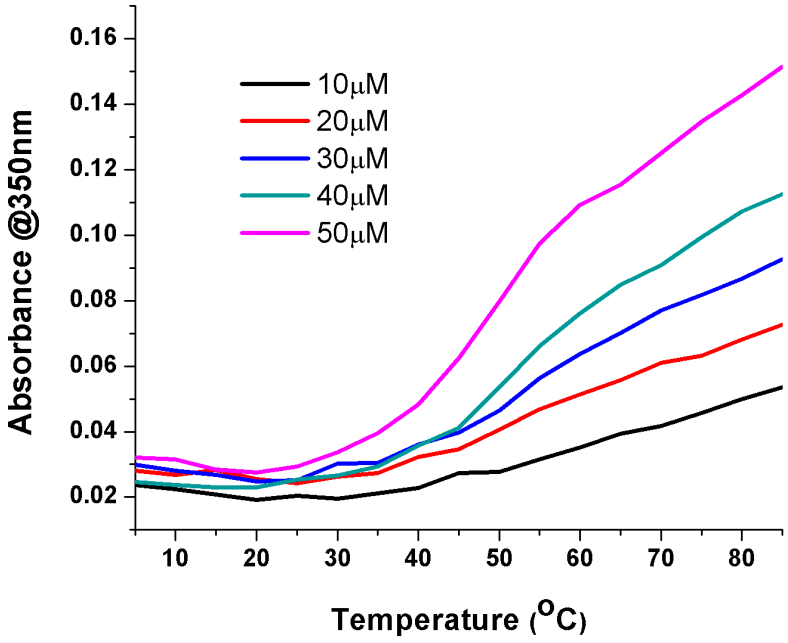

Figure 2-6 The concentration dependence of the temperature profiles for turbidity of ELP-SH3 in water was weak. The transition temperature, T_t, was defined as the temperature at which the maximum dOD/dT occurred. T_t ranged from 60°C - 55°C for 10-50μM ELP-SH3

The concentration dependence on phase transition temperature depression was more pronounced for ELP-SH3 in PBS (Figure 2-7B), with temperatures ranging from 60°C - 30°C. ELP-SH3 samples in PBS were kept at 4°C before analysis to reduce possible precipitation. Precipitation was observed for 50μM ELP-SH3 in PBS even at 4°C, this precipitation might explain the similarity in transition temperature to 40μM ELP-SH3.

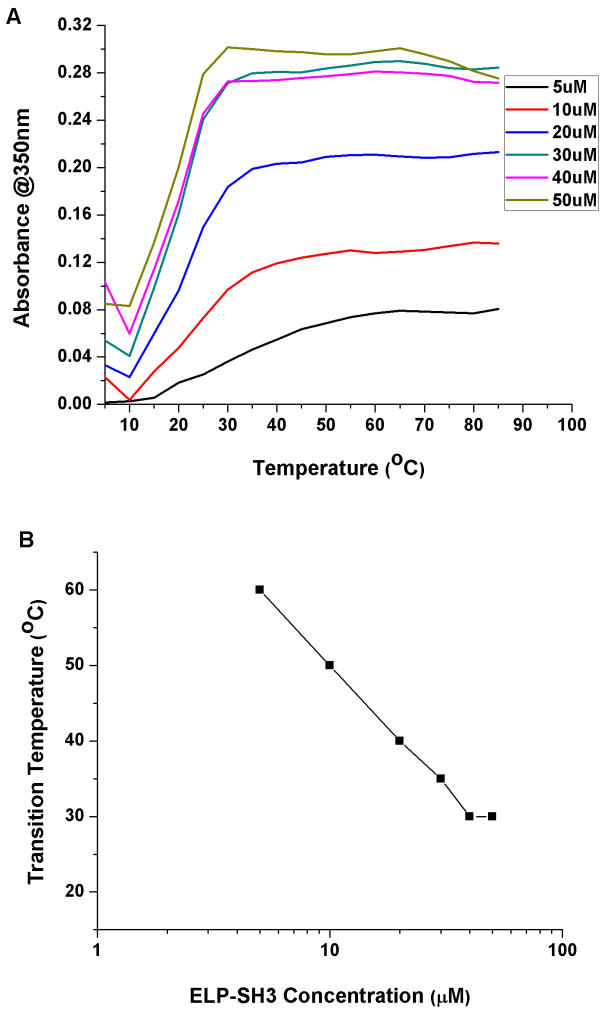

Figure 2-7 Concentration dependence of the temperature profiles for turbidity of ELP-SH3 in PBS. The transition temperature, T_t, was defined as the temperature at which the maximum dOD/dT occurred. (A) Turbidity curves of increasing concentrations of ELP-SH3, (B) calculated transition temperatures for varied protein concentrations.

Dynamic light scattering measurements of 50μM ELP-SH3 in PBS as a function of temperature (Figure 2-8) confirms the formation of nanoparticles (~250nm) at low temperatures. Particle sizes reached it maximum of ~ 4μm at the onset of the phase transition.

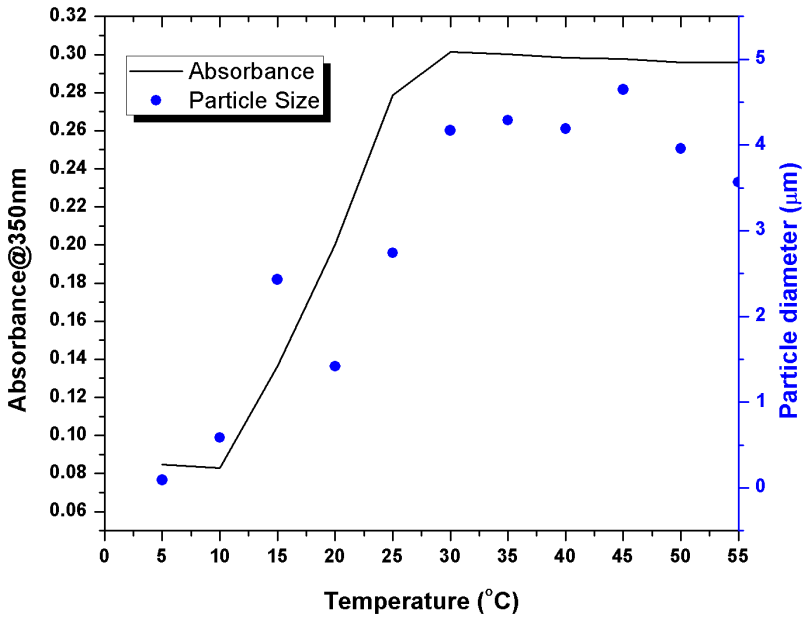

Figure 2-8 Hydrodynamic diameter of ELP-SH3 as a function of temperature. Dynamic light scattering data was acquired for 50μM ELP-SH3 in PBS.

GST-GLP-1-SBP2 was successfully expressed and purified by Glutathione sepharose as evidenced by SDS-PAGE and western blot with anti-GST antibody probe (Figure 2-9). Cleavage by thrombin (GE Healthcare), despite attempts at optimizing cleavage conditions such as concentration, temperature, bead immobilization and time was unsuccessful. Activity of thrombin enzyme was confirmed by the presence of cleavage product GST tag (Figure 2-10 - lane 3). Analysis of cleavage products by MALDI-TOF mass spectrometry revealed non-specific cleavage at the end of the GLP-1 sequence resulting in the effective cleaving off of the affinity peptide (Figure 2-11). Redesign of the linker between GLP-1 and SBP (DNA Sequence listed in APPENDIX I) by site directed mutagenesis resulted in similar cleavage results indicating non-specific cleavage.

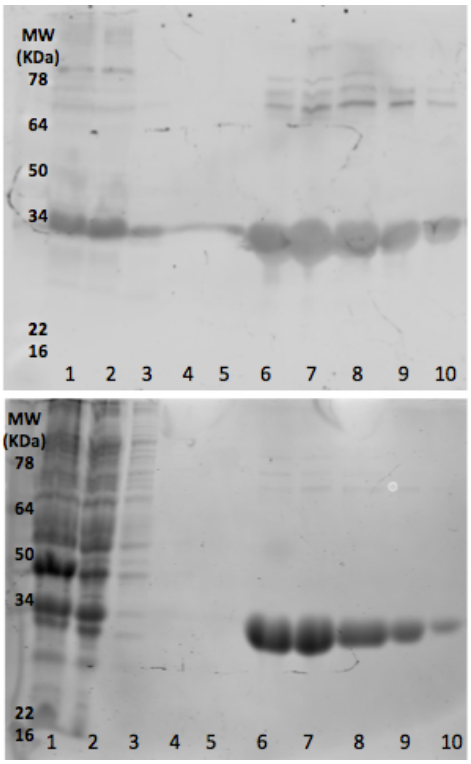

Figure 2-9 Representative images of GST-GLP-1-SBP2 purification samples as analyzed by western blot (top) and coomassie blue stained SDS-PAGE (bottom). Bacterial cleared lysate (lane 1), glutathione sepharose column flow through (lane 2), column washes (lanes 3-5), column elution (lanes 6-10). GST-GLP-1-SBP2 band observed at 31.5 kDa, upper bands in lanes 6-10 are possible degradation product from the GST terminus

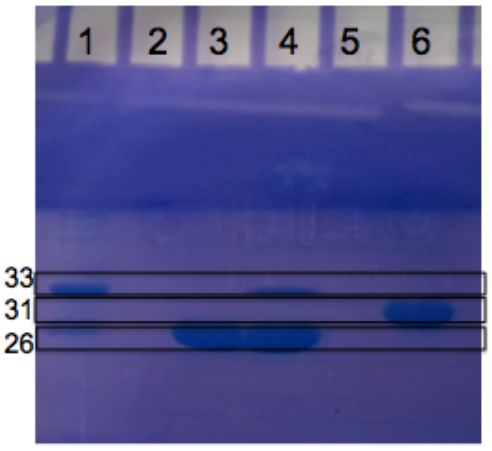

Figure 2-10 SDS-PAGE of GST-GLP-1-SBP2 post-treatment with thrombin (33kDa). Enzyme and cleavage products include: thrombin (lane 1), peptide from resin-immobilized GST-GLP-1-SBP2 cleavage (lane 2), GST tag (lane 3), thrombin

and GST (lane 4), product from GST-GLP-1-SBP2 cleavage in solution (lane 5), and GST-GLP-1-SBP2 before cleavage (lane 6).

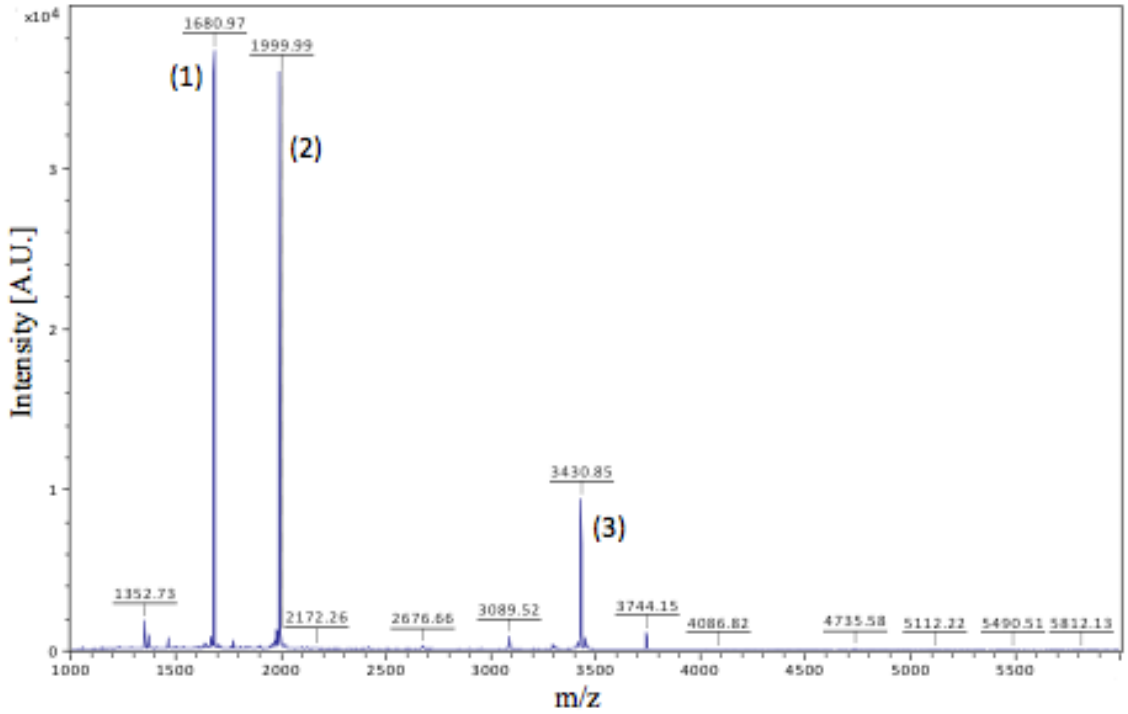

Figure 2-11 GST-GLP-1-SBP2 products are analyzed by MALDI mass spectrometry after treatment with thrombin (GE Lifesciences). Cleavage products show non-specific action of thrombin enzyme. Peaks (1) SKSPAPSIDRSTKPPL, (2) GAGKSKSPAPSIDRSTKPPL, and (3) AAHGEGTFTSDVSSYLEEQAAKEFIAWLVKGA.

Alternatively, GLP-1-SBPs were synthesized by Genscript (NJ, USA). The alpha-helical structure (222nm) present in GLP-1 analog Exendin-4 was confirmed in GLP-1-SBPs. Alpha-helical peak at 208nm were offset by the presence of SBP which has a strong characteristic peak at 200nm (Figure 2-12).

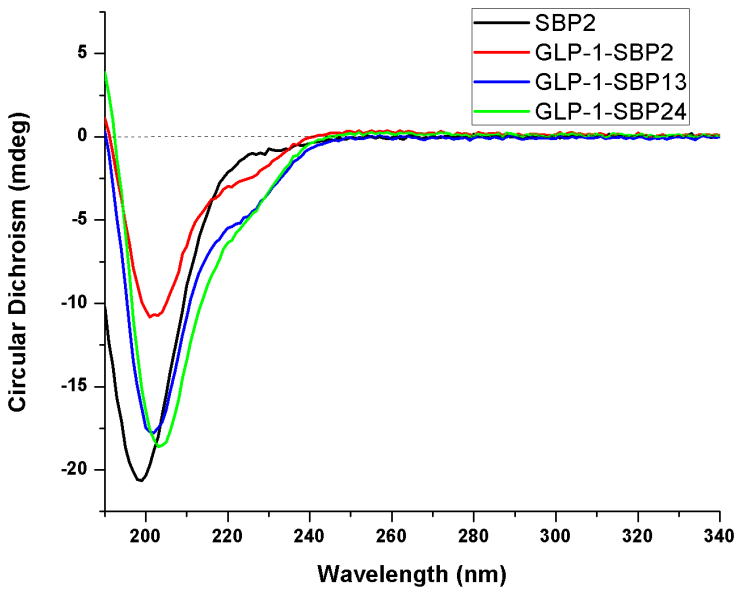

Figure 2-12 Circular dichroism spectra of GLP-1-SBP peptides and SBP at 16µM and ~0.4 µM in water respectively. Alpha-helical characteristic peak at 222nm is evident for GLP-1-SBPs but absent in SBP2

Kinetic parameters of SBP and SH3 binding interactions were measured using BioLayer Interferometry (ForteBio). Analysis required optimization of ligand binding to sensor tip before kinetic assay.

The optimal density of immobilized biotinylated ELP-SH3 ligand was determined after performing loading and analyte association with varied concentrations of ligand. Ligand concentration resulting in significant but not saturated loading signal with a slow initial loading rate and a high analyte association was chosen as the optimal loading density. The ELP-SH3 biotinylated ligand tended to form nanoparticles at high concentration in the assay buffer or upon contact with the sensor surface. Functionalization with PEG4-Biotin decreased aggregation. Optimization of assay buffer and loading conditions were essential for proper ligand loading. Fitting of GLP-1-SBP13 analyte association and dissociation curves for serial dilution of analyte resulted in a good fit for the 1:1

interaction model. Fitted kinetic parameters could be obtained only for the GLP-1-SBP13 analyte due to equipment malfunction. However, BLI analysis of GLP-1-SBP13 binding had an affinity value of K_D of 1.66 x 10^{-7} (M) which is of similar magnitude to previous data for FN-SBP13 (K_D 4.59 x 10^{-7} (M)) obtained by SPR analysis. This suggests that the fusion of GLP-1 peptide to the SBPs do not adversely affect affinity binding.

CHAPTER 3.

CONTROLLED RELEASE OF GLP-1 FROM AFFINITY-BASED PROTEIN MICROSPHERES

3.1 Background

Glucagon-like peptide-1, GLP-1, along with analog Exendin-4 is one of the major peptide-based treatments for Type 2 diabetes. GLP-1 stimulates the secretion of insulin and pancreatic beta cell proliferation [32,49]. However, GLP-1 suffers from inactivation by DPPIV enzyme in vivo and like most peptide undergoes rapid clearance. To overcome these challenges GLP-1 has been conjugated to large molecules, undergone sequence mutation, or encapsulated in polymeric microparticles [33,69–71].

Roughly one-tenth of the US population has been diagnosed with diabetes or pre-diabetes (early onset insulin resistance), with 90% of those cases associated with Type 2 diabetes [31]. Long-lasting formulations that increase patient compliance while maintaining therapeutically relevant doses are attractive alternatives to once-daily injections. Bydureon (AstraZeneca), consisting of Exendin-4 encapsulated within polymeric particles is the only microsphere formulation currently on thes market with a once-weekly administration. Several research studies are focused on particle-based release systems for both subcutaneous and oral delivery of GLP-1. Amiram et al proposed a promising cleavage-dependent release of GLP-1 from an injectable biopolymer depot [67], while Kim and colleagues sought to increase patient compliance by fabrication of exendin-4-loaded chitosan particles for oral delivery thereby avoiding the subcutaneous

route [72]. Combinatorial use of PEGylated exendin-4 and encapsulation within PLGA microspheres were investigated by Lim and colleagues to allay the effects of peptide-destabilizing acylation reactions, and to increase circulation time of peptide upon release, while taking advantage of the degradation-dependent release of the PLGA encapsulation system [73]. Common to these approaches is the attempt to maintain glycemic control through sustained bioavailability of the peptide therapeutic. However, enzyme-mediated release systems are limited by enzyme diffusion to substrate site, while peptide activity may be compromised by harsh conditions in the gut during oral delivery. Approaches similar to Lim et al using degradation- and particle-based systems have been exhaustively investigated. However, the tendency for diffusive over degradative release [8] and the poor adaptation to hydrophilic proteins and peptides [4] respectively, make such systems undesirable for controlled peptide release [74]. Other systems employ harsh incompatible organic solvents for fabrication denature or destabilize structure leading to loss of therapeutic activity.

In Chapter 1 several affinity-based studies employing complementary binding pairs to reduce non-specific binding and to control release have been described. An illustrative example of the use of affinity binding pairs to reduce non-specific interactions is presented by Belair and colleagues. They reported that serum-enhanced release rates of VEGF from VEGF binding microspheres was much slower for the VEGF binding peptide over the low affinity scramble peptide control[22]. Another prominent contributor in this emerging class of delivery systems is the Shoichet group. They have developed delivery systems using SH3 fusion proteins of both chondroitinase ABC and growth factor bFGF to showing release over periods of 7 and 10 days respectively with binding affinities of

10^{-5} – 10^{-7}M [19,20]. Herein we use affinity-dependent release of GLP-1 from protein microspheres that preserves function through mild preparation conditions and minimizes non-specific interaction while sustaining release. Our system seeks to reduce the frequency of injections by sustaining therapeutically relevant peptide release profiles and to decrease the burst-release effects experienced by encapsulation systems. To achieve this, we exploit the associative and dissociative interactions between protein domains for specific immobilization and release, respectively. These domains are the Src Homology domain 3 (SH3), and its partner SH3 binding peptide (SBP). To develop our delivery system; SH3 was expressed as a fusion protein with elastin-like polypeptide (ELP-SH3) which facilitates microsphere preparation while the SBP was synthesized with GLP-1 as the 45 aa peptide GLP-1-SBP. Interactions between the microsphere-immobilized SH3 and GLP-1-SBP allow for reversible binding that impedes the release of GLP-1 fusion peptide. SBPs; SBP2, SBP13, SBP24, possessing a wide range of affinities (K_d from 10^{-8}M (high), 10^{-7}M (mid), 10^{-6}M (low)) allows for the tuning of the GLP-1 release rates from the microspheres. Here we show that functionality of the SH3 domain survived the gentle microsphere fabrication process. We demonstrate the 7- day release of active GLP-1-SBPs as evaluated by GLP-1 ELISA and cell number increase *in vitro*. Mouse pancreatic insulinoma βTC-6 cells, known to proliferate in the presence of GLP-1 receptor agonist, assessed the activity of GLP-1-SBPs release from microspheres in vitro. GLP-1-SBPs modulation of insulin secretion was also evaluated. To facilitate estimation of peptide affinity effects on release rate from microspheres a mathematical model, developed previously by Saiyama-Elbert et al, describing the release of peptides from hydrogels was employed [15,75]. The model comprised of a system of equations; a reaction-

diffusion equation for the diffusing species along with mass balances on immobilized species, characterized the influence of affinity strength on the release rates of GLP-1-SBP from SH3 microspheres.

3.2 Experimental Details

3.2.1 Peptides

Exendin-4 and GLP-1 were purchased from SigmaAldrich. GLP-1-SBP peptides were synthesized by Genscript (NJ, USA). The sequences of the peptides are shown in Appendix I.

3.2.2 Cell Culture

βTC-6 mouse pancreatic insulinoma cells, were grown in DMEM media (ATCC 30-2002) supplemented with 15% heat inactivated fetal bovine serum and 100 U/ml penicillin/Streptomycin.

3.2.3 Stability of GLP-1-SBP

Stability of GLP-1-SBPs was qualified by the preservation of the alpha-helical secondary structure at 208, and 222nm using circular dicroism (APL Chirascan). The quantity of active GLP-1 was measured by active GLP-1 ELISA that recognizes only the intact N-termini of GLP-1 peptides.

3.2.4 ELP-SH3 Immobilization on polysterene microparticles

ELP-SH3 protein cloned previously with a cysteine residue at its N-terminus allowed for thiol conjugation to microparticle. ELP-SH3 was covalently coupled to the microparticle surface in the following coupling steps. Carboxyl-functionalized polysytrene microparticles 3 microns in nominal diameter (2.6 wt%) were purchased from Polysciences Inc (PA, USA). 382ul of particle suspension was removed from a well-shaken stock solution and centrifuged at 2500 x g for 2.5 minutes. Particles were then activated by twice repeated suspension in 0.1mM MES buffer (pH 5.2). The activated carboxyl groups were then reacted with 50mM of Ethyl-3-(3-dimethylaminopropyl)carbodiimide (EDC), which forms an unstable O-acylisourea intermediate, and 16.7mM sulfo-NHS transforming the intermediate to the more stable sulfo-NHS ester intermediate for 15 minutes under constant shaking at room temperature. The particles were then twice washed with 1xPBS (pH 7.4) to remove unreacted reagents. Reaction with 33.2mM of 2-(2-pyridyldithio) ethyleneamine (PDEA) in 0.1M acetate buffer (pH 4.2) for 15 minutes under constant shaking at room temperature. Following the reaction particles were thrice washed with distilled water. The thiol-terminated ELP-SH3 was reduced in 5mM TCEP solution for 30 minutes then desalted using PD Desalting columns from GE Healthcare (NJ, USA) in preparation for the coupling reaction. 1mg/ml of ELP-SH3 was added to the PDEA activated microparticles and reacted for 2-4hrs under constant shaking at room temperature. The molar quantities of the reagents used were based on Polyscience's reported molar range of the carboxyl-functionalization. EDC/NHS/PDEA were used in a 3:1:2 molar ratio to the -COOH groups on the microparticles.

3.2.5 Elastin-like polypeptide microsphere formulations

50 μM of ELP-SH3 in deionized water (18.2 MΩ-cm) was sonicated at 25^{o}C for 10 minutes. NaCl was added to a final concentration of 0.3M with continued sonication for 10 minutes. Amine-reactive cross-linker DTSSP was added to a final concentration of 0.75mM under continuous sonication for 30 minutes. Unreacted cross-linker was removed by twice-repeated centrifugation at 500 x g for 5 minutes and suspension in 1xPBS. Microsphere formulations in which variation of either crosslinker concentration (0.75mM to 6mM), salt concentration (60mM to 300mM), or loading conditions (temperature and salt concentration) were investigated for optimization of microsphere stability and loading capacity. Characterization of the SH3 microspheres hydrodynamic radii, R_h, was performed using dynamic light scattering Zetasizer Nano ZS90 (Malvern Instrument) before storage at 4^{o}C. Microsphere samples were twice- washed in deionized water then dried on silicon wafers overnight at room temperature in preparation for imaging by scanning electron microscopy (S.E.M). SH3 microsphere morphologies were characterized by S.E.M operated at 5kV accelerating voltage and 3mm working distance.

3.2.6 Analysis of SH3 microsphere loading with GLP-1-SBP

Specificity of GLP-1-SBP loading was determined by fluorescence detection. Loaded microspheres were incubated with mouse anti-GLP-1 primary antibodies for 1 hour before washing and subsequent incubation with fluorescently-labeled anti-mouse secondary antibody. Flow cytometry detected fluorescent GLP-1-SBP bound to

microspheres; their mean fluorescence compared to that of unloaded microspheres with and without antibody probes.

To facilitate direct fluorescent detection, GLP-1-SBPs were conjugated to TAMRA dye. Briefly, 20mM TAMRA-NHS ($^{ex}/_{em}$ 546/579) ester in DMSO was reacted with GLP-1-SBP in 50mM phosphate at pH 6.5 for preferential labeling of the α-amino group while lysine amines (ε-amino group) remain protonated. Unreacted TAMRA dye was separated from the conjugation mixture by dialysis for 48 hours with intermittent buffer exchange. To determine whether the binding capacity of the various microsphere formulations were affected by either cross-linking density or loading conditions, the prepared formulations were incubated with TAMRA-labeled GLP-1-SBP before detection by flow cytometry. Confocal microscopy was employed for additional verification of binding. Confocal microscopy (Carl Zeiss LSM 510B) images of fluorescently-labeled GLP-1-SBP loaded microspheres were obtained using a 63X oil immersion objective at TAMRA laser excitation wavelengths. Loaded samples were diluted with 50% glycerol/PBS solution immediately before imaging.

The binding capacity of the most stable microsphere formulation was determine using fluorescent plate reader (BioTek). Briefly, 1 mg/ml of microspheres were loaded with varying concentrations of TAMRA-labeled GLP-1-SBPs for 1 hour followed by centrifugation for 5 minutes at 500 x g. Supernatant fluorescence was measured by plate reader and peptide quantity determine by comparison to serial dilution curves of the loading solution. The quantity GLP-1-SBP captured by microspheres was calculated by subtraction of original loading amount from amount remaining in supernatant.

3.2.7 Bioactivity of GLP1-SBP: Beta-Cell Counting Assay

βTC-6 cells were seeded in 24-well plates at a density of 20 x10^4 cells/well in complete media comprised of penicillin/streptomycin, 16.7mM glucose DMEM (ATCC 30-2002), and 15% Heat Inactivated FBS. Cells were treated with 10nM peptide agonists at 2-day intervals after seeding for 6-10 days in DMEM Media with 5.5mM glucose and 2% heat inactivated fetal bovine serum (serum-starved conditions). After aspiration of cell media, cells were treated with 0.05% Trypsin, 0.53mM EDTA for 15 minutes at 37C followed by addition of cold PBS before storage on ice (4C) in preparation for counting by flow cytometry. Increase in cell number was assayed as described above for GLP-1-SBPs released from microspheres using transwell inserts in 24-well plates as shown in the schematic in Figure 3-1.

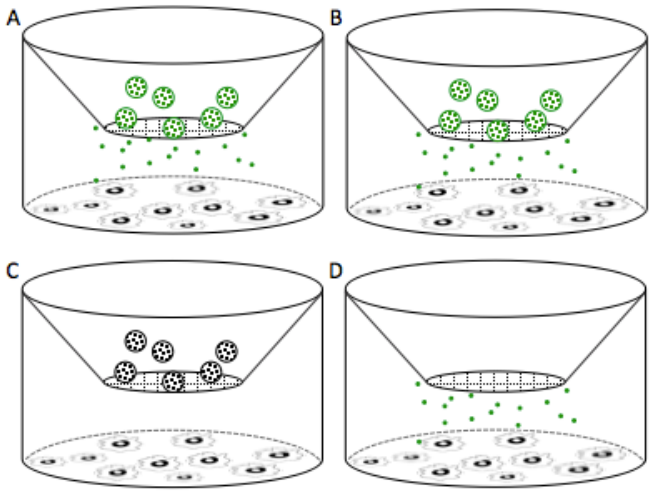

Figure 3-1 Schematic of GLP-1-SBP release from microspheres. Microspheres were loaded with GLP-1-1SBPs (A-B), empty (C) or soluble GLP-1 agonist. Cell media was replaced 2-day intervals.

3.2.8 Bioactivity of GLP1-SBP: Insulin Secretion

βTC-6 cells were seeded at 150,000 cells/ 1.9cm^2 in a 24-well plate were washed in glucose-free Krebs-Ringer Bicarbonate buffer (115mM NaCl, 24 mM $NaHCO_3$, 5mM KCl, 1mM $MgCl_2$, 2.5 mM $CaCl_2$, and 25mM HEPES, 1 mg/ml Bovine Serum Albumin, pH 7.4) then incubated in glucose-free krebs-ringer bicarbonate buffer 37^{o}C, 5% CO2 for 1 hour prior to treatment [76,77]. Cells were then treated with Krebs/HEPES buffer containing 0, 3, and 16.7mM glucose with either GLP-1-SBP2 or GLP-1 for 2 hours at 37^{o}C 5% CO_2. Cell supernatants were collected and the secreted insulin quantified by insulin ELISA kit (Crystal Chem, IL).

3.2.9 Induction of insulin secretion by loaded microspheres

βTC-6 cells were cultured in 24-well plates to 70% confluence in 16.7mM glucose DMEM (ATCC 30-2002), and 15% Heat Inactivated FBS. Cells were washed glucose-free Krebs/Hepes buffer for 1 hour prior to incubation in Krebs/HEPES buffer containing 3mM Glucose for 24 hours. GLP-1-SBP loaded microspheres were incubated with plated Beta-TC-6 cells using a transwell 24-well insert. Microspheres were placed in 0.4 micron pores transwell insert (Corning, NY, USA). 10 μl of cell supernatant wad removed after 2, 4, and 12 hours. Insulin secretion in cell supernatants was quantified by ELISA (Crystal Chem).

3.2.10 GLP-1-SBP Release from microspheres

SH3 microspheres were incubated with 0.5mg /ml GLP-1-SBPs overnight in 1.5ml Low protein binding microcentrifuge tubes (Eppendorf) to allow for equilibrium binding. Microspheres were twice washed -- centrifuged at 500 x g for 5 minutes followed by suspension in 1x PBS and placed in transwells inserts in 24-well plates containing 1xPBS. Supernatants were collected at varying time points and equal volumes of 1xPBS were replaced at each time point. GLP-1 ELISA quantified peptide concentration in supernatants (EMD Millipore).

3.2.11 Competitive binding experiment

SH3 microspheres were incubated with TAMRA-labeled GLP-1-SBPs for 4 hours at 4C. Varying concentrations of soluble ELP-SH3 were then added to the incubated samples. After dosing, the samples were incubated for an additional 4 hours at 4C. Microsphere fluorescence was then measured by flow cytometry.

3.2.12 Normalization of Release Data

Fractional release curves were obtained through normalization to the total quantity of peptide detected. At the end of release period, ELISA determined the quantity of peptide remaining on microspheres. Total peptide detected was calculated as the sum of the

quantity from cumulative release and the quantity remaining on microspheres after the release period.

3.2.13 Mathematical Model

$$SH3 + SBP \underset{k_r}{\overset{k_f}{\rightleftharpoons}} SH3 - SBP \quad (1)$$

$$\frac{\partial C_{SBP}}{\partial t} = \frac{D_{SBP}}{r^2}\frac{\partial C_{SBP}}{\partial r^2} + \frac{D_{SBP}}{r}\frac{\partial C_{SBP}}{\partial r} + k_r C_{SH3-SBP} - k_f C_{SBP} C_{SH3} \quad (2)$$

$$\frac{\partial C_{SH3}}{\partial t} = k_r C_{SH3-SBP} - k_f C_{SBP} C_{SH3} \quad (3)$$

$$\frac{\partial C_{SH3-SBP}}{\partial t} = k_f C_{SBP} C_{SH3} - k_r C_{SH3-SBP} \quad (4)$$

Equation (1) describes the binding interaction between the components of the affinity-based system[78,6]. The SH3 domain is modeled as immobilized or microsphere-bound, while GLP-1-SBP, denoted here as SBP, is modeled as the diffusing species. SH3-SBP describes the microsphere-bound complex. The model assumes that both SH3-SBP and SH3 are non-diffusible species, while SBP is diffusible. Mass balances for each species within the affinity-based system resulted in the derivation of one partial differential equation describing the reaction-diffusion of SBP species in spherical co-ordinates (equation 2) and two ordinary differential equations (equations 3-4). Kinetic constants, k_f and k_r, describe the forward and reverse rates of SH3/SBP interactions. D denotes the

diffusion coefficient of SBPs. The model assumes perfect "sink" -- Dirichlet condition at the outermost boundary and a Neumann condition at the innermost boundary

Assuming all reactants are at equilibrium provides the initial conditions for the model, these conditions are represented by equations (5) through (7)

$$k_f C_{SBP}^{EQ} C_{SH3}^{EQ} = k_r C_{SH3-SBP}^{EQ} \quad (5)$$

$$C_{SBP}^{TOT} = C_{SBP}^{EQ} + C_{SH3-SBP}^{EQ} \quad (6)$$

$$C_{SBP}^{TOT} = C_{SBP}^{EQ} + C_{SH3-SBP}^{EQ} \quad (7)$$

For all r @ t=0 $C_i = C_i^{EQ}$ where i= SBP, SH3, SH3-SBP

Equations (8) and (9) describe the boundary conditions of the model

For t > 0 @ r=R $C_{SBP} = 0$ (8)

For t > 0 @ r= 0 $\frac{\partial C_{SBP}}{\partial r} = 0$ (9)

The system of equations was solved using MATLAB solver PDEPE that involves the numerical discretization of the coupled PDE-ODE equations. MATLAB source code (Appendix II)

Table 1: Constants used in mathematical model

Constants	Values	Units
*$D_{SBP,i}$	1.3×10^7	$\mu m^2/d$
$k_{f,SBP2}$	6.03×10^5	1/Ms
$k_{r,SBP2}$	0.017	1/s
$k_{f,SBP13}$	9.26×10^4	1/Ms
$k_{r,SBP13}$	0.043	1/s
$k_{f,SBP24}$	1.85×10^4	1/Ms
$k_{r,SBP24}$	0.091	1/s

i= 2, 13, or 24 *Diffusivity of GLP-1-SBP was estimated from the diffusivity of a 12mer heparin-binding peptide in mucus [75,79]. $k_{f,i}$ and $k_{r,i}$ are estimated for GLP-1-SBPs from the values for Fibronectin-SBPs obtained by Surface Plasmon Resonance.

3.2.14 Data Analysis

Studies were performed in triplicate and reported as the mean +/- standard deviation. Statistical significance was determined by student's t-test, with a p-value of less than 0.05 being considered statistically significant.

3.3 Results and Discussion

Proteolytic inactivation and reduced bioavailability are main challenges facing peptide therapeutics. We report the release of GLP-1-SBPs from an affinity-based protein microsphere that effectively seeks to reduce decrease degradation through protease-resistant peptide design and sustain release. Affinity-based microspheres ensure that active peptides are available in tunable quantities for efficacy of treatment while reducing quantity of injections required. This system negates not only the need for the high molecular weight peptide fusion formulation with polymers and biopolymers that can sterically hinder receptor binding and potentially reduce efficacy [80,81] but also reduces potential polymer-related peptide denaturation and adsorption [82] by controlling how the peptide interacts with the microsphere, namely through specific binding and release.

3.3.1 Microsphere Fabrication and Characterization

To facilitate affinity-based immobilization and release of fusion affinity binding partners, ELP-SH3 and GLP-1-SBP2 were prepared. The elastin-like polypeptide imparted inverse phase transitioning properties to the ELP-SH3 fusion protein. Its increased hydrophobic interaction in response to increased salt and protein concentration allowed for the biocompatible preparation of ELP-SH3 microspheres. During this inverse phase transition it is expected that SH3 domain will not be denatured. ELP fusion protein, thioredoxin–ELP underwent inverse transition cycling (ITC) with retention function, indeed ITC is proposed by Chilkoti and colleagues as a tandem protein purification method [8384]. This is attributed to the presence of water (~60%) [36] in sufficient amounts to keep the guest domains hydrated and in its natural conformation in the aggregated phase.

Stability of SH3 microspheres was achieved via amine cross-linking following microsphere formation preventing the dissolution to soluble ELP-SH3 at storage temperatures lower than the transition temperature. Salt concentration played a significant role in particle stability -- low salt formulations (60mM-150mM) tended to aggregate over time despite the stabilizing effect of cross-linking. S.E.M images confirmed DLS diameters (Figure 3-2). Increasing concentration of ELP-SH3 in the absence of salt let to nanosphere formations. Particle size increased as a function of both protein and salt concentrations. Particle size increased to 5 microns on average in 0.3M salt and 50μM ELP-SH3 concentrations. SH3 microsphere preparation with varying quantities of cross linker did not affect the loading of GLP-1-SBP fusion peptides. GLP-1-SBP binding occurred throughout the microspheres evidenced by confocal microscopy imaging of the loaded microspheres (Figure 3-3) and was not limited to surface binding only. Examination of loading via flow cytometry across various microsphere formulations confirmed that cross-linking density, salt concentration, or loading temperature had no effect on GLP-1-SBP binding (Figure 3-4). Anti-GLP-1 antibody probing of loaded microspheres confirmed the presence of GLP-1-SBP on the microsphere surface (Figure 3-5). An anti-GLP-1 antibody that is specific to the active N-termini of GLP-1 probe was employed. Fluorescence remained relatively similar across all microsphere formulations suggesting that the SH3 domain function was preserved and competitive binding experiments (Figure 3-6) confirmed binding specificity. A fractional loading of 30-40% was achieved for both low and high cross-linker concentration (Figure 3-7). The positive shift in fluorescence indicates that GLP-1-SBP immobilized on SH3 microspheres retained its structure suggesting specific binding interaction. Additionally,

specificity of binding was analyzed by competitive binding. The loss of GLP-1-SBP binding to microsphere in the presence of soluble SH3 competitor demonstrated the specificity and reversibility of interactions between the SH3 and SBP binding partners.

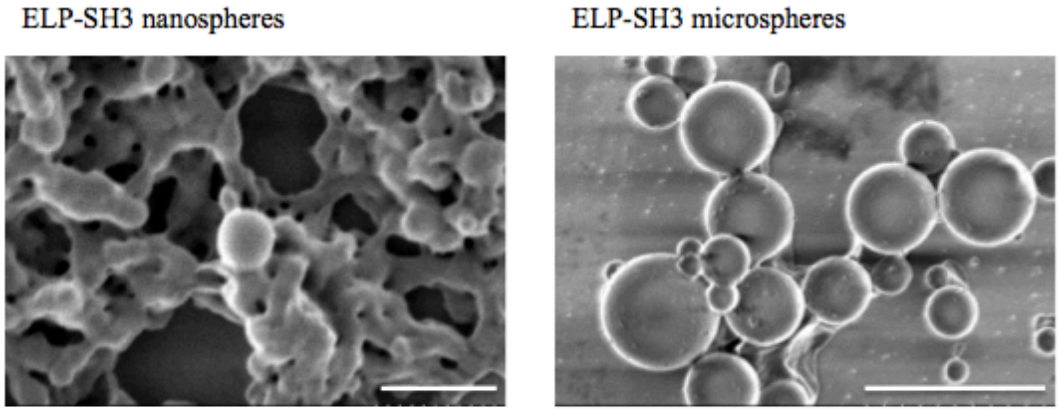

Figure 3-2 Scanning electron microscope images of 50µM ELP-SH3 particles cross-linked with amine reactive DTSSP. Nanospheres were prepared with 50µM ELP-SH3 in the absence of salt (scale 500nm). Microspheres were prepared with 50µM ELP-SH3 and 300mM salt (scale 5µm).

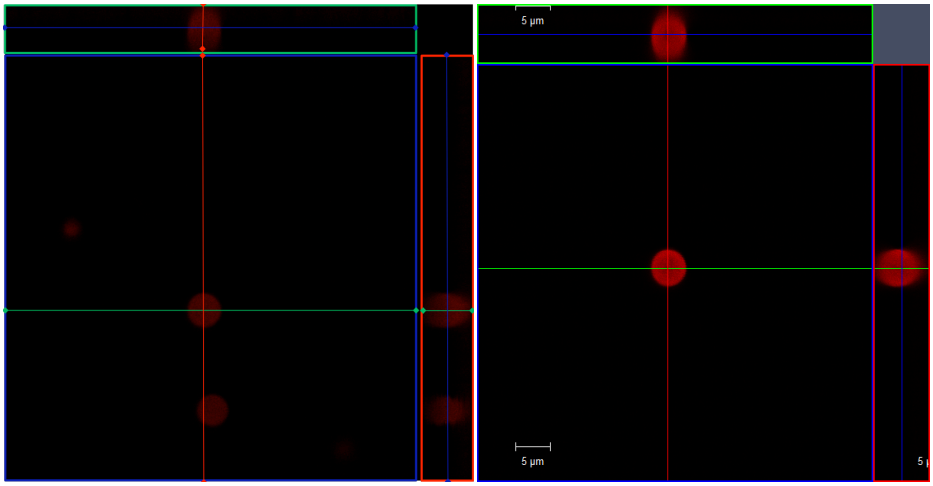

Figure 3-3 Confocal Laser Scanning Microscopy (CLSM) image of TAMRA-labeled GLP-1-SBP loaded ELP-SH3 microspheres. Microspheres were prepared with 150mM Salt and 6mM DTSSP crosslinking Representative image of microspheres loaded in conditions below their transition temperature, $T < T_t$ (left) and above $T > T_t$ (right)

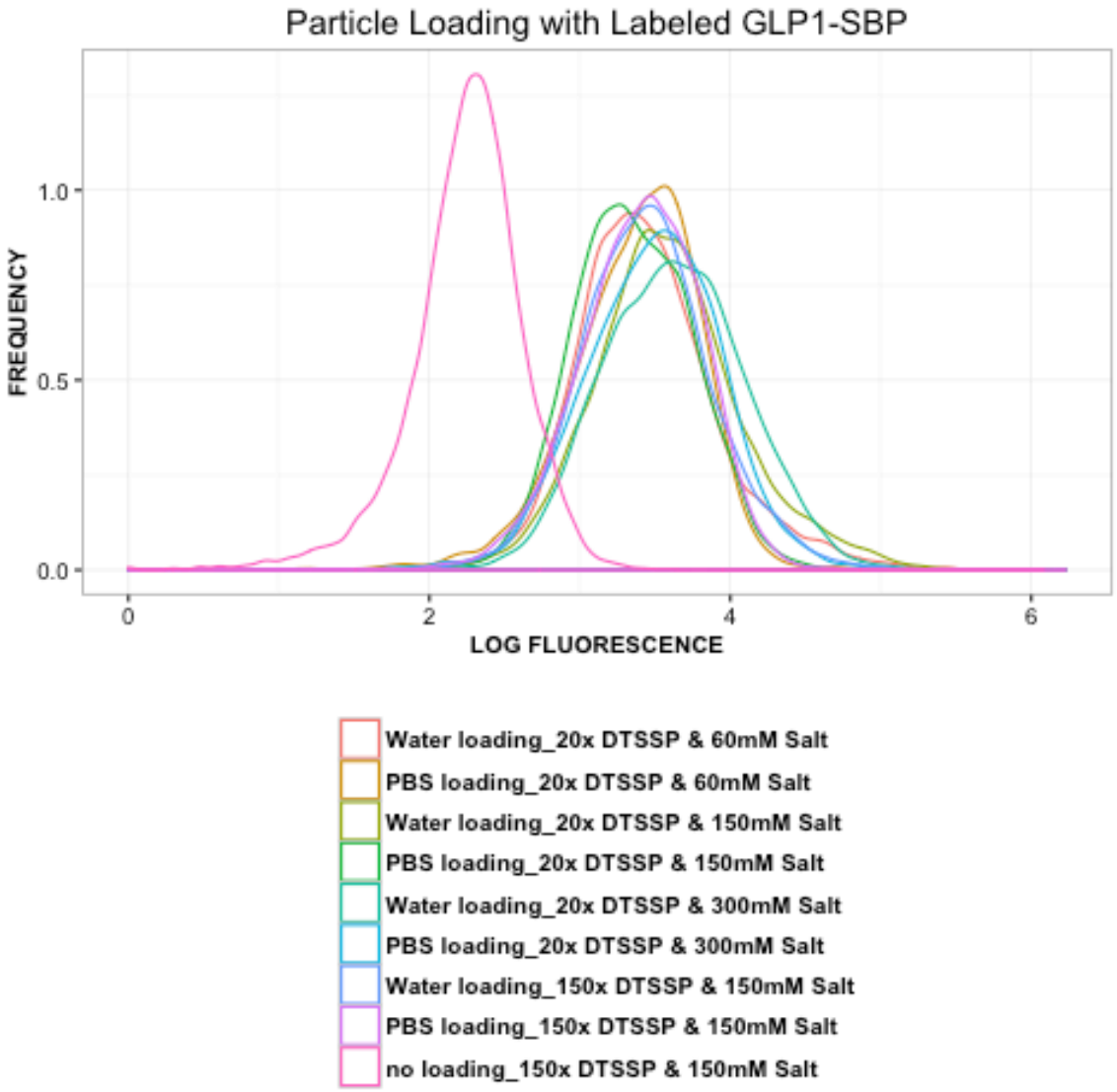

Figure 3-4 Loading capacity of SH3 microsphere formulations analyzed by fluorescence intensity. Formulations were incubated with equal amounts of TAMRA-labeled GLP-1-SBP. Microsphere fluorescence, analyzed by flow cytometry 12-hours post incubation showed no significant increases in fluorescence among loaded microspheres.

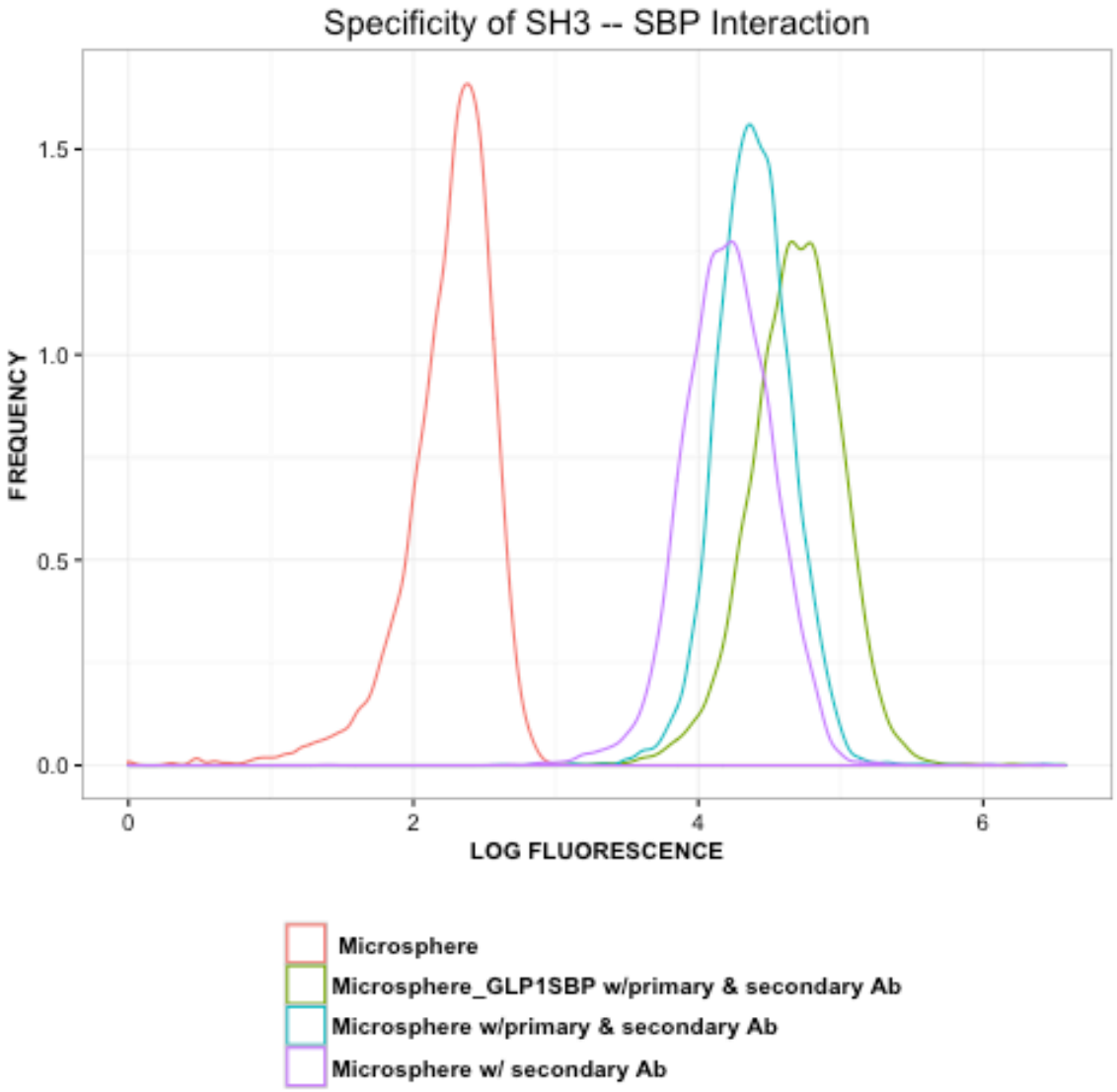

Figure 3-5 GLP-1-SBP binding to SH3 microsphere. 1mg/ml of SH3 microspheres were incubated for 4 hours with 0.100 mg/ml GLP-1-SBP. Qualitative analysis of GLP-1-SBP immobilization on microspheres using anti-GLP-1 and Alexa fluor 633 anti-mouse secondary antibody showed an increase in mean fluorescence in comparison to the microspheres without GLP-1-SBP.

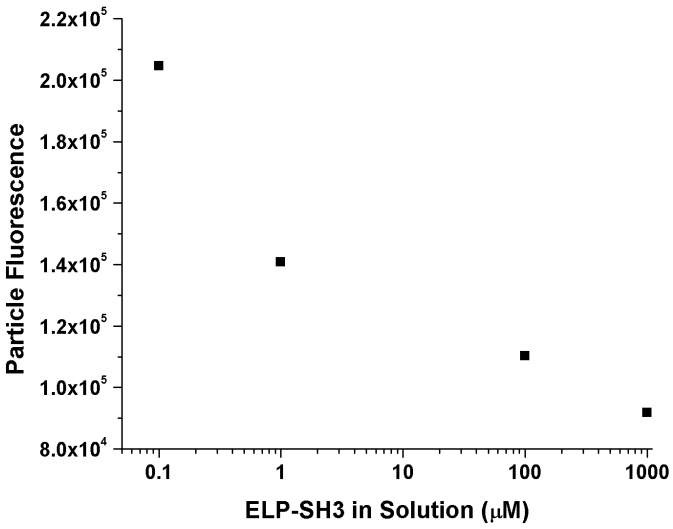

Figure 3-6 Competitive binding assay. GLP-1-SBP loaded microspheres were incubated in varying concentrations of free SH3. As the concentration of free SH3 increased, the amount of GLP-1-SBP immobilized on microspheres decreased leading to a reduction in fluorescence

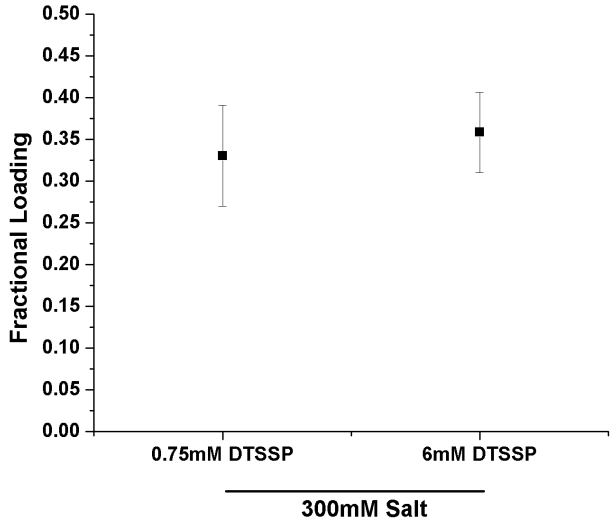

Figure 3-7 Quantification of GLP-1-SBP binding to varied SH3 microsphere formulations. 1mg/ml of SH3 microspheres were incubated for 12 hours with 0.150 mg/ml TAMRA-labeled GLP-1-SBP. Formulations prepared with 0.3M NaCl and stabilized with either low or high concentrations of DTSSP cross-linker showed similar loading capacities of 30-40% of the loading solution, while other formulations varied in stability and/or binding capacity. Error bars represent standard deviation across three separate experiments

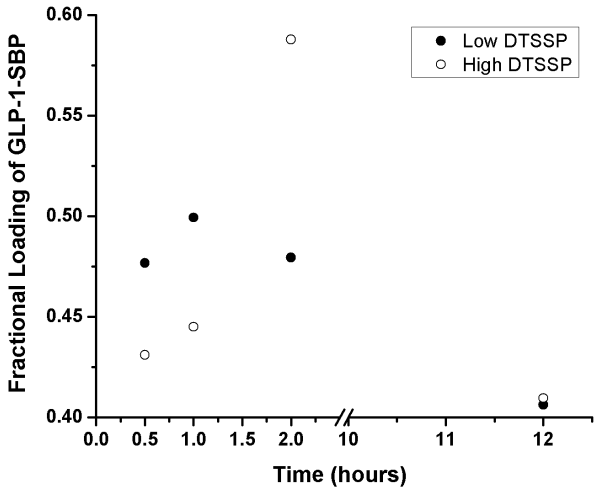

Figure 3-8 GLP-1-SBP binding characterization. Fractional loading of low and high cross-linker microsphere formulations varied significantly at short times, <2 hours, but were similar at long times >=12 hours.

3.3.2 βTC-6 Cell Activity Assay

GLP-1 is reported to induce proliferation of βTC-6 cells [49]. Increase in ßTC-6 cell number was dependent on GLP-1-SBP concentration under serum starved conditions, resulting in a 1.4 fold increase in the number of cells in comparison to the no treatment control (Figure 3-9) and with similar cell numbers to the Exendin-4 (GLP-1 analog) positive control treatment (Figure 3-10) . GLP-1-SBPs exhibited similar activity before immobilization and after microsphere release suggesting that there were no adverse

denaturing interactions between the microsphere and fusion peptide (Figure 25).

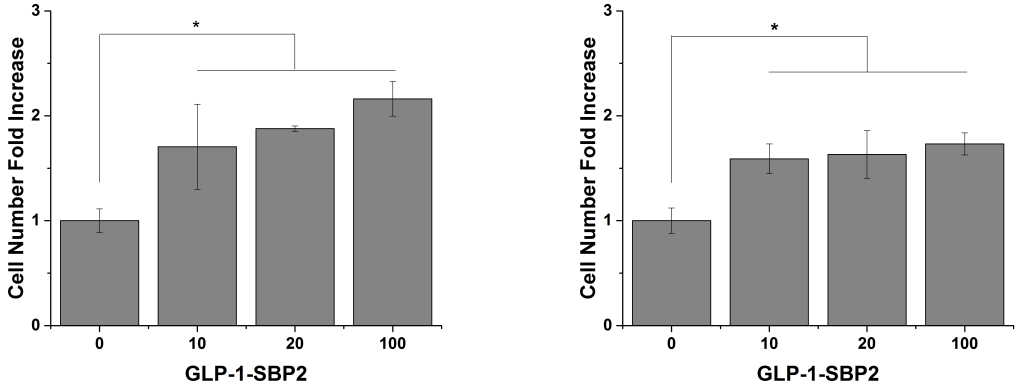

Figure 3-9 Cell-based GLP1-SBP activity assay. Treatment with increasing concentrations of GLP1-SBP significantly increased the number of ßTC-6 cells in comparison to the non-treatment control under serum-starved conditions; (left) 2% heat inactivated FBS, (right) 4% heat inactivated FBS. *P<0.05

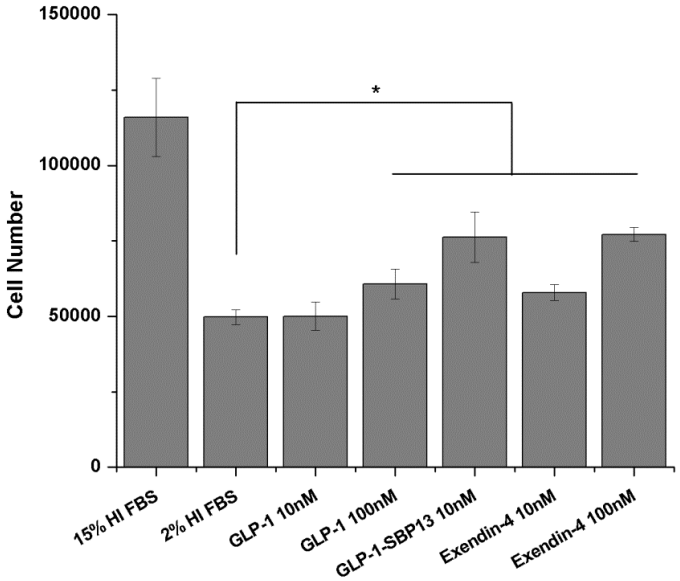

Figure 3-10 ßTC-6 cell number increased in response to incubation with soluble GLP-1-SBPs. Cells were treated every 2 days with soluble GLP-1-SBPs, GLP-1(Control), and Exendin-4 (Control) under starved conditions (2% heat inactivated FBS) until harvesting on day 7. Stimulation with GLP-1-SBPs and Exendin-4 led to significant increases in cell number at all concentrations. While significant increases in cell number were observed only for high concentrations of GLP-1 (100nM)

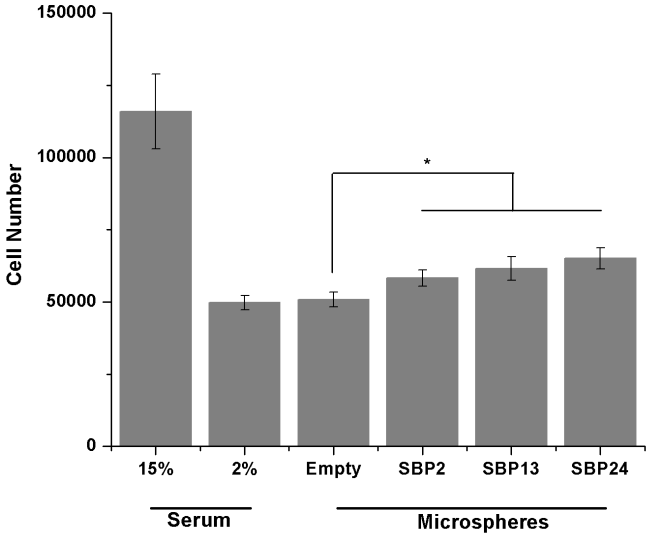

Figure 3-11 ßTC-6 cell number increased in response to incubation with GLP1-SBP loaded microspheres in transwell insert. GLP-1-SBPs released from microspheres retained activity; significant increase in cell number when compared to the no treatment (empty) microspheres was observed.

3.3.3 Insulin Secretion Activity

Baggio et al reported that chronic activation of GLP-1 receptors do not result in hypoglycemia due to the loss of insulinotropic effects of GLP-1 at low glucose concentrations *in vivo* [85]. This finding mirrored the glucose-dependent secretion of insulin after incubation of GLP-1 agonist with ßTC-6 cells. Insulin secretion increased with increasing glucose concentration (0, 3, and 16 mM), however maximal secretion was observed at 3mM glucose under co-stimulation by GLP-1. In the absence of glucose, Exendin-4 had no stimulatory effect on insulin secretion but showed significant secretion in the presence of 3mM glucose (Figures 3-11,-12). Repeated experiments with soluble GLP-1 analogs showed insensitivity to increasing stimulant concentration in 3mM glucose; there was no significant difference between basal and stimulated cases (Figures 3-13,-14). Cell-cell contact influences insulin secretion -- non-contacting beta-cells lose

glucose sensitivity while simultaneously increasing basal level insulin secretion [86]. Changes in cell number from plated to actual seeding at time of assay may account for the similarity between basal and stimulated cases in experimental repetitions. Similar results in insulin secretion were obtained for the microsphere-mediated GLP-1-SBP release (Figure 3-15) with possible common cause since the seeding density, which is a function of cell-cell contact [87]. Optimization of cell density in relation to maximal difference in insulin secretion compared to basal rates is important for experimental consistency for ßTC-6 cells. Additionally, exposure time of cells to soluble stimulant did not yield any significant change in insulin secretion which lends credence to a loss of cell sensitivity over low release quantities from loaded microspheres (Figure 3-16).

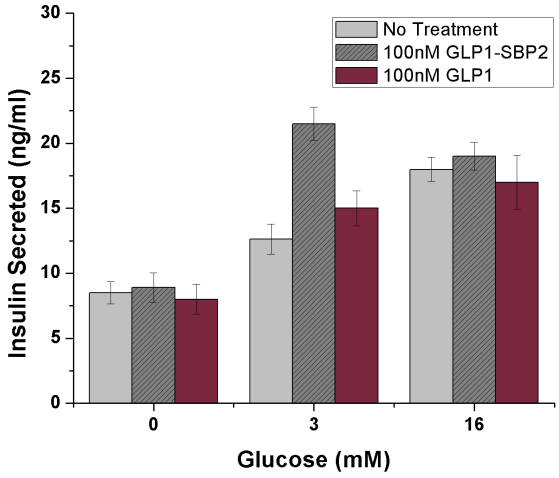

Figure 3-12 Optimization of insulin secretion by varying glucose concentration. Insulin secretion in ßTC-6 cells increased with glucose concentration in comparison to the basal insulin secretion at 0mM glucose. Maximal secretion was achieved with combined stimulation of 3mM glucose and 100nM GLP1-SBP2.

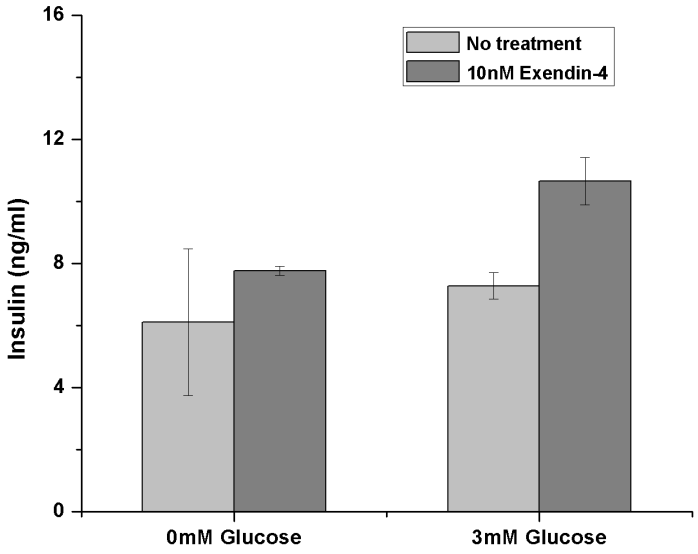

Figure 3-13 Glucose-dependent secretion of insulin. Exendin-4 treatment in the presence and absence of glucose with ßTC-6 cells. Exendin-4 treated cells stimulated significant quantities of insulin only in the presence of 3mM glucose. P<0.05

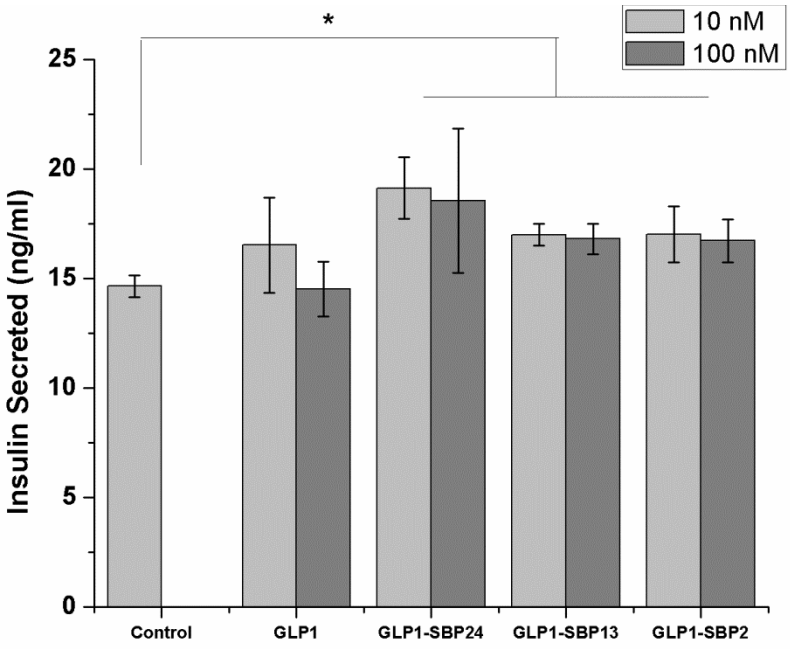

Figure 3-14 Insulin secretion in response to GLP-1 in 3mM glucose. GLP-1-SBPs induced increased insulin secretion compared to the 3mM glucose-only control in ßTC-6 cells. Treatment with GLP-1 (positive control) did not induce significant secretion.

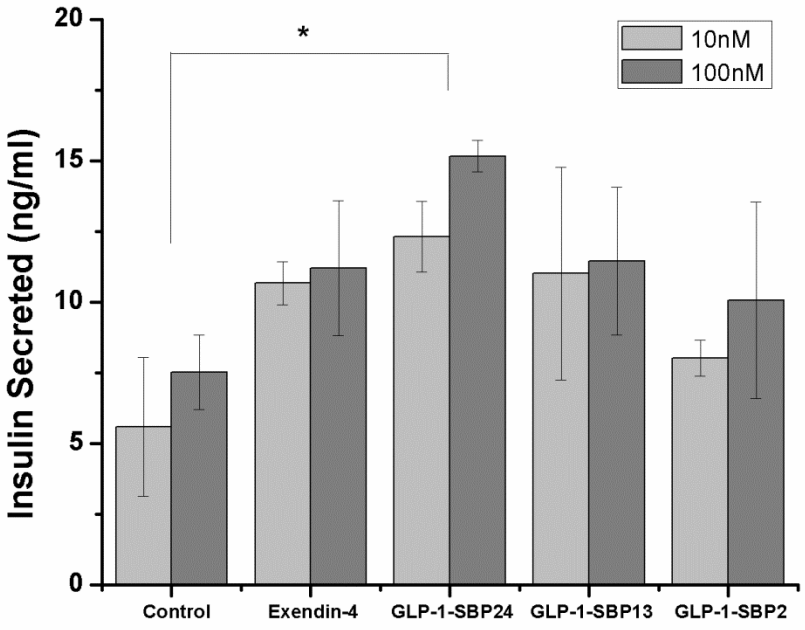

Figure 3-15 Insulin secretion assay. Repeated insulin secretion experiment with GLP-1 analog, Exendin-4, showed no significant increase in insulin in comparison to basal rates buffer. GLP-1-SBPs and Exendin-4 were incubated at low (10nM) and high (100nM) concentrations in 3mM glucose.

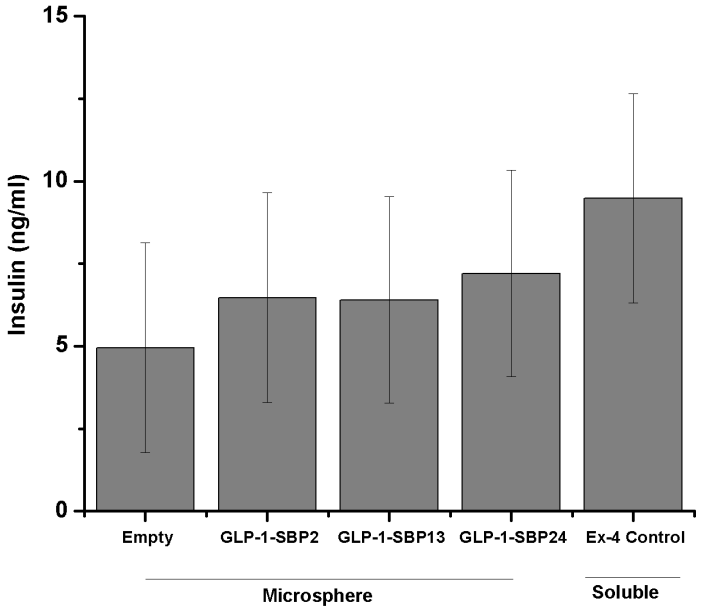

Figure 3-16 Insulin secretion activity of GLP-1-SBPs released from loaded microspheres. Released GLP-1-SBPs induced no significant insulin secretion after 2-hour incubation with ßTC-6 cells. Positive control Exendin-4 treatment resulted in a

non-significant increase in insulin secretion in comparison to the empty microsphere control.

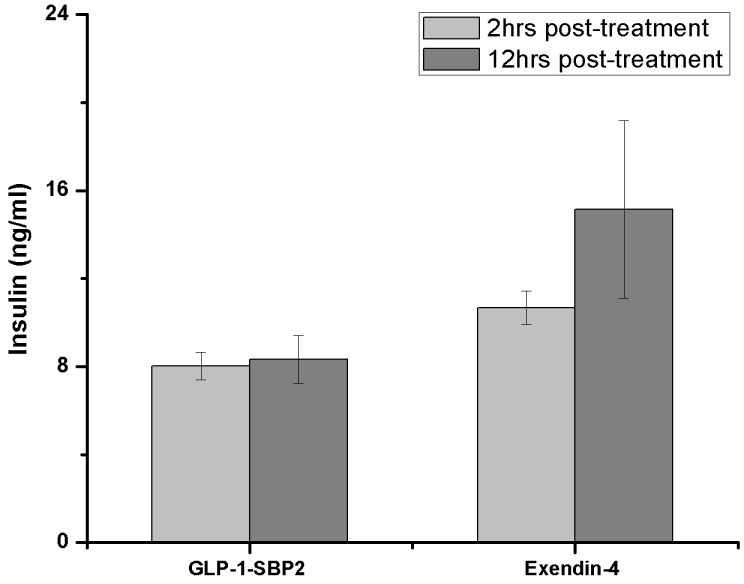

Figure 3-17 Time-dependence on insulin secretion. Soluble Exendin-4 and GLP-1-SBP2 showed no significant increase in insulin secretion with increasing time.

3.3.4 GLP-1-SBP Release

Preliminary release profiles examined the role of surface immobilization of SH3 in comparison to the effective functional area of SH3 microspheres (loading throughout microsphere as confirmed by confocal microscopy). Results showed comparable rapid release of GLP-1-SBP from both SH3 conjugated polystyrene particles and SH3 microspheres. These results suggested that diffusion through the SH3 microsphere was as rapid as surface released peptide. SH3 microsphere size remained unchanged post-release negating any dissolution contributions to the rapid release observed. Total peptide loading of the GLP-1-only control to SH3 microspheres confirmed minimal contributions from non-specific binding interactions, with a total loading of GLP-1 that was two orders

of magnitude lower than either GLP-1-SBP loading to SH3 microspheres or polystyrene particles.

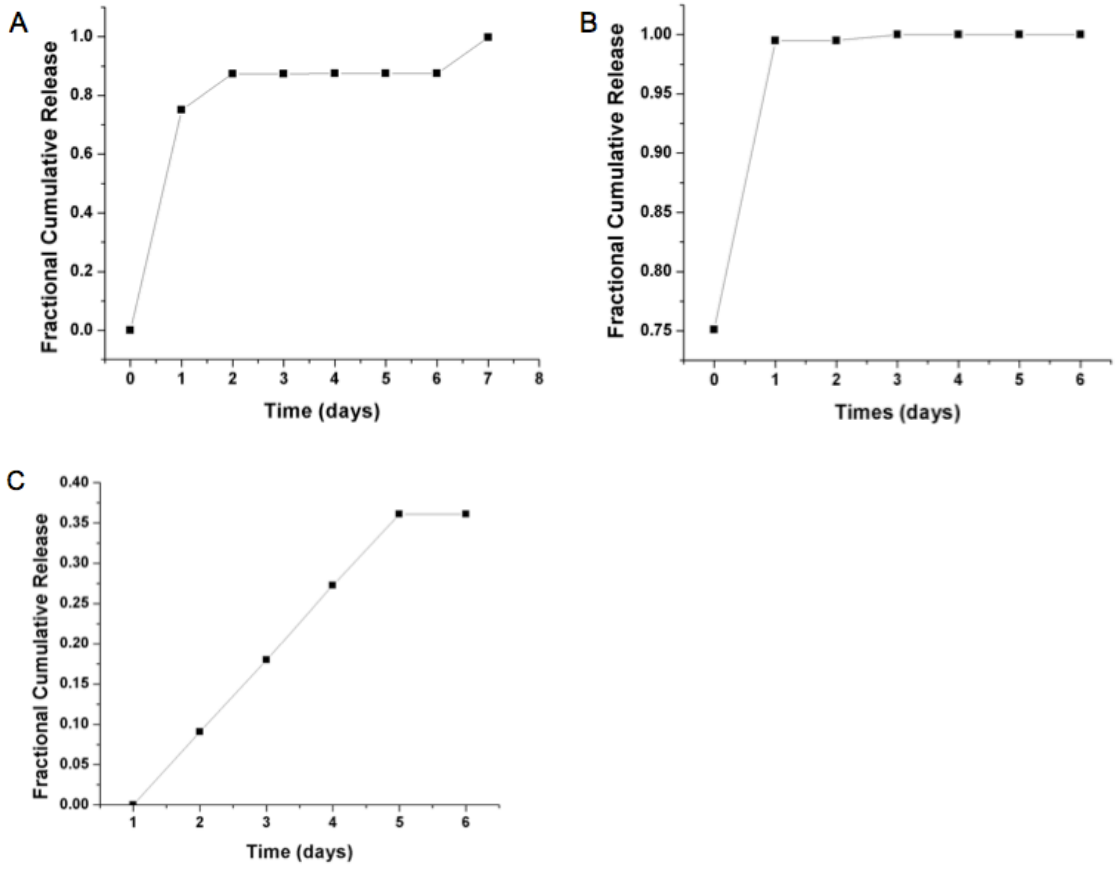

Figure 3-18 Preliminary release of GLP-1-SBP2 from microspheres. (A) Cumulative release from SH3 microspheres incubated with 5 mg/ml GLP-1-SBP2 resulted in rapid burst in a 24-hour period. (B) Release profile for GLP-1-SBP2 release from SH3 conjugated polystyrene surface. (C) Non-specific control, GLP-1, was released from SH3 microsphere at a slower rate than either specific-binding samples. The cumulative release was represented as a fraction of the total quantity loaded on microspheres/particles. Total GLP-1 loading was two orders of magnitude lower than GLP-1-SBP samples

Vulic et al describes a time scale of release typical of affinity-based systems in equation (10).

$$t_{final} = \frac{L^2(1 + \frac{C_{ligand}}{K_D})}{D} \quad (10)$$

Where L is the diffusion path length, D is the diffusivity of the peptide, K_D is the affinity between the peptide and binding ligand [88]. The term, $(1+ C_{ligand}/K_D)$, impedes pure diffusion-driven release (L^2/D). Thus, peptide concentration is independent of release rates. In atypical systems in which $C_{peptide} >> C_{ligand}$ diffusion-driven release governs initially since the attenuating term becomes $(1 + C_{ligand}/C_{peptide})$. It follows then that the rapid release experienced by both GLP-1-SBP specific binding systems may be attributable to high initial concentrations of the GLP-1-SBP peptide (Cpeptide $=20*C_{ligand}$). In subsequent release experiments, peptide concentrations in 2X molar excess of ligand concentration were used for loading, favoring affinity-driven release.

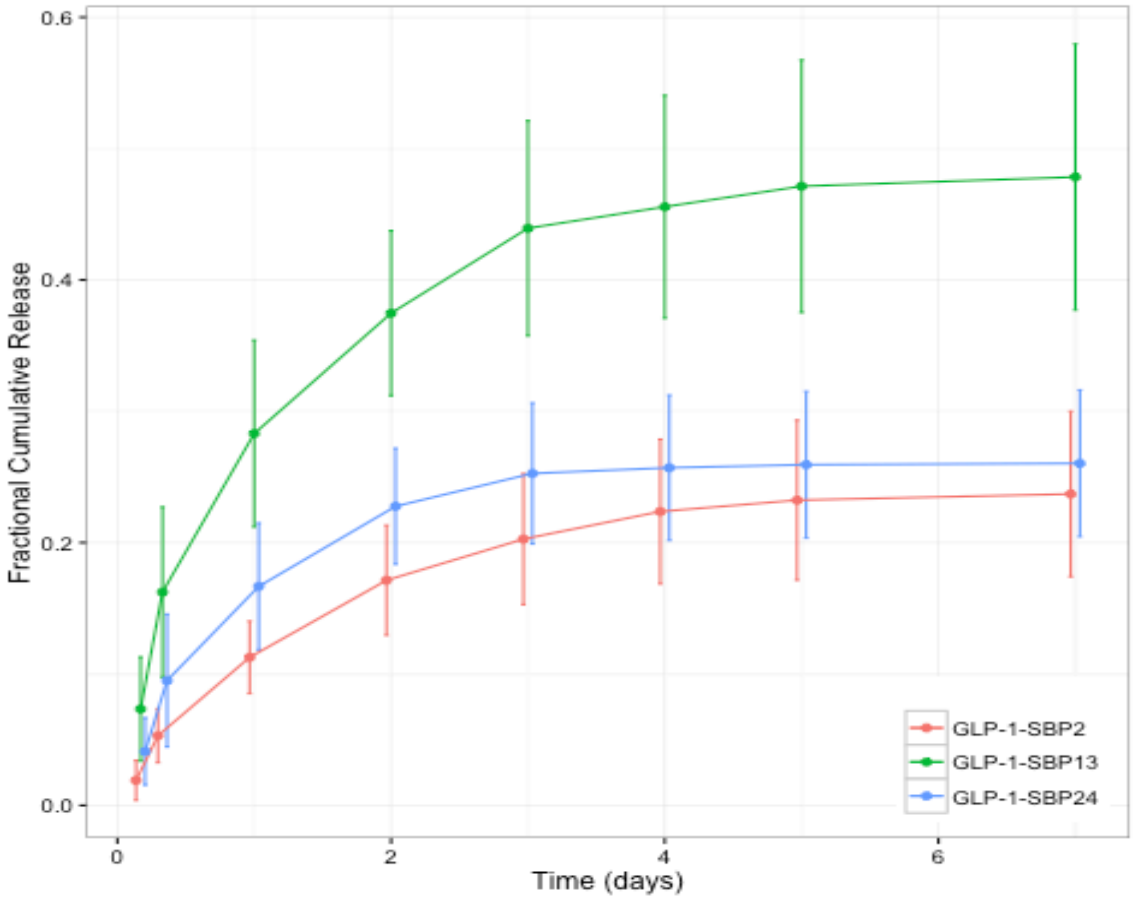

Figure 3-19 Release profile of GLP-1-SBPs delivered from SH3 microspheres. SH3-binding peptides attenuated the release of GLP-1 such that stronger binding peptide (SBP2) released at a slower rate than the weaker binder (SBP13). $p < 0.05$ for all groups, except between GLP-1-SBP2 and GLP-1-SBP13 at t = 4h. Weakest binding GLP-1-SBP24 showed an anomalous release profile.

Release rates were fastest for GLP-1-SBP13 (weaker binder), followed by GLP-1-SBP2 (strong binder), and were statistically significant ($p<0.05$) for all time points after 4 hours. This suggests that tunable release can be achieved through the variation of binding peptides. GLP-1-SBP24 (weakest binder) showed anomalous release; with release profile closer to that of the strong binder instead of the expected faster release than GLP-1-SBP13. This anomaly may be attributed to increased interaction of SBP24 with the elastin-like polypeptides present in the microspheres. Elastin-like polypeptides are known

to under phase transitions from randomly coiled conformations to ordered polyproline alpha-helical structures above a lower critical solution temperature [89,90]. SH3 binding peptide, SBP24, unlike SBP2 or SBP13, possesses repeat polyprolines. These polyprolines can form (PPII) alpha helical structures that interact with similar structures present on the ordered ELPs of the microspheres.

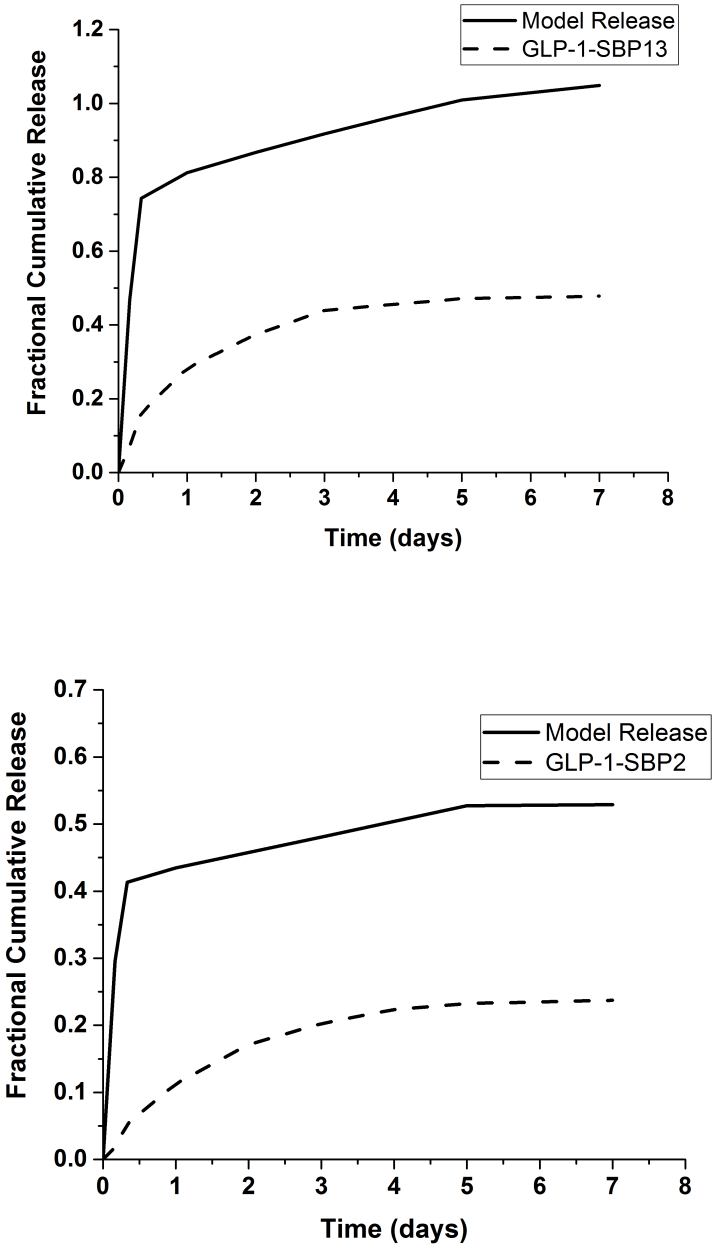

Figure 3-20 Mathematical model correlation to experimental release for GLP-1-SBP3 (top) and GLP-1-SBP2 (bottom).

The mathematical model described the influence of SH3 binding peptide affinity on the release of GLP-1-SBPs from the ELP-SH3 microspheres. Partial differential equations describing the reaction-diffusion kinetics of the diffusible species and mass balances of

all system species (equations 2-4) comprised the model. The model does not correlate well with experimental release (Figure 20), which is attributed to overestimation of model parameters. The model recapitulates the release trends. The estimated diffusivity coefficient and kinetic parameters used in the model contributed to the differences observed between the model and experimental data. Calculation of the apparent diffusivity (the slope of the cumulative release versus root time, Figure 21) showed discrepancy in the estimated diffusivity and the apparent experimental diffusivity. Apparent diffusivity was lower for the stronger binding SBP2 than for the weaker binding SBP13 suggesting that release rates were due to interactions between the affinity domains and not only slower diffusion of peptides through microspheres[91].

$$\frac{M_t}{M_\infty} = kt^{1/2} \qquad (11)$$

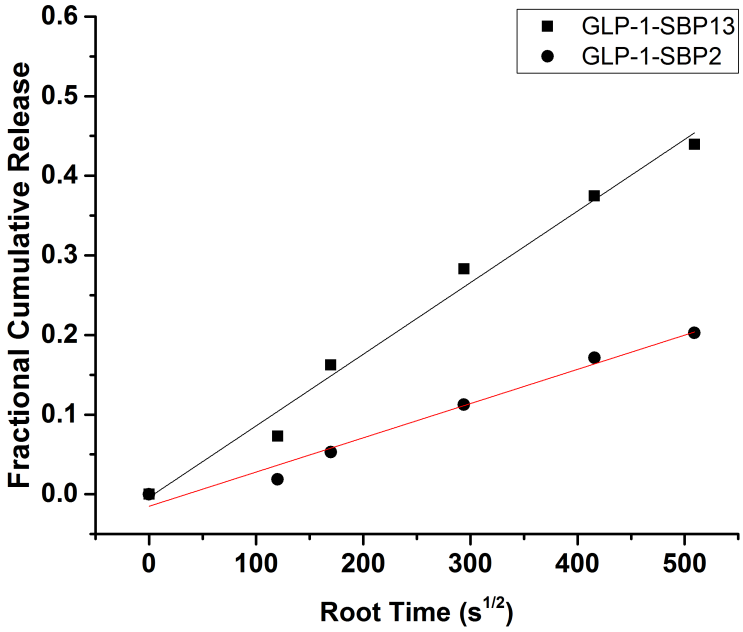

Figure 3-21 Release profiles of GLP-1-SBP2 and GLP-1-SBP13 were fit to a short time approximation (equation 11). The slopes are proportional to apparent diffusivity of the peptides through the microspheres.

3.4 Conclusion

In conclusion, exploiting SH3-SBP binding interactions is expected to provide a versatile platform for specific and controlled release of GLP-1. The use of self-assembling building blocks such as elastin-like polypeptides leads to bottom-up control of delivery system structure under conditions favorable to the retention of binding function. Therapeutic peptide fusion with SBP preserved activity while still allowing for release. A 20-40% release over a 7-day period suggests that this system can be used to effectively deliver GLP-1 therapeutic. Release profiles were dependent on the strength of SBP

affinity, with the weaker binding SBP13 releasing significantly faster than the stronger binding SBP2. Mathematical model results qualitatively predicted the trend of release for both GLP-1-SBP13 and -SBP2. Low quantitative correlation of model prediction to actual release profiles was attributed to the estimated diffusivity coefficient and the estimation of kinetic parameters based on larger molecular weight fusion SBPs. Control of system parameters such as ligand concentration, peptide concentration, and affinity could lead to a wider range of affinity-based release.

CHAPTER 4.

OUTLOOK AND FUTURE RECOMMENDATIONS

The affinity-based system developed by utilizing properties of affinity binding strength and self-assembly provides a modular approach to therapeutic peptide delivery. A diverse range of therapeutics have been successfully delivered using such affinity binding domains including growth factors VEGF, bFGF, NGF [14,92,93], and large globular proteins such as chABC [19]. Immobilization achieved without modification of the therapeutic, in the former examples, and through modification of therapeutics with an affinity-binding domain in the latter examples. Functionalization of the therapeutic with affinity domains offers more control over specificity of binding interaction, serving as the main driving force behind the SH3/SBP domain selection. Molecular control over particle fabrication, biocompatible fabrication conditions, and ease of assembly are the advantages of the elastin-like polypeptide building block selected. Preparation of ELP-SH3 components via expression in E. Coli and Inverse Thermal Cycling purification [83] could provide scalability at low cost.

To maximize SH3/SBP platform versatility, considerations of (1) affinity partner selection (2) ease of preparation of functionalized therapeutic (3) ELP-SH3 delivery system design (4) optimization of activity assay and (5) biomaterial interactions should be addressed.

1. Affinity Partner Selection

One of the potential pitfalls to therapeutic modification is the loss of structural stability and subsequent reduction in activity. Functionalization of therapeutic peptide with SBP affinity domain has resulted in successful preservation of structure, as attested by GLP-1-SBP and fibronectin-SBP [68]. However, this is not universal and SBPs also have the potential to destabilize dimeric growth factors. Preparation of SBP functionalized bone morphogenetic protein 4 (BMP4) resulted in the destabilization of intermolecular bonds resulting in irreversible aggregation. The use of very long (>12 aa) linker regions or the use of hydrophilic polymer linkers may mitigate the effects, though the latter may affect scalability. It is posited that SBP24 amino acid sequence allowed for increased interaction with the ELP-SH3 protein microspheres. SBP sequences can thus be exploited to further decrease release. Shoichet et al have successfully modified globular proteins with the larger SH3 affinity partner [20]; such modifications would necessitate optimization of a new ELP-SBP microsphere fabrication and affect release profiles.

2. Preparation of Functionalized Therapeutic Peptide

Bacterial expression of peptides is typically accomplished by fusion to high molecular weight solubility tags such as GST [94,95] to reduce peptide degradation during expression and facilitate purification. Enzymatic cleavage of solubility tags from peptides can potentially result in non-specific cleavage within the desired peptide thereby reducing function. Non-specific cleavage in the case of GST-GLP-1-SBP resulted in the loss of the SBP functionalization. Alternative preparation of peptides by chemical synthesis can become prohibitively expensive. Multiple repeating units of GLP-1 can be used to increase peptide molecular weight thus negating the need for enzymatic cleavage as well as increased secondary structure stability. Albiglutide™ (GlaxoSmithKline) incorporates

multiple units of GLP-1 to alleviate structure instability from albumin fusion. Since the active domain is located on the N-terminal of the GLP-1 peptide, all other tandem repeats act as linker domains. The GLP-1 sequence used here has been modified to evade DPPIV protease degradation (Chapter 2 of thesis), however, future design of linker regions and fusion partners should examine cleavage by other proteases and test for peptide stability to DPPIV over the course of release[67]. Kinetic parameter measurements of GLP-1, GLP-1-SBPs, and GLP-1-Scramble will increase mathematical model accuracy. The sensitivity of peptide quantification methods should also be considered. Current quantification methods that measure pg/ml-ng/ml released peptide are limited (e.g. ELISA, Mass Spectrometry with labeled peptide). Common also is the use of reverse phase high-pressure liquid chromatography (RP-HPLC), though the lower limit for reliable quantification at 215nm should be considered. Doping with radiolabeled peptide may increase the sensitivity of detection [96] even in complex release media or buffers.

3. Elastin-like Polypeptides Alternative Systems to Increase GLP-1 Loading

Gilroy and colleagues have extensively reviewed strategies for extending the circulation of GLP-1 analogs in a recent review [97]. Amino acid mutations, in an attempt to reduce protease degradation experienced by native GLP-1 (highlighted in Chapter 2), have been employed with Taspoglutide™ (Ispen/Roche), Exenatide™ or Byetta™ (Amylin/Eli Lilly), and Lixisenatide™(Sanofi). Strategies to increase the molecular weight through conjugations to fusion partners have also met with success. Albiglutide, multiple repeats of GLP-1 in tandem with human serum albumin (GlaxoSmithKline) increases circulation time. Liraglutide and Semaglutide (Novo Nordisk) through functionalization with palmitic acid moieties on the c-termini of GLP-1 allows for non-covalent and reversible

binding to serum albumin thereby prolonging circulation times. Dulaglutide (Eli Lilly) fuses GLP-1 monomers to Fc regions of immunoglobin G to extend half-life *in vivo*. Finally, GLP-1 analog fusions to polymers such as Polyethylene glycol, XTEN, and elastin-like polypeptides to increase circulation times are currently in the pre-clinical trial phase. While these strategies have met with some success in increasing circulation time, controlled release which aids in the delivery of quantities within relevant therapeutic thresholds and reduces toxicity is not achieved. These formulations therefore can only be modulated through injection frequency.

Bydureon, exenatide encapsulated within 20 - 60 μm PLGA microspheres, is one formulation that attempts to control the release of GLP-1 analog (Amylin) and remains the only FDA approved microsphere formulation to date. However, these microspheres are loaded with 14-28 times the required peptide quantity to account for losses during burst release and adsorption/denaturation with the polymer matrix. Polymeric microsphere encapsulation has been extensively used to control the release of therapeutic proteins, peptides, and small molecules, achieving release from weeks to months through optimization of polymer ratios. The challenge of reducing burst release effects continues to push innovation in such systems, and is the driving force behind the use of affinity-based systems in which such burst release are controlled (Chapter 1).

Specifically, for the encapsulation of GLP-1 analogs, formulations outlined in Table 2 were investigated.

Components	Preparation	Loading	Release Period	Ref:

1.**PLGA** microspheres 33.4-45.7 µm.	Metal cation-stabilization of GLP-1; S/O/O extraction	90% loading efficiency (1.8 mg) total loading per mg microspheres (RP-HPLC measured)	w/zinc Complexation: 3% burst release (6hrs) & additional 23% of total loading over 28 days. w/o zinc: 37% burst release (6hrs) additional 25% total dose over 28 days	Yin et al[98]
2.ABA-type triblock copolymer PLGA-PEG-PLGA (ReGel)	Zinc-complexed GLP-1 formulated in ReGel	10 mg total loading (via RP-HPLC)	w/zinc Complexation: no initial burst 90% release over 14 days. w/o zinc Complexation: 60% burst release (24hr) additional 20% (3 days)	Choi et al[99]
3.Porous silicon stabilized by thermal oxidation 185-250 m^2/g	GLP-1	45% w/w: 0.82mg/1mg microspheres (thermo gravimetric analysis, RP-HPLC)	40% burst release (1 hr) additional 60% in 1 day	Huotari et al[100]
4. 10 µm PLGA microspheres	PEG-Ex4	PEG-Ex4 in PLGA, Ex4 in PLGA	PEG-Ex4: 10.8% burst release with additional 80% over 18 days. Ex4: 43.8% in 3 days	Lim et al[73]

The ELP-SH3/ GLP-SBP affinity-based systems showed a reduction in the burst release of GLP-1-SBP with a 20-40% release of 50 µg total loading over 7 days. This reduction in burst release between SBPs was dependent on strength of affinity. 40% of GLP-1-SBP13 was released in the first 3 days with an additional 5% of release over the

remaining 4 days. 20% of GLP-1-SBP2 was released in the first 4 days with an additional 5% being release up to 7 days. Current twice-daily doses of Byetta deliver 5-10 μg per dose. In order to achieve similar therapeutic levels the affinity-based system has to be optimized.

Therapeutic release in affinity-based systems can be achieved through modulation of several parameters including affinity (K_D), system geometry, and ligand concentration[28]. Chapter 3 details the effects of varying SH3-binding peptide affinities. Increasing the size of the ELP-SH3 microspheres may increase their loading capacity, decrease potential phagocytosis, and extend release. However increased particle size may lead to more painful injections with larger gauge needles[34]. Elastin-like polypeptides have been used been used as scaffolds in tissue engineering, hydrogels, particles, and micelles for drug delivery[48,101]. Na and colleagues created 200μm porous microparticles with ELPs using the water oil w/o emulsion method[43]. Varying protein concentration, salt concentration, and fabrication methods can increase ELP-SH3 particle size. 50μM ELP-SH3 produces 3μm particles, increasing protein concentration from 100μM to 400μM at 300mM salt increased average particle diameters from 3μm to 5μm (Figure below).

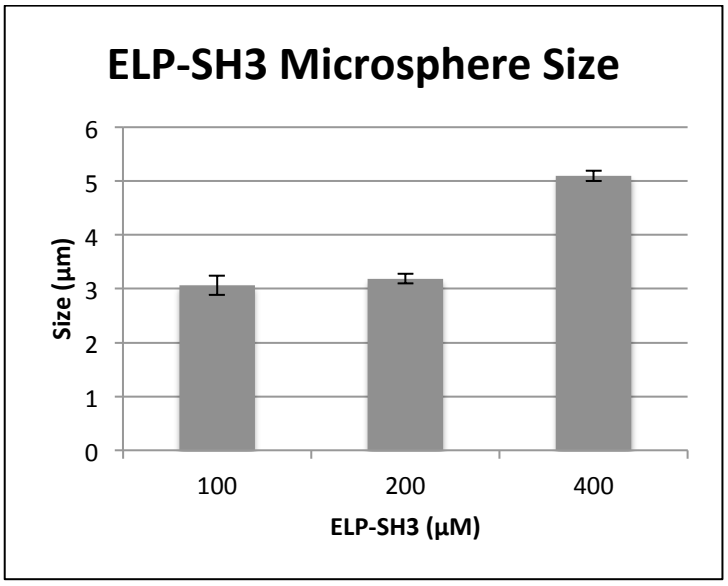

In situ gel formation to form ELP depots have also been investigated[67,102], though modification to the repeat units of the ELP to optimize transition behavior at body temperature is required. In situ formation will minimize painful injections due to large (>20µm) particle size. However, the tight control of storage and handling temperatures of the injectable system is required to avoid premature aggregation, and may be a considerable downside to this approach. Incorporation of pendant moieties within polymer hydrogels is another well-established way to present affinity-domains and may serve as another way to control SH3 ligand concentration, which affects loading and release. For example, heparin and/or heparin binding peptides have been covalently incorporated into Fibrin, PEG, Chitosan, and PLGA polymer delivery systems to facilitate release[15,103–105].

4. Optimizing Activity Assays

    a. Cell line Selection

ßTC-6, MIN-6, and INS-1 are cell lines that are physiologically relevant beta-cell models. These cell lines secret insulin in response to physiological ranges of glucose stimulation[87,106–108]. In this work the ßTC-6 cells showed high basal levels of insulin secretion upon stimulation. However, treatment with GLP-1 analogs did not produce significant insulin secretion levels above basal levels. GLP-1 analog stimulation of ßTC-6 cell typically results in a significant 2-3 fold increase in insulin secretion[109]. Optimization of cell density, stimulation time, glucose treatment protocol or change of cell line may serve to increase GLP-1 induced insulin secretion significantly above basal levels.

b. cAMP Detection Assay

GLP-1 analogs are known to both stimulate insulin secretion and increase cAMP levels (Thesis Chapter 2)[32,110]. cAMP production should be measured after dose-dependent stimulation by GLP-1-SBPs with controls; GLP-1-Scramble SBP, DPPIV resistant GLP-1, native GLP-1, ELP-SH3, and SH3 binding peptides.

c. EdU Incorporation into Beta cells

5. Stimulation of ßTC-6 cells showed significant but modest increases in cell number. GLP-1 analogs stimulate cell proliferation. Beta-cell proliferation can be measured via incorporation of the alkyne-containing thymidine analog EdU (5-ethynyl-2′-deoxyuridine) into DNA and detection by fluorescent azide through a Cu(I)-catalyzed [3+2] cycloaddition reaction [111].Biomaterial *In vivo* Interaction

Biomaterial properties play a crucial role in foreign body responses[112], microsphere size has also been found to influence foreign body responses[113]. *In vivo* response to loaded ELP-SH3 microspheres and microsphere components must be taken into account since

foreign body responses can influence particle degradation and bioavailability of released peptides. To determine the *in vivo* response to microspheres, ELP-SH3 microspheres and controls can be injected subcutaneously on the backs of mice. Microsphere implants and surrounding tissue can be explanted and fixed for histochemistry analysis. While Elastin-like polypeptides are derived from ECM components and do not elicit immune responses, the immunogenicity of delivery systems prepared from ELPs in combination with other components must be determined[114]. Measurement of antibodies against microsphere components in plasma can determine the immunogenicity of the delivery system.

Plasma concentration of GLP-1-SBP released from ELP-SH3 microspheres at different time intervals is required to determine efficacy in vivo[73]. To determine the extent to which GLP-1-SBP loaded microspheres can reduce glucose levels over a long period, in vivo monitoring of glucose levels and intraperitoneal glucose tolerance test (IPGTT) in diabetic mouse models is necessary [67]. Endotoxin levels in microsphere components must be determined before in vitro and in vivo studies.Immobilization of varied SBPs in combination within SH3 microspheres is expected to modulate the release, allowing for specific immobilization and controlled co-delivery of therapeutic peptides.

CHAPTER 5.

QUANTITATIVE ANALYSIS OF THE ROLE OF FIBER LENGTH ON PHAGOCYTOSIS AND INFLAMMATORY RESPONSE BY ALVEOLAR MACROPHAGES

5.1 Summary

In the lung, macrophages attempt to engulf inhaled high aspect ratio pathogenic materials, secreting inflammatory molecules in the process. The inability of macrophages to remove these materials leads to chronic inflammation and disease. How the biophysical and biochemical mechanisms of these effects are influenced by fiber length remains undetermined. This study evaluates the role of fiber length on phagocytosis and molecular inflammatory responses to non-cytotoxic fibers, enabling development of quantitative length-based models. Murine alveolar macrophages were exposed to long and short populations of JM-100 glass fibers, produced by successive sedimentation and repeated crushing, respectively. Interactions between fibers and macrophages were observed using time-lapse video microscopy, and quantified by flow cytometry. Inflammatory biomolecules (TNF-α, IL-1 α, COX-2, PGE_2) were measured. Uptake of short fibers occurred more readily than for long, but long fibers were more potent stimulators of inflammatory molecules. Stimulation resulted in dose-dependent secretion of inflammatory biomolecules but no cytotoxicity or strong ROS production. Linear cytokine dose-response curves evaluated with length-dependent potency models, using measured fiber length distributions, resulted in identification of critical fiber lengths that cause frustrated phagocytosis and increased inflammatory biomolecule production. Short

fibers played a minor role in the inflammatory response compared to long fibers. The critical lengths at which frustrated phagocytosis occurs can be quantified by fitting dose-response curves to fiber distribution data.

5.2 Introduction

Phagocytosis by macrophages is critical in the degradation and clearance of pathogenic materials in the body [115]. High aspect ratio materials such as asbestos fibers or carbon nanotubes can be cleared by phagocytosis or persist and induce frustrated phagocytic interactions leading to chronic inflammation, oxidative stress, direct cell injury, and chromosomal abnormalities [116–119]. This evasion can lead to diseases such as fibrosis, asbestosis, lung cancer, mesothelioma for asbestos-like materials, and carbon nanotubes have recently been shown to induce asbestos-like chronic inflammation. In this work we define frustrated phagocytosis as the failure to engulf after attaching, spreading and manipulation of fibers by macrophages. The extent to which high aspect ratio materials evade clearance is strongly length-dependent, both *in vivo* and *in vitro* [120–131]. However, there is no consensus about a critical length beyond which materials persist, as these studies are confounded by other material physicochemical properties such as diameter and surface chemistry, or by cell type and location within the body.

For asbestos specifically, comparative study of length-based contributions between different types remains challenging since they possess different physicochemical properties and lead to varied disease endpoints and health outcomes, ranging from cancerous lesions to genotoxicity [132–135]. *In vivo* study of the role of fiber length on disease endpoints is further complicated by other length-dependent processes, which can

obscure any correlation of residual fibers with the disease endpoint. *In situ* fiber breakage reduces the population of long fibers and increases the population of short fibers [136]. *In situ* dissolution reduces fiber diameter, which may then lead to additional breakage [137,138]. Phagocytosis removes shorter fibers, changing the length distribution over time. Translocation reduces the fiber population at the deposition site and, together with all clearance mechanisms, may have an efficiency that depends on fiber length [139]. It is thus difficult to associate unambiguously fibers recovered in pathology with those that have induced disease. In *in vitro* experiments, after an induction time, macrophages will successfully engulf short fibers, and we lose the information of whether the short-fiber/cell interaction differs from the long-fiber/cell interaction. Therefore, we need to monitor cell-fiber interactions on short timescales following initial contact. An *in vitro* model that quantitatively captures all length-based contributions to the cellular response is critical to understanding pathogenic mechanisms.

A challenge in studying the effect of fiber properties in biological systems is the difficulty in obtaining fiber samples with well-controlled physical properties. The Baron dielectrophoretic classifier enabled earlier studies with length-separated glass fibers [129,130], while the use of JM-100 model glass fibers decouples fiber length from surface chemistry. Blake et al. [129] and Ye et al. [130] revealed a length-dependent cytotoxicity and induction of inflammatory cytokines after exposure of alveolar macrophages to glass fibers of varied lengths *in vitro*. However, while the Baron classifier can prepare short fibers with a narrow distribution of lengths, the long fibers are inherently broad in their length distribution. Without characterization of long fiber length distributions, it is not possible to attribute a critical fiber length to the cellular responses reported.

Here we present a quantitative assessment of phagocytic and inflammatory responses of MH-S murine alveolar macrophages to long and short populations of JM-100 glass fibers with well-characterized fiber distributions. Parameterization of the length distributions enabled the development of models that propose critical lengths for varied phagocytic interactions between fibers and cells. These length-dependent interactions were captured by time-lapse microscopy and flow cytometry. Production of inflammatory biomolecules, tumor necrosis factor α (TNF-α), Interleukin-1 α (IL-1 α), cyclooxygenase-2 (COX-2), and prostaglandin E2 (PGE_2), was quantified after macrophage exposure to short and long glass fiber populations. These pathological hallmarks are evidence of macrophage activation and fiber-induced inflammatory signaling [131]. We used the dose-response curves of the directly-stimulated cytokines (TNF-α, IL-1 α) to identify critical fiber lengths that increase inflammatory biomolecule production in macrophages during frustrated phagocytosis of long fibers.

5.3 Experimental Details

5.3.1 Fiber sample preparation

Fibers were prepared from a Pall glass fiber depth filter sheet, type AE binder free (Pall Life Sciences, Ann Arbor, MI, available as SKC no. 225-7-07, SKC Inc., Eighty Four, PA). This media consisted of entangled uncoated borosilicate glass fibers (of nominal diameters 0.1 μm < d < 10 μm), designed to retain 1-μm particles on liquid filtration. Batches of 24 sheets were cut out to fit into a 1¼" die cavity and crushed with a lab press for 60 seconds. Short fibers were obtained by crushing at 10 tons and re-crushed at 15 tons, while long fibers were crushed at 2 tons. Each batch yields ~ 1.3 g of fiber [140].

Individual fibers were liberated from the residual fibrous mat after crushing through suspension in 500 ml of DI water and sonication (Fisher Scientific Sonic Dismembrator Model 500 with ½" horn), at 50% amplitude (i.e. tip amplitude ~ 76 μm), for 30 minutes (1 second on, 1 second off). This procedure was followed to prepare the stock suspension of short fibers (no sedimentation step). The long fiber samples were allowed to gravitationally settle for 20 minutes, with the resulting supernatant decanted. The sediment was re-suspended in 500 ml and sonicated as described above. This sonication, settling, decanting, re-suspension procedure was iterated 10 times; the 10^{th} sediment constituted the long fiber sample. All samples were prepared for diameter measurement by vacuum filtering 1 mL of a 1000:1 dilution through a 0.8 μm nitrocellulose filter (Millipore AAWP 02500); deposition is nominally ~ 1 $\mu g/cm^2$.

5.3.2 Fiber length measurement

All fiber samples were subjected to a final filtration through a 35 μm mesh to separate entangled fibers before length measurement and exposure to macrophages. Fibers were imaged (see Time-Lapse Video Microscopy section) on an incubation stage of an Axio Observer Z1 inverted light microscope (Carl Zeiss Microscopy, LLC, Thornwood, NY) and observed using differential interference contrast at 100X magnification. This imaging differs from the typical phase contrast microscopy analysis of fibers collected on acetone cleared MCE filters [141,142].

The length of the fibers was measured, using the line tool from Motic Images Plus 2.0 ML (Motic Group, Richmond, BC, Canada); faint fibers were identified with the aid of

the magnification tool at 200% magnification. Only fibers entirely contained within the field of view were included for length measurement; this restriction actually biases the measured length distribution against the longer fibers, but since the dimensions of the field of view (220 μm x 170 μm) are quite large compared to almost all of the measured fibers, this distortion was neglected (Turkevich, unpublished). At this magnification, 1 μm represents the image resolution limit.

5.3.3 Fiber diameter measurement

Fibers were imaged with scanning electron microscopy (SEM) to analyze fiber diameter. The nitrocellulose filters were mounted on 25 mm planchettes or stubs, using colloidal graphite adhesive, and were sputter coated with gold, to prevent charging by the electron beam. The samples were analyzed using a Hitachi S3000N scanning electron microscope. Secondary electron images were obtained at an accelerating voltage of 25 keV. Images were taken at 800X and 4000X. The length and diameter of the fibers were again measured using the line tool from Motic Images Plus 2.0 ML. At 800X, fiber diameter quantitation was not possible below 0.25 μm; at 4000X, fiber diameter quantitation was not possible below 0.15 μm.

5.3.4 Fiber count

Serial dilutions of suspended fibers were counted using a haemocytometer mounted on a light microscope at 40X magnification; fiber counts were accepted when the difference in

count among serial dilutions was less than 5%. Short fiber counts were verified by an Accuri C6 flow cytometer (Becton Dickinson). Dose-response experiments were reported as a function of optically detected (40X mag) fibers/cell.

5.3.5 Fiber labeling with fluorescent probe

Approximately 1.5 mg of glass fibers were suspended in 1 mL of 1 M KOH by sonication (pulse mode; 4 sec on, 2 sec off; 30% amplitude; 2 min total process time) and incubated for one hour. Fibers were washed with 1 mL deionized water (18.3MΩ.cm@ 25^{o}C) followed by a wash with 1 mL ethanol. Washes consisted of centrifuging the fibers at 125 x g for 5 min, 2400 x g for 10 min, and 21,000 x g for 1 min. To maximize fiber retention while minimizing breakage of fibers, the fiber pellet was retained after each centrifugation step and only the supernatant was centrifuged in the next step. Fibers were dried in an oven at 37°C for 1.5 hours. Fibers were then incubated for 2 min in a solution of 1 mL toluene and 33 µL 3- mercaptopropyl trimethoxysilane, washed with excess toluene to remove unconjugated silane, and suspended in 1 mL of 20 mM N-[Tris(hydroxymethyl)methyl]-2-aminoethanesulfonic (TES) sodium salt buffer solution. 15 µl of 20 mM of 5-iodoacetamidofluorescein (5-IAF) in dimethyl formamide (DMF) was added. The reaction was allowed to proceed in the dark for 2 hours at 4^{o}C under constant stirring. Fibers were washed twice in deionized water by centrifugation at 125 x g for 5 min, 2400 x g for 10 min, and 21,000 x g for 1 min to remove unreacted reagents before exposure to cells.

5.3.6 Alveolar Macrophages

Immortalized MH-S murine alveolar macrophages (ATCC-CRL2019) were used as model macrophages. They were cultured in RPMI media supplemented with 10% fetal bovine serum, 1% penicillin-streptomycin, and 50 μM beta-mercaptoethanol at 37^{o}C in a humidified atmosphere containing 5% CO_2. MH-S macrophages possess increased homogeneity of response in comparison to their highly heterogeneous primary macrophage counterparts. The cytokine response is known to differ among primary macrophage cell type. Immortalized cells are less responsive to cytotoxic stimuli and are thus ideal as model macrophages for dose-response testing of stimuli that are typically cytotoxic at high doses.

5.3.7 Time-lapse video microscopy

Macrophages, 3.2 x 10^4 cells/cm^2 in culture media, were seeded in a glass bottom dish and placed in an incubation stage on an Axio Observer.Z1 inverted microscope (Carl Zeiss, Inc.) and observed using differential interference contrast at 100X magnification. Cells were allowed to attach for 1 hour before short or long fibers were added to the center of the dish. Images of fiber-cell interactions were captured every 2 min by a Zeiss AxioCam camera for 24 hours. Images were collected and compiled into videos using AxioVision software and manually analyzed for cell-fiber interactions. Successful phagocytic internalization was characterized by membrane ruffling at the site of attachment, blurring the crisp boundary of the membrane, and subsequent reforming of the membrane boundary after internalization. In addition, a fiber was only classified as

internalized if it remained within the cell membrane boundary for the remaining observation period. Fibers with incomplete internalization and/or attachment were seen to cross the cell membrane of mobile cells.

5.3.8 Quantification of fiber internalization and attachment

Macrophages were plated at 5.3 x 10^4 cell/cm^2 in a 48-well plate and incubated for 24 hours. Cell culture media was replaced with identical media containing fibers at concentrations of 5, 10, and 20 fibers/cell for 24 hours. Cells were harvested by scraping, centrifuged at 125 x g for 5 minutes followed by suspension in 200 µl PBS. Fiber internalization and attachment events were distinguished by the use of trypan blue, which quenches fluorescence of externally bound fibers but not internalized fibers. Half of each cell sample was mixed with equal volumes of either PBS (unquenched) or trypan blue (quenched), and filtered with 35 µm mesh. Cell fluorescence was measured with an Accuri C6 flow cytometer. The cell populations were gated to exclude free fibers not associated with cells. Cells were identified as associated with fibers if their fluorescence was greater than cell autofluorescence measured in the absence of fibers for both the trypan blue quenched and PBS unquenched conditions.

5.3.9 Inflammatory Biomolecule and Cytotoxicity Measurements

Macrophages were seeded in 6-well plates ($5.3x10^4$ cells/ cm^2) for COX-2 and PGE_2 measurements, and in 96-well plates ($1.6x10^5$ cells/ cm^2) for TNF-α and IL-1 α

measurements, for 24 hours. Cell culture media was replaced with identical media containing fibers at concentrations of 5-15 long fibers/cell and 10-150 short fibers/cell. Bacterial lipopolysaccharide (1 μg/mL LPS) was used as an inflammatory stimuli positive control. After 24 hours of cell-fiber incubation, supernatants were harvested for TNF-α, IL-1α, and PGE_2 and interrogated by ELISA following R&D Systems (Minneapolis, MN) instructions. Supernatants were also used to determine cytotoxicity by detection of lactate dehydrogenase (LDH) with a colorimetric assay based on the reduction of pyruvate from Thermo Scientific (Waltham, MA). Cell lysates were collected and used for COX-2 ELISA (R&D Systems) following the manufacturer's instructions. All cell fiber conditions were repeated in triplicate, and results were validated with three separate preparations of short and long fibers.

5.3.10 Reactive Oxygen Species (ROS) Production

Macrophages were seeded in 48-well plates (5.3 x 10^4 cell/cm^2) for 24 hours prior to pretreatment with 10 μM dose of the non-fluorescent, membrane-permeable dye 6-carboxy-2',7'-dichlorodihydrofluorescein-diacetate(carboxy-H2DCFDA, ThermoScientific, Grand Island, NY) at 37°C for 20 min. Esterases in the cells convert carboxy-H2DCFDA to the charged form to increase intracellular retention. Cells were then washed with PBS before treatment with short and long fibers for 24-hours as detailed in the inflammatory biomolecule and cytotoxicity section above. Carboxy-H2DCFDA is chemically reduced by intracellular reactive oxygen species (ROS) to

become fluorescent. Cell fluorescence was detected using a fluorescent plate reader (Biotek, Winooski, VT)

5.3.11 Statistical analysis

Data are presented as mean ± standard deviation of the mean of representative experiments. Group means were compared using Student *t* test or one-way analysis of variance. $P<0.05$ was considered statistically significant.

5.3.12 Length-derived parameters and model fitting

In our fitting of these models, the length distribution of the fibers is represented by log-normal distribution,

$$f(\ln(L)) = (2\pi\sigma^2)^{-\frac{1}{2}} * \exp\left[\frac{-(\ln(L)-\mu)^2}{2\sigma^2}\right], \qquad (1)$$

with parameters;

$$\text{Short fibers: } \mu = 1.946 = \ln(7.0) \ and \ \sigma = 0.971$$

$$\text{Long fibers: } \mu = 3.671 = \ln(39.3) \ and \ \sigma = 0.739$$

Similar determinations could have been made directly using the length histograms; however, the shot noise inherent in the finite binning of the histograms introduces additional interpolation uncertainty.

Since the fiber populations differ only in their length distributions, for the case of direct stimulation, the ratio of the slopes of the dose-response curves depend on a potency function, p(L), averaged over the length distribution: <p(L)>. In each of the three models, the function p(L) is defined and <p(L)> is calculated.

Model 1 - Length cut-off, L_c

Model assumption - Fibers shorter than L_c elicited no cytokine response, while all fibers longer than L_c contributed equally to the cytokine response. The potency function $p(L)$ is given by:

$$p(L) = \begin{cases} 0, & L < L_c \\ p_0, & L > L_c \end{cases} \qquad (2)$$

The model attributes fiber potency to the number of fibers not internalized by macrophages, generating an average potency

$$< p > = p_0 \, [\, 1 - cum(L_c)], \qquad (3)$$

where $cum(L)$ is the cumulant of the fiber length distribution. For a log-normal fiber distribution (1), the average potency (3) becomes.

$$< p > = \left(\frac{p_0}{\sigma}\right) erfc\left[\frac{ln(L_c) - \mu}{\sqrt{2\sigma}}\right] \qquad (4)$$

where erfc(x) is the complementary error function.

Model 2 - Power-law Potency

Model assumption - Fiber potency varies as a power law of the length, weighting very long fibers as more 'problematic' for macrophages.

$$p(L) \sim L^{\alpha} \tag{5}$$

For a log-normal length distribution (1), the average potency becomes

$$< L^{\alpha} > = \ exp\left(\alpha\mu \ + \ \alpha^2 \frac{\sigma^2}{2}\right) \tag{6}$$

Model 3—Power-law Potency with a Cut-off

Model assumption - Fibers shorter than a cut-off, L_c, do not elicit a cytokine response from macrophages, while fibers longer than this cut-off elicited a response that scales as a power of the length.

$$p(L) = \begin{cases} 0, \ L < L_c \\ p_0 L^{\alpha}, \ L > L_c \end{cases} \tag{7}$$

In this model, those fibers that are internalized by macrophages do not contribute to the cytokine response, and, of the *non-internalized fibers*, the longer ones are more potent. For a log-normal distribution (1), the average potency becomes

$$< p > = \left(\frac{p_0}{\sigma}\right) * \ exp\left(\alpha\mu \ + \frac{\alpha^2\sigma^2}{2}\right) * \ erfc\left[\frac{ln(L_c) - \ \mu - \alpha\sigma^2}{\sqrt{2\sigma}}\right] \tag{8}$$

where, again, erfc(x) is the complementary error function.

5.4 Results

5.4.1 Fiber length and diameter distribution

Subsequent to their separation into “short” and “long” populations by high pressure crushing, and low pressure crushing followed by repeated sedimentation, respectively, the diameter and length of fiber samples were measured. Figure 1 shows the length distributions of the two populations. The fiber length distributions were confirmed to be log-normal (Figure 5.1 inset) where mean length, μ, was 7.0 μm and 39.3 μm for short and long fibers, respectively. Electron micrographs of typical short and long fibers are shown in Figure 5.2. Fiber diameter is centered around d ~ 0.8 μm and is uncorrelated with fiber length (Figure 5.3).

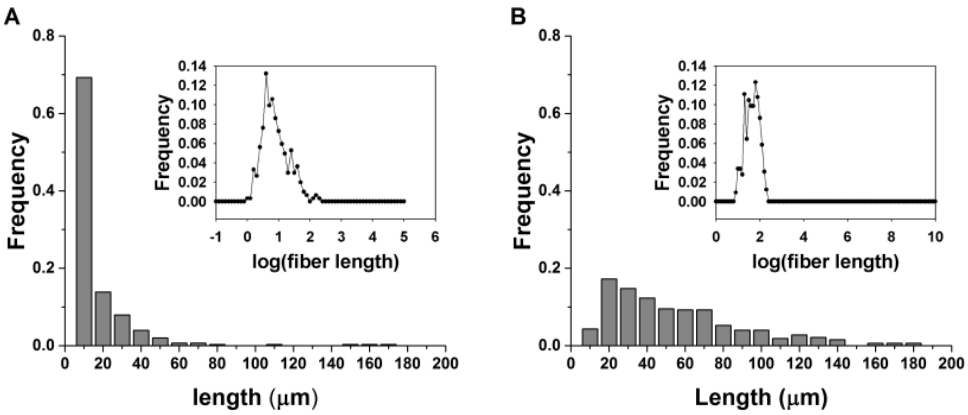

Figure 5-1 Fiber length distribution. Representative histograms of the length distributions of (a) short and (b) long fibers. Both populations exhibit a log-normal distribution for fiber lengths (inset).

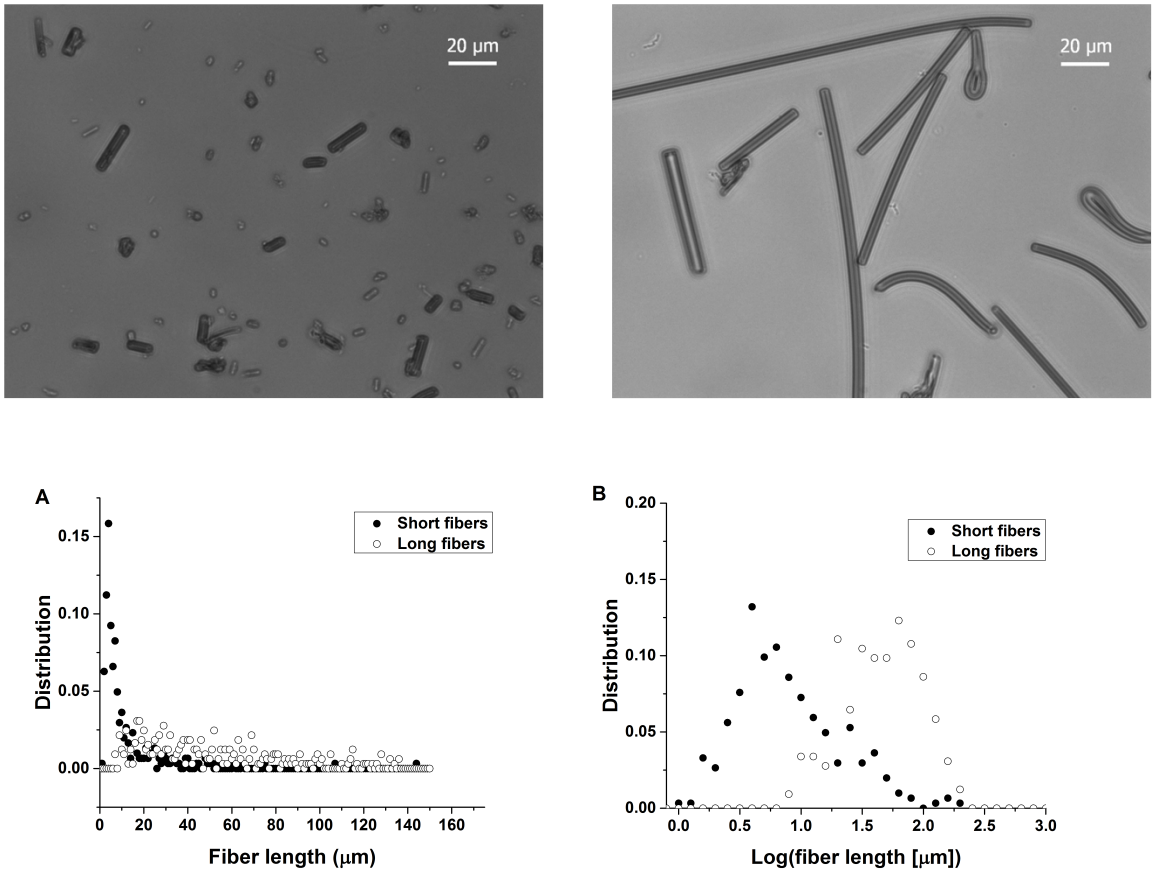

Figure 5-2 . Morphology of fiber and fiber length distribution. Top panels: Typical short and long fibers, as measured by light microscopy. Bottom panels: Statistics of the measured length showed (a) a long tail on the linear scale, and (b) a normal distribution on the logarithmic scale, characteristic of a log-normal distribution of fiber lengths

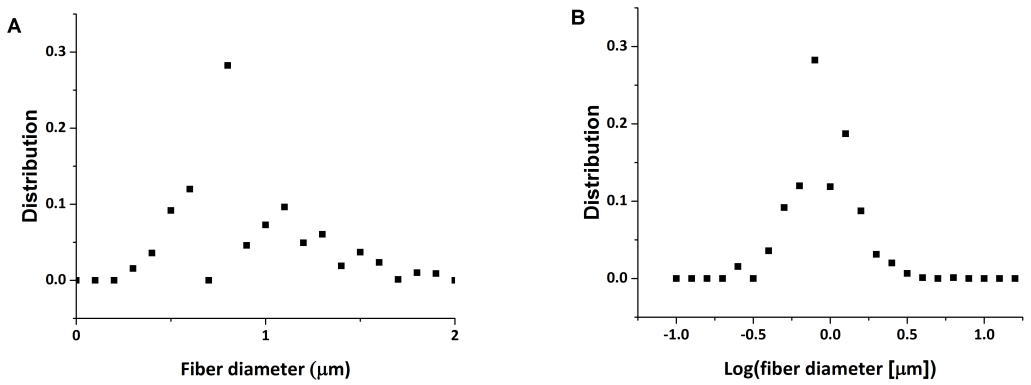

Figure 5-3 Fiber diameter distribution. Fiber diameters as measured by scanning electron microscope 4000 X. Fiber distribution on a (a) linear scale and (b) logarithmic scale.

5.4.2 Fiber-cell interactions

The immortalized murine MH-S alveolar macrophage cell line was used as a model to examine the role of glass fiber length in uptake, cytotoxicity, and inflammatory response. Real-time images of fiber-cell interactions were captured using time-lapse microscopy. A total of twenty-five fiber-cell interaction events, in which fibers either attached to or were internalized by macrophages, were recorded. Figure 4 provides snapshots showing representative interactions -- internalization of a short fiber and frustrated phagocytosis of a long fiber. Cell membrane ruffling can be seen at the site of attachment to the short fiber with subsequent blurring of the crisp boundary of the membrane. A membrane boundary reformed after the fiber is completely engulfed by the cell with the fiber remaining in the same focal plan and relative position within the cell . The cell interacting with the long fiber can be seen to attach with a pseudopod-like projection, pull the fiber toward it, and spread along a small region of the fiber. It is evident that the cell can exhibit significant force on the fiber as it flips the fiber vertically

180°. The scenario in which the macrophage is 'speared' on the fiber was never observed, nor was any cell blebbing upon fiber-cell interactions. Internalization events were fewer for long fibers in comparison to short; 25% of cell binding events with short fibers resulted in phagocytic internalization, while only 12% of long fiber binding events were internalization events. Only frustrated phagocytosis was observed to occur for fibers greater than 16 μm.

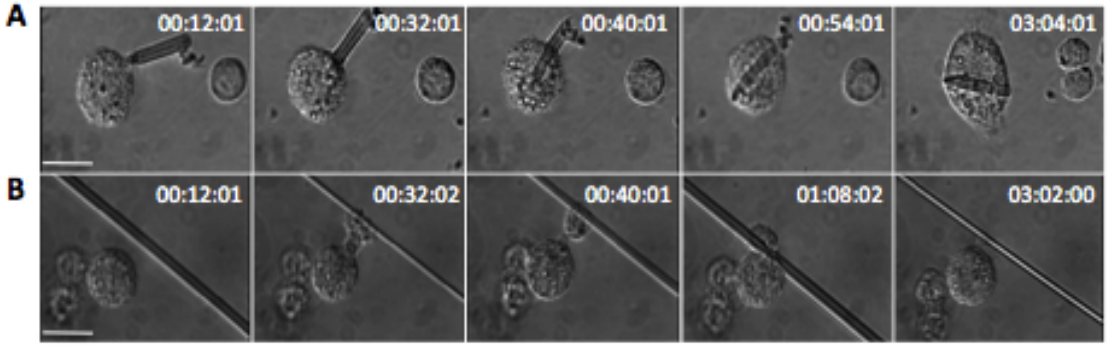

Figure 5-4 Time-lapse video microscopy frames of macrophage-fiber binding events. (A) A short fiber being internalized by a macrophage. (B) A macrophage attaching to and pulling a long fiber toward itself without internalization. Scale bar: 20 μm, Time: 0-3 hrs

For high throughput quantification of fiber-cell, fibers were covalently conjugated with fluorescent probe IAF (5-Iodoacetamidofluorescein) for detection by flow cytometry. Cell fluorescence was measured in the absence or presence of extracellular fluorescence quenching agent trypan blue to measure the combination of attached and internalized fibers or only internalized fibers, respectively. This measurement counts relative populations of cells but does not yield information on, the number of fibers associated with a cell. Therefore, internalization refers to the complete phagocytosis of *at least one* labeled fiber, and attachment refers to attachment of *at least one* labeled fiber.

The cells exhibited a dose-dependent increase in total short fiber interactions, but the *relative* fraction of cells with internalized fibers compared to attached was independent of concentration (Figure 5.5). Flow cytometry was not feasible for long fibers due to the similarity in lengths of the long fibers and the core diameter of the flow cytometer fluidics components. However, quantification of long fiber-cell interactions at 24 hours post-incubation by optical observation at 40X magnification revealed a similar independence of internalization with increased long fiber dose (Figure 5.6).

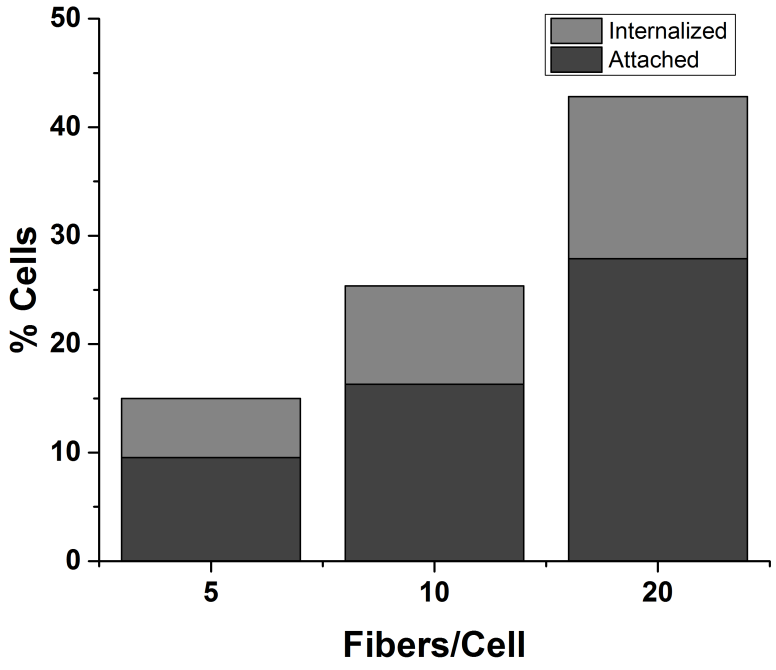

Figure 5-5 Fiber-cell interactions with increasing short fiber dosage. Fiber-cell interactions quantified by flow cytometry reveal a dose-dependent increase in all interactions for short fibers. The relative percentage of cells with internalized interactions compared to total interactions was relatively unchanged for all fiber doses, with 36.4%, 35.7%, and 34.9% for short fiber doses 5, 10, and 20 respectively. A total of 10,000 cells were counted including cells with no associated fibers.

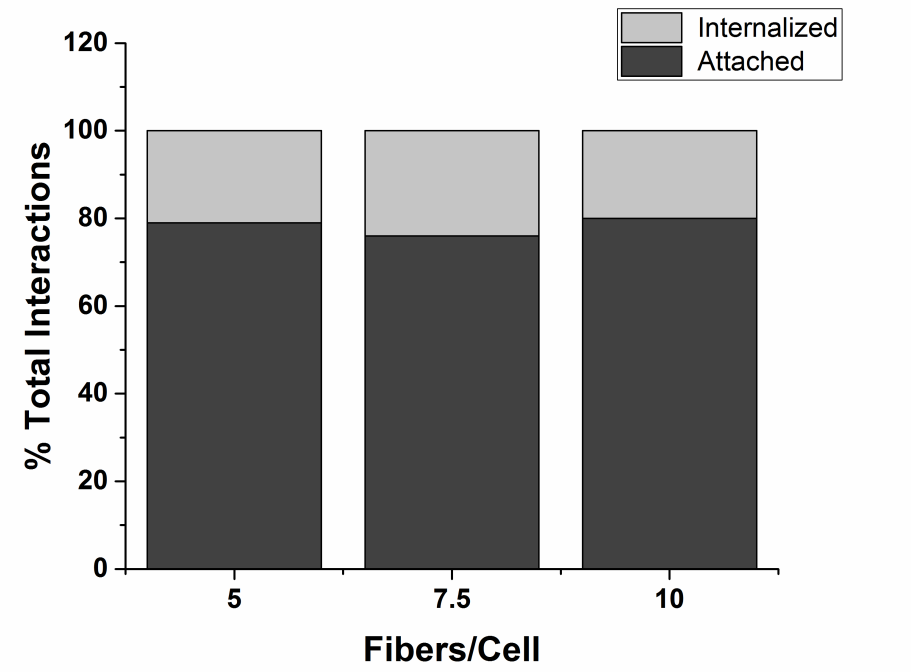

Figure 5-6 Fiber-cell interactions with increasing long fiber dosage. Fiber-cell interactions were quantified by optical observation (40X magnification) at 24 hours post-incubation. Internalized interactions compared to total interactions were relatively unchanged for all fiber doses, with 21%, 24%, and 20% for long fiber doses 5, 7.5, and 10 respectively. A total of 700 fiber/cell were counted

5.4.3 Fiber Cytotoxicity

Macrophages were exposed to short and long fibers for 24 hours, and released cytosolic lactate dehydrogenase (LDH) was measured from culture supernatants as a measure of cytotoxicity. The fiber-exposed macrophages exhibited no detectable LDH cytotoxicity, i.e. the normalized optical absorption fell below the limit of detection range (LOD = 12.5 +/- 3.5%) of the media blanks. Fiber concentrations ranging from 0 – 15 long fibers/cell, and 0 – 150 short fibers/cell exhibited no cytotoxicity (Figure 5.7).

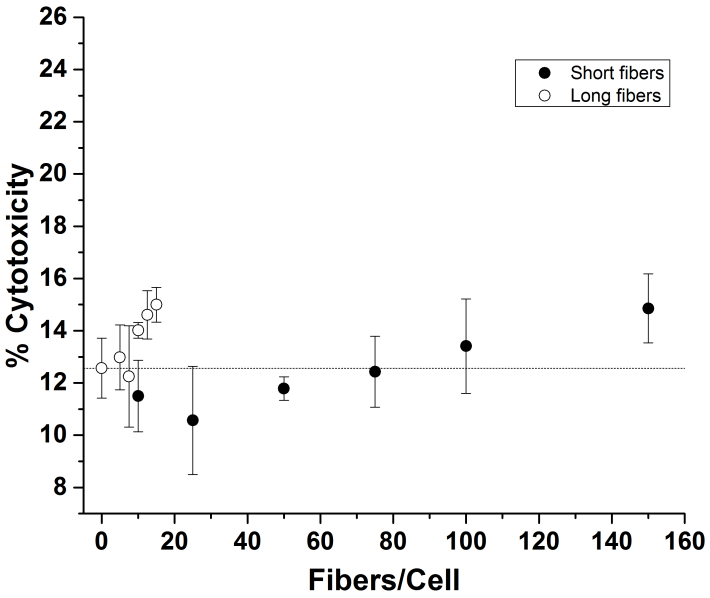

Figure 5-7 Cytotoxicity of macrophages exposed to short and long fibers. The percentage cytotoxicity was measured as the quantity of LDH released from fiber-damaged cells relative to a lysed cell control. Normal cell turnover is shown as 0 fibers /cell and by dashed line (---). On average fiber cytotoxicity was not significant for both short and long fiber populations as compared to the media blank with the exception of the maximum long fiber dose, 15 long fibers/cell. *p<0.05

5.4.4 Fiber induced ROS activity

Cell permeating fluorescent probes such as DCDHF has been used to measure intracellular ROS activity in fiber-stimulated macrophages [143,144]. DCDHF is used to measure the cumulative ROS [145] response after 24 hrs of fiber stimulation to macrophages. Activity of the DCDHF probe was confirmed by LPS stimulation of macrophages (Figure 5.8)**.** Cumulative intracellular reactive oxygen species (ROS) production in response to either long or short fibers is weak. Individual experiments all exhibited ROS signals below the LOD. Attempts to pool the data, using, as a standard,

the ROS signal generated from cells stimulated by LPS (at 1 μg/mL) resulted in low R^2 values indicative of minimal statistical correlation due to this standard signal variance. The pooled data suggest: i) ROS production in response to the glass fibers is detectable, and ii) increased ROS production following exposure to long (vs. short) fibers. However, the ROS signals are all weak, and the above suggestions were not statistically significant (Figure 5.9). Detailed statistical analysis of the ROS measurements were completed by Dr. Turkevich (NIOSH)

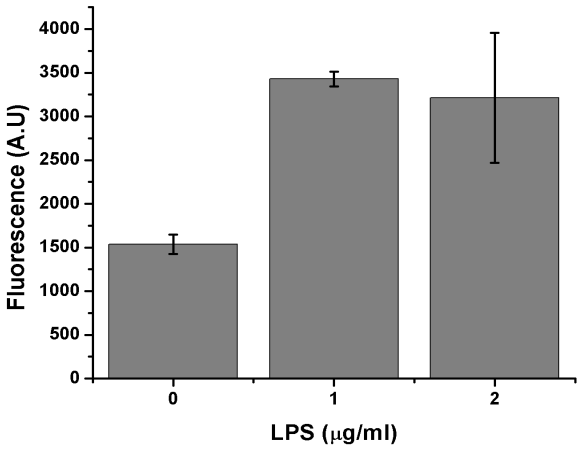

Figure 5-8 ROS production by macrophages stimulated with lipopolysaccharide (LPS). Lipopolysaccharide (LPS), used as a positive control, showed pronounced increase in ROS production after 24-hour stimulation in comparison to the media-treated control cells

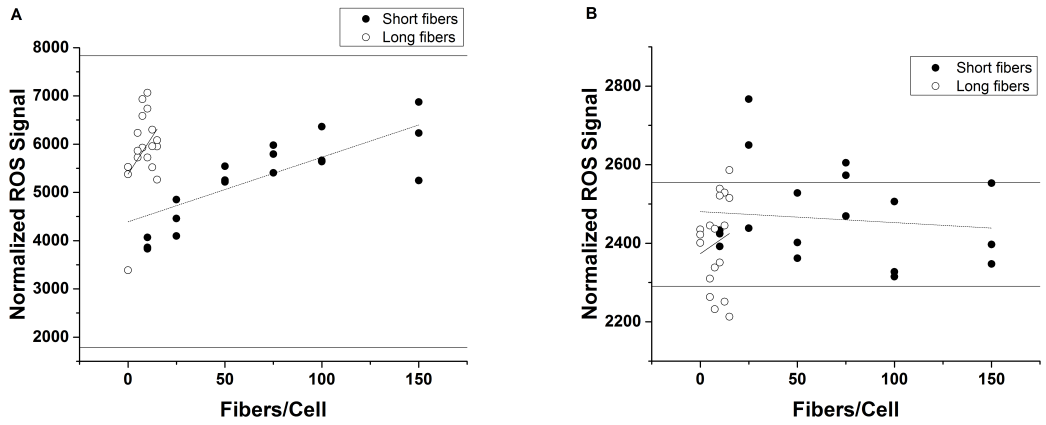

Figure 5-9 ROS production by macrophages stimulated with fibers. Low levels of ROS were observed for long and short fiber stimulated macrophages. ROS experiments were repeated seven times; Graphs (A) & (B) are representative of the variations in ROS observed.

5.4.5 Fiber induced inflammatory molecule production

Four inflammatory-related molecules were measured by ELISA following 24 hours of exposure to fibers. TNF-α cytokine secretion exhibited a linear dose-response on a per fiber basis (Figure 5.10). The signal is strong (much larger than the LOD = 16 pg/mL and LOQ = 44 pg/mL). Long fibers produced greater inflammatory biomolecule secretion than short fibers. The ratio of the TNF-α dose response slopes of long to short fibers was $m_L/m_S = 11.1$, with a 95% confidence interval of $9.1 < m_L/m_S < 13.3$.

Cytokine IL-1α was secreted in very low quantities, but above the limit of detection (LOD = 1.4 pg/mL, LOQ =6.5 pg/mL). Again, both long and short fibers exhibited linear dose responses (Figure 5.11). The ratio of long and short fibers slopes of the IL-1α dose-response curves $m_L/m_S = 11.3$, with a 95% confidence interval of $8.1 < m_L/m_S < 15.7$.

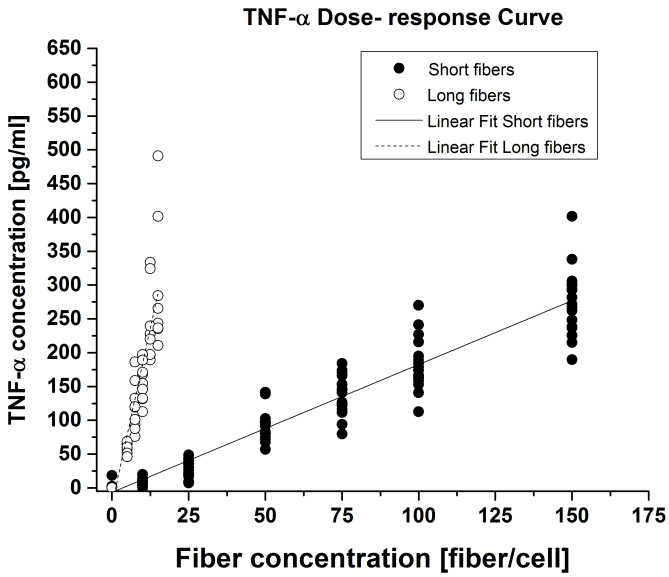

Figure 5-10 TNF-α dose-response curves. TNF-α secretion showed a linear dose response for short and long glass fibers. Data shown was collected for three (3) independent experiments.

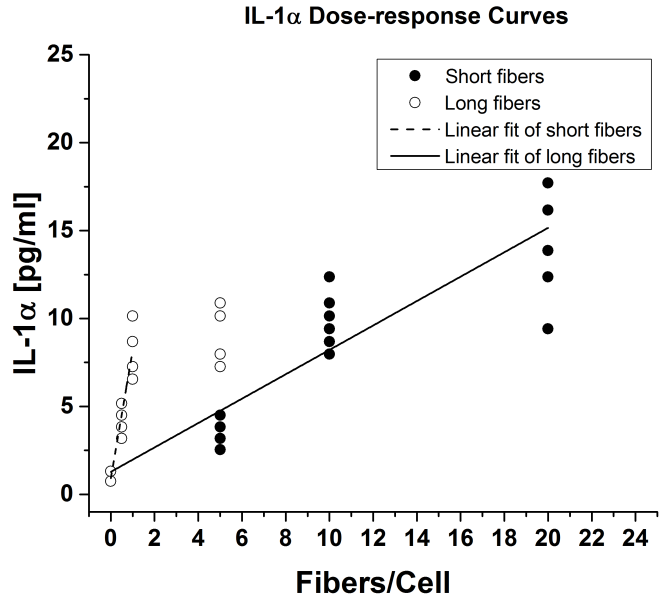

Figure 5-11 IL-1α dose-response curves. IL-1α secretion showed a linear dose response for short and long fibers. Data shown was collected from three (3) independent experiments.

Cyclooxygenase-2 (COX-2) production by fiber-treated macrophages depended inversely on fiber dose (Figure 5.12). The variation of the fiber-stimulated COX-2 production is complicated by the fact that it depends both directly on the stimulating fibers but also indirectly on the cytokine TNF-α, whose production is also stimulated by the fibers [146]. We noted that COX-2 production varies inversely with TNF-α expression (Figure 5.13).

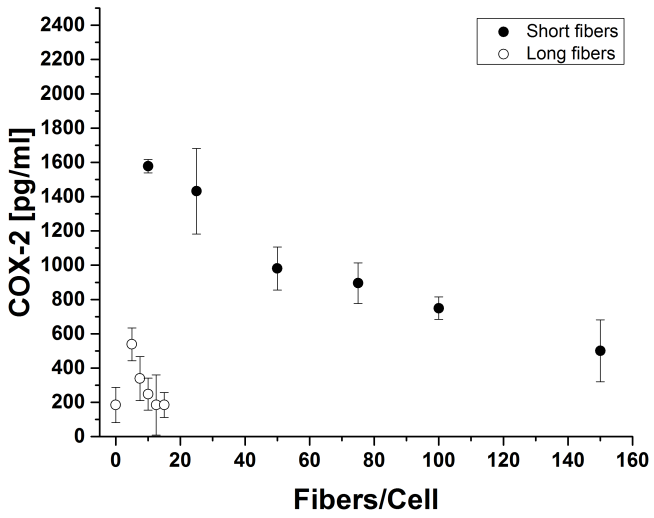

Figure 5-12 COX-2 Enzyme Production. COX-2 production decreased with increasing fiber dose -short fiber stimulation resulted in significantly high expression of COX-2 while long fibers were generally comparable to no fiber stimulation.

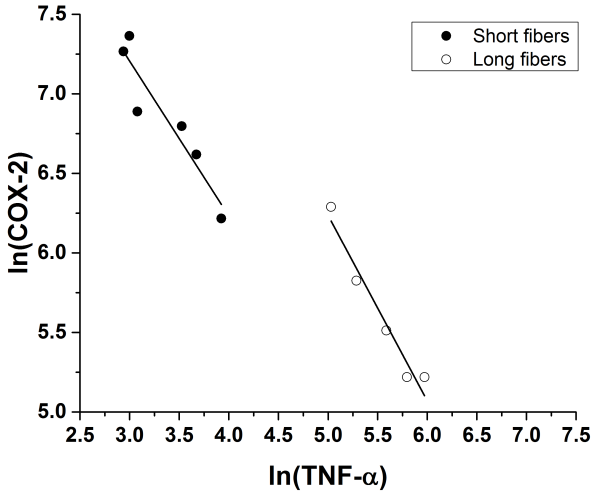

Figure 5-13 COX-2 varies inversely with TNF-α. COX-2 production decreased with respect to fiber length and dosage. COX-2 production varied inversely TNF-α secretion. COX-2 molecule is known to modulate (down-regulate) TNF-α secretion via an NF-kB dependent pathway

Prostaglandin E2 (PGE_2) is a secreted downstream metabolite of the COX enzymatic pathway. PGE_2 secretion was greater for long fibers than short fibers (Figure 5.14). The measured signal from PGE_2 secretion was low, but there was a weak observed linear dose-response for long fibers. PGE_2 production for short fibers was neither statistically significant, i.e. most signals were below the limit of detection (LOD = 55 pg/mL), nor dose-dependent.

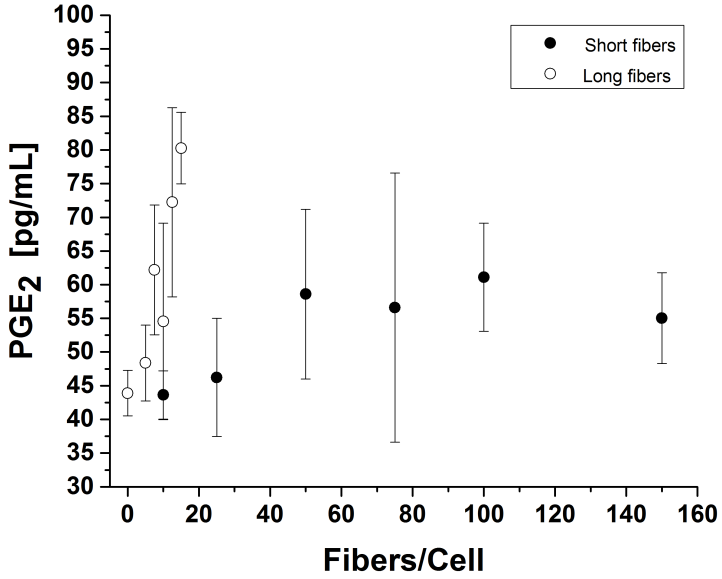

Figure 5-14 Prostaglandin E2, PGE_2, production 24 hours post-incubation. Short fiber response was independent of fiber concentration. Long fibers showed weak dose dependence in comparison to 0 fibers/cell control.

5.5 Discussion

This work uses model glass fibers with measured length distributions and model alveolar macrophages to assess fiber length effects on phagocytosis and associated inflammatory biomolecule production, and to develop the quantitative model described below. The use of glass fibers eliminates contributions of surface chemistry and diameter from those of fiber length. Macrophages are highly heterogeneous cells, and immortalized mouse MH-S alveolar macrophages were chosen as model macrophages because of their increased homogeneity in response to particles of various shapes and sizes [147,148]. Although cytokine response varies across macrophage source, macrophage dose-response is investigated here, and analysis of the change in response is used to build our models.

While cytotoxicity by glass fibers is less pronounced for immortalized cell lines [130] than for primary cell line [121,129], the trends of cytokine response for short and long fibers are the same. Moreover, MH-S macrophages have been shown to function similarly to primary cells for phagocytic interactions and IL-1α cytokine response [149,150].

Stanton performed an exhaustive study across various asbestos types and hypothesized that asbestos fiber dimension and durability, rather than other physicochemical properties, were responsible for fiber-related biological effects *in vivo* [124]. The latency of asbestos-associated pulmonary diseases, as well as the established link between chronic inflammation and cancer [134,135], supports this theory of chronic inflammation resulting from biopersistence as the prevailing cause of disease pathology [120,151–154]. *In vivo* and *in vitro* studies examining the role of fiber length on biopersistence also support this theory. Goodglick et al. showed that both short and long asbestos fibers were cytotoxic *in vitro*, while short fibers were cytotoxic when clearance was prevented *in vivo*[122]. In threshold length studies using silver nanowires Schinwald and colleagues identified *in vivo* threshold lengths of L >4 μm, and 11-14 μm for fiber-induced pleura [123] and pulmonary [155] inflammation respectively. McDonald and colleagues described long fibers (>10 μm) as having the greater pathogenic risk than short fibers (<6 μm) *in vivo* [156]. However, direct comparison among different forms of asbestos remains challenging due to fiber heterogeneity. Comparative length dependent studies, using actual asbestos fibers, have neither been able to characterize fibers within narrow length-classified size ranges, nor separate other confounding fiber parameters such as diameter, chemistry, and surface properties. Indeed, recent studies of asbestos-like high aspect ratio nanomaterials, of which carbon nanotubes are a subset, have shown that these fibers elicit an inflammatory

response due also to surface chemistry-related reactivity and thus are unable to isolate length-based contributions from the biological effects. This highlighted the need for model materials in which pathogenic parameters can be isolated and accurately characterized in order to determine single-parameter contributions to disease endpoints. To this end, *in vitro* studies using glass fibers identified length dependence to the inflammatory response and speculated that increased inflammatory response was due to frustrated phagocytosis of longer fibers. Blake et al. observed a length-dependent cytotoxicity and production of reactive oxygen species after exposure of alveolar macrophages to glass fibers of varied lengths [129]. Ye et al. showed that long fibers (17 μm) were significantly more potent than short fibers (7 μm) in inducing inflammatory NF-kB activation and TNF-α production [130]. Zeidler-Erdely et al. also found that glass fiber > 17 microns were cytotoxic to human primary macrophages [121]. Here we are able to quantify phagocytic interactions and corresponding molecular responses from accurately characterized glass fibers to develop a model that can be used to evaluate the isolated contributions of fiber length to macrophage interactions.

Real-time imaging of interactions between macrophages and fibers revealed internalization, attachment and frustrated phagocytosis outcomes within short and long samples, suggesting weighted contributions of these processes to the overall inflammatory response. We saw that the fraction of internalized long fibers was less than that of short fibers, with long fibers undergoing frustrated phagocytosis due to the inability of the cell to effectively phagocytize fibers. No spearing or damage to the cell membrane was observed. Since, there is ample microscopy evidence for such processes in the literature [120,125], they are either rare, dependent on macrophage type, fiber diameter

and type [157] or occurs on time-scales longer than the 24 hours of our time-lapse experiments. Our observation of macrophage biochemical response to fibers on the short timescale implicates a mechanism other than spearing responsible for increased inflammatory response. Comparison of the average contact surface areas, which scales with fiber length at constant diameter, of long and short internalized fibers, revealed no relationship between quantities of fibers internalized and their average fiber lengths. Thus, internalization does not scale solely with average fiber length, suggesting that other more complex length models are possible. The quantity of internalized short fibers was limited only by fiber concentration, as flow cytometry data showed increased internalization with increased short fiber concentration.

Similar to the cytotoxic findings of Ye et al. with immortalized peritoneal macrophages [130], we found no relationship between fiber length and cytotoxicity. Neither increases in attachment nor internalization had adverse cytotoxic effects. Likewise, cumulative intracellular ROS production by fiber-stimulated macrophages is weak, with, perhaps, an enhancement in ROS production by macrophages stimulated by the long fibers (Supplementary Figure S7). Reactive oxygen species (ROS) are a complex array of highly reactive molecules including H2O2, HOCl, *OH, *O, and superoxide anion compounds. In phagocytes oxidative stress responses at the plasma membrane in response to extracellular pathogenic material [158], and metal ions [116,159] can lead to the generation of extracellular ROS compounds. Generation of ROS by NADPH oxidase also occurs in intracellular compartments such as phagosomal membranes and mitochondria.

In fiber induced diseases ROS plays a pivotal role through fiber-mediated respiratory bursts [160], and frustrated phagocytosis [161]. ROS also plays a role both in cell signaling [162],

activation of cytokine transcription [163], and oxidative stress-mediated cytotoxicity [164]. Increasing levels of intracellular ROS is indicative of cell toxicity [165]. The low intracellular ROS produced by glass fiber stimulation is expected, given the observed lack of cytotoxicity. The low level of ROS produced did not permit significant length-based conclusion, as demonstrated by Brown et al in the study of morphological dependence on phagocytosis of carbon nanotubes [166].

Cytokines TNF-α and IL-1α are secreted in response to inflammatory stimuli. TNF-α has been identified as a critical mediator of fiber-related pathogenicity [130], while pro-inflammatory cytokine IL-1α works in concert with TNF-α and is induced following NF-κB activation [167]. IL-1α secretion has also been reported upon exposure to carbon nanotubes[168,169]. Additionally, IL-1α, along with IL-1β, is indicative of inflammasome activation [170,171]. Studies have shown that the inflammasome is activated upon stimulation by asbestos fibers, carbon nanotubes, and nanoparticles [161,172,173] with reports of dose-dependent secretion of IL-1α [172,174]. Similar to Palomaki and colleagues, glass-fiber stimulation of IL-1α secretion was both dose- and length-dependent[172].

NF-κB has been shown to a have a length-dependent activation by glass fibers [130]. Comparison of the slopes of the dose-response curves for TNF-α and IL-1α showed a greater response to long fibers than to short fibers (Figures 5, 6). TNF-α cytokine secretion did not scale with the average fiber length. We would expect that the ratio of the slopes of short and long cytokine response curves to be the same as the ratio of the short and long average fiber lengths (7 μm /39.3 μm) if cytokine secretion scaled only with fiber length. Additionally, short fibers produced a weaker inflammatory response

per fiber. By extension, complete phagocytosis of fibers has minimal contribution to the inflammatory response. This agrees with contributions of 'frustrated' phagocytic interaction or incomplete internalization of longer fibers to the inflammatory condition [175].

We assessed the ability of the fibers to stimulate pathogenic markers, cycolooxygenase-2 (COX-2) and its downstream metabolite, prostaglandin E2 (PGE_2). COX-2 is known to modulate carcinogenesis. It is induced by oxidative stress and inflammatory cytokine secretion, which are key mechanisms of asbestos fiber responses in cells [176]. Fiber-treated macrophages demonstrated an inverse relationship between TNF-α and COX-2 at 24 hours post-incubation (Supplementary Figure S6). Literature supports that this modulatory action may be NF-κB dependent. Not only is NF-κB known to up-regulate COX-2, but COX-2 activity in turn affects NF-κB [177,178]. Past studies of inflammatory regulation reveal a temporally destabilizing effect of TNF-α on COX-2 mRNA [146]. Our COX-2 results supports this proposed feedback action of COX-2, since at short time scales production of PGE_2 is weak but shows concomitant increases with TNF-α.

We have attempted to rationalize the cytokine data, which demonstrates the increased relative potency of long over short fibers with three simple models— that may be treated as a phenomenological parameterization of the data. These models were fitted only to TNF- α and IL-1 α, since they are directly stimulated by the fibers; by contrast, COX-2 and PGE_2 depend both directly on the stimulating fiber and also indirectly, through the cytokines generated by the macrophages responding to fibers. The two fiber populations differed only in their distribution of lengths, not diameters or chemistry. Thus the ratio of

the slopes of the dose-response curves can only depend on some potency function, $p(L)$, averaged over the length distribution: $< p(L) >$.

In the first model, a simple length cut-off, L_c, is posited so that fibers shorter than L_c elicit no cytokine response, and that all fibers longer than L_c contribute equally to the cytokine response; the potency function $p(L)$ is given by:

$$p(L) = \begin{cases} 0, & L < L_c \\ p_0, & L > L_c \end{cases} \qquad (2)$$

Using the fitted parameters for short and long fiber distributions, we obtain L_c = 27.0 μm, with a 95% confidence interval 22.9 μm < L_c < 31.4 μm for TNF- α, and L_c = 27.4 μm, with a 95% confidence interval 20.8 μm < L_c < 36.0 μm from the IL-1α response. It is remarkable that these two cytokines, TNF-α and IL-1α, yield similar relative potencies of the long and short fibers. Furthermore, the cut-off length is quite reasonable when compared to the size of macrophages. Typical rodent alveolar macrophages are ~13 μm in suspension [179]. However, plated macrophages spread to larger diameters, 20.7 +/- 8.8 μm in this work, and are the appropriate comparison since all experiments were performed on plated cells.

In the second model, long fibers are modeled as being more potent than short through a power law:

$$p(L) \sim L^{\alpha} \qquad (5)$$

There is no cut-off length in this model. Using the fitted parameters for short and long fiber distributions we obtain $\alpha = 1.75$, with a 95% confidence interval $1.56 < \alpha <$

1.93 for TNF- α, and $\alpha = 1.76$, with a 95% confidence interval $1.46 < \alpha < 2.11$ from the IL-1α response. Most physical quantities relevant to fiber -cell interactions, such as average fiber length, average volume, mass, average surface area, all scale as <L> (i.e. $\alpha = 1$) and thus $\alpha > 1$ is unreasonable. Our results thus argue for either a stronger length variation of potency (stronger than a power law, or for an additional reduced potency of the short fibers e.g. through a length cut-off, L_c).

In a third two-parameter model, fibers longer than a cut-off, L_c, elicit a response, scaling as a power of the length, that is, longer non-internalized fibers, are weighted more; the appropriate potency function is

$$p(L) = \begin{cases} 0, & L < L_c \\ p_0 L^{\alpha}, & L > L_c \end{cases} \qquad (7)$$

If we force $\alpha = 1$, we obtain $L_c = 12.1$ μm, with a 95% confidence interval 7.7 μm < L_c < 16.3 μm for TNF- α, and $L_c = 12.5$ μm, with a 95% confidence interval 4.9 μm < L_c < 20.6 μm from the IL-1α response. Again, the cut-off lengths determined by these independent cytokine measurements are very similar.

With a cut-off, if there is no additional length dependence of the potency ($\alpha = 0$), we obtain $L_c \sim 27$ μm, comparable to the macrophage size. If, with a cut-off, the potency of the non-phagocytosed fibers depends on the standard physical parameters ($\alpha = 1$), we obtain $L_c \sim 12$ μm, shorter than the macrophage size, but not unreasonable. Frustrated phagocytosis was observed by time-lapse microscopy for length, L > 16μm, which is consistent with the cut-offs obtained from the first and third models; we have no

independent criteria to prefer the first model over the third model. We note that, $\alpha = 1.75$ from a simple power law potency (second model) seems unreasonable.

Schinwald and colleagues reported a critical length range of 5 μm for onset of frustrated phagocytosis in a primary alveolar *in vitro* migration assay [155]. However, considering the contribution of fiber length distribution, and *in vitro* assay type we cautiously report that the authors' threshold length is within the range of our third model predictions. Schinwald et al proposes that mechanical obstruction of long bulky fibers may have led to decreasing mobility with increasing fiber length. We have also observed that multiple cells will simultaneously attempt to engulf the same longer fiber which may lead to low cell mobility, as seen by Schinwald et al. Given our frequency of fiber length, with 40% of short glass fibers and 95% of our long fibers being greater than the silver nanowire lengths examined a migration assay would not have been feasible for direct comparison of threshold lengths.

Our models suggest that fiber-cell interaction differs above and below a critical fiber length; fibers with lengths $L < L_c$ contribute minimally to inflammatory biomolecule production, while the majority of biomolecule production is due to frustrated phagocytosis of fibers of length $L>L_c$. L_c should be viewed as a statistical parameter, as variations in macrophage cell and fiber-cell orientation will influence the outcome of individual fiber-cell interactions. The output of the length-based models may change with fiber and cell type. The degree, to which this occurs, along with *in vivo* validation of *in vitro* findings, will be the focus of our future work. By establishing glass fiber length-based models as a control, the question of the extent to which length potentiates the

adverse effects of other physicochemical parameters of asbestos fibers can be answered. Importantly, independent of the detailed modeling, these studies have shown that, even for very short induction times (~ 24 hours), there is significant length dependence to the response of macrophage cells phagocytic interactions with fibers.

5.6 Conclusion

Our results show that the single physical parameter of length plays an important role in fiber-induced macrophage inflammatory responses. Pro-inflammatory cytokines, TNF-α and IL-1α, were shown to increase in both a dose and length dependent manner. Short fibers were more readily internalized and played a minor role in inflammatory biomolecule production compared to long fibers on a per-fiber basis. The MH-S cell line showed no dose toxicity allowing us to reproducibly evaluate dose-response up to two orders of magnitude. Importantly, for our stimulating material, characterization revealed no correlation between fiber diameter distribution and length distribution, so we are able to isolate the effect of fiber length on the macrophage response. This distinguishes our study from previous work on length dependence of frustrated phagocytosis and inflammatory responses. Here we show a universal dose-response approach to determining critical length and present two possible models that describes phagocytic interactions: a critical length based model in which the potency of longer fibers are equally weighted, and a two-parameter power law and potency model in which the weighting is skewed toward longer fibers. Each model produces reasonable critical lengths for frustrated phagocytosis: 27 μm and 12 μm.

5.7 Future Work

These fiber-cell interactions differed above and below modeled critical fiber lengths suggesting that length should be treated as a statistical parameter where variations in fiber type and cell type may influence the output of the length-based models. Future studies will seek to determine the extent to which fiber length potentiates the effects of other physicochemical parameters such as surface composition by comparing length-based results of various asbestos types to our single-parameter glass fiber model. This will involve the identification of asbestos or mineral fiber types that can be reproducibly length-separated without adversely affecting other physicochemical properties. Fibers can be selected across varied groups and/or mineral series: actinolite, anthophyllite, chrysotile, crocidolite, tremolite, and wrightwood actinolite. Interactions of asbestos fibers both 'unseparated or separated' with mouse alveolar macrophage cells can provide initial screening of fiber-cell interactions that lead to frustrated phagocytosis and which contribute to cell death in short times (< 24hours). Observations of fiber-cell interactions with primary alveolar macrophage cells that are more physiologically relevant can be investigated. Cytokine responses (TNF-α, IL-1ß, IL-1α) as well as intra- and extra-cellular ROS generation, and cell metabolism assays can be performed across asbestos groups.

APPENDIX I.

PROTEIN AND PEPTIDE SEQUENCES

Sequences

ELP DNA Sequence

TGTGGGGTGCCGGGTGTGGGCGTTCCGGGCGTGGGTGTACCGGGCTTCGGTG
TCCCGGGCGTAGGTGTTCCGGGTGTCGGGGTGCCGGGTGTGGGCGTTCCGGG
CGTGGGTGTACCGGGCTTCGGTGTCCCGGGCGTAGGTGTTCCGGGTGTCGGG
GTGCCGGGTGTGGGCGTTCCGGGCGTGGGTGTACCGGGCTTCGGTGTCCCGG
GCGTAGGTGTTCCGGGTGTCGGGGTGCCGGGTGTGGGCGTTCCGGGCGTGGG
TGTACCGGGCTTCGGTGTCCCGGGCGTAGGTGTTCCGGGTGTCGGGGTGCCG
GGTGTGGGCGTTCCGGGCGTGGGTGTACCGGGCTTCGGTGTCCCGGGCGTAG
GTGTTCCGGGTGTCGGGA

ELP Amino Acid Sequence

MKGSCGVPGVGVPGVGVPGFGVPGVGVPGVGVPGVGVPGVGVPGFGVPGVGV
PGVGVPGVGVPGVGVPGFGVPGVGVPGVGVPGVGVPGVGVPGFGVPGVGVPG
VGVPGVGVPGVGVPGFGVPGVGVPGVG

ELP-SH3 DNA Sequence

GATCCTGTGGGGTGCCGGGTGTGGGCGTTCCGGGCGTGGGTGTACCGGGCTT
CGGTGTCCCGGGCGTAGGTGTTCCGGGTGTCGGGGTGCCGGGTGTGGGCGTT
CCGGGCGTGGGTGTACCGGGCTTCGGTGTCCCGGGCGTAGGTGTTCCGGGTG
TCGGGGTGCCGGGTGTGGGCGTTCCGGGCGTGGGTGTACCGGGCTTCGGTGT
CCCGGGCGTAGGTGTTCCGGGTGTCGGGGTGCCGGGTGTGGGCGTTCCGGGC
GTGGGTGTACCGGGCTTCGGTGTCCCGGGCGTAGGTGTTCCGGGTGTCGGGG
TGCCGGGTGTGGGCGTTCCGGGCGTGGGTGTACCGGGCTTCGGTGTCCCGGG
CGTAGGTGTTCCGGGTGTCGGGAAGCTTCGCGATTGGGGTGGTAGCCCTAGG
GGAGTGCGTTGGGCCAGGGCACTGTATGACTTTGAGGCTCTGGAAGAGGACG
AGCTGGGATTCCGAAGCGGAGAAGTGGTTGAAGTCCTGGACAGCTCCAACCC
ATCTTGGTGGACCGGCCGTCTGCACAACAAACTGGGTCTCTTCCCTGCCAACT
ATGTGGCCCCCATGATGCGAAGATCTCATCACCATCACCATCAC

ELP-SH3 Amino Acid Sequence

MKGSCGVPGVGVPGVGVPGFGVPGVGVPGVGVPGVGVPGVGVPGFGVPGVGV
PGVGVPGVGVPGVGVPGFGVPGVGVPGVGVPGVGVPGVGVPGFGVPGVGVPG
VGVPGVGVPGVGVPGFGVPGVGVPGVGKLRDWGGSPRGVRWARALYDFEALE
EDELGFRSGEVVEVLDSSNPSWWTGRLHNKLGLFPANYVAPMMRRSHHHHHH

GST-GLP1-SBP2 Amino Acid Sequence

MSPILGYWKIKGLVQPTRLLLEYLEEKYEEHLYERDEGDKWRNKKFELGLEFPN
LPYYIDGDVKLTQSMAIIRYIADKHNMLGGCPKERAEISMLEGAVLDIRYGVSRI
AYSKDFETLKVDFLSKLPEMLKMFEDRLCHKTYLNGDHVTHPDFMLYDALD
VVLYMDPMCLDAFPKLVCFKKRIEAIPQIDKYLKSSKYIAWPLQGWQATFGGGD
HPPKSDLVPRGSHGEGTFTSDVSSYLEEQAAKEFIAWLVKGAGKSPAPSIDRSTK
PPL

GLP-1-SBP2 DNA Sequence

GCAGCGCACGGTGAAGGCACCTTTACGAGCGATGTGAGCTCGTATCTGGAAG
AGCAGGCAGCGAAAGAATTTATCGCGTGGCTGGTGAAAGGTGCGGGCAAGC
TTCCTATGAAAAGCAAAAGCCCGGCGCCGAGCATTGACCGTAGCACCAAACC
GCCACTG

Table 1: Comparison of Amino Acid Sequences of GLP-1-SBPs

Agonist	Amino Acid Sequence
GLP-1	^{7}HAEGTFTSDVSSYLEGQAAKEFIAWLVKGRG^{37}
Exendin-4	HGEGTFTSDLSKQMEEEAVRLFIEWLKNGGPSSGAPPPS
GLP-1-SBP2	HG^{8}EGTFTSDVSSYLEE^{22}QAAKEFIAWLVKGA^{36}GKSPAPSIDRSTKPPL

GLP-1-SBP13 | HG[8]EGTFTSDVSSYLEE[22]QAAKEFIAWLVKGA[36]GKSPAPSIARSTKPPL

GLP-1-SBP24 | HG[8]EGTFTSDVSSYLEE[22]QAAKEFIAWLVKGA[36]GKSSNTPPPRPPKPSH

Potential Scramble fusion peptide based on the scrambling of binding sequence R-xx-K

GLP-1-Scramble | HG[8]EGTFTSDVSSYLEE[22]QAAKEFIAWLVKGA[36]GKSPAPSISAKTPPRL

APPENDIX II.

MATHEMATICAL MODEL

Pdex_release.m

```
function pdex_release
%PDEXTP  Mathematical Model for GLP-1-SBP Release
%
%   The PDEs & ODEs are
%      The Reaction-Diffusion Eqn
%      D(u1)/Dt = Di*D^2(u1)/Dx^2 + F
%
%   ODEs
%      D(u2)/Dt = F
%      D(u3)/Dt = -F
%
%      where;
%      F(y) = kr*u(3)-kf*u(1)*u(2)
%
%   In the form expected by PDEPE solver,
% cn(x; t; u; ux)unt = x^-m d/dx (x^m bn(x; t; u; ux))+sn(x; t; u; ux)
%   the equations are:
%   |1|         |u1|      | Di*D(u1)/Dx |        | F |
%   |1| .*  D_  |u2| = D_ | 0.0*D(u2)/Dx |  +    | F |
%   |1|     Dt  |u3|   Dx | 0.0*D(u3)/Dx |       |-F |
%
%   ---         ---       ------------------    ---------------
%    c           u          f(x,t,u,Du/Dx)       s(x,t,u,Du/Dx)
%
%   The initial condition is u1(x,0) = u1eq , u2(x,0) = u2eq and
u3(x,0) = u3eq for 0 <= x <= 1.
%
%   The left boundary condition is D(u1)/Dx = 0, u2(0,t) = 0,
u3(0,t)=0.  The
%   condition on the partial derivative of u1 has to be written in
terms of the flux.  In the form expected by PDEPE, the left bc is
%
%      |0 |       |1|     | 0.00905*D(u1)/Dx |        |0|
%      |u2|   +   |1| .*  | 0.0*D(u2)/Dx |      =     |0|
%      |u3|       |1|     | 0.0*D(u3)/Dx |            |0|
%
%      ---        ---     ------------------          ---
%    p(0,t,u)    q(0,t)     f(0,t,u,Du/Dx)             0
%
%   The right boundary condition is u1(1,t) = 0, D(u1)/Dx = J(u1):
%
%      |u1|        |0|     | 0.00905*D(u1)/Dx |         |0|
%      |u2|   +    |1| .*  | 0.0*D(u2)/Dx   |       =   |0|
%      |u3|        |1|     | 0.0*D(u3)/Dx   |           |0|
%
%      -------    -----    ------------------          ---
%      p(1,t,u)   q(1,t)     f(1,t,u,Du/Dx)             0
```

```
%
% Subfunctions
%PDEX_releasePDE, PDEX_releaseIC, & PDEX_releaseBC define the system
%


m = 2; %spherical
x = [0 0.005 0.01 0.05 0.1 0.2 0.3 0.4 0.5 0.6 0.7 0.8 0.9 0.95 0.99
0.995 1]; %mesh for a model 1 micron sphere
t = [0 0.005 0.01 0.05 0.1 0.5 1 1.5 2]; %time

sol = pdepe(m,@pdex_releasepde,@pdex_releaseic,@pdex_releasebc,x,t);
u1 = sol(:,:,1);%u(1)SBP
u2 = sol(:,:,2);%u(2)SH3
u3 = sol(:,:,3);%u(3)SBP-SH3

 figure;
plot(t,u1);
xlabel('Time');
ylabel('Concentration');


% --------------------------------------------------------------------


function [c,f,s] = pdex_releasepde(x,t,u,DuDx)
c = [1; 1;1];
f = [Di;0;0] .* DuDx;      % Input Di, diffusivity   [=]micron^2/day
F = kr*u(3)-kf*u(1)*u(2);  % Values for koff [=]1/day & kon [=]1/M*day
s = [F; F;-F];

% --------------------------------------------------------------------

function u0 = pdex_releaseic(x)
u0 = [SBPeq; SH3eq;SBP-SH3eq];   % Input([=]Molar)equilibrium
quantities

% --------------------------------------------------------------------

function [pl,ql,pr,qr] = pdex_releasebc(xl,ul,xr,ur,t)
pl = [0; ul(2);ul(3)];
ql = [1; 1;1];
pr = [ur(1); ur(2);ur(3)];
qr = [1; 0;1];
```

nonlinear.m

```
%Coupled non-linear algebraic equations for equilibrium values
% kf*CSBPeq*CSH3eq = kr*CSBP-SH3eq (5)
% CSBPtot = CSBPeq + CSBP-SH3eq    (6)
% CSH3tot = CSH3eq + CSBP-SH3eq    (7)
% requires user input x0 = [...] initial guesses for x(1),x(2), and
x(3)
% Equilibrium concentration output used in PDEPE model for solution
% to coupled PDE-ODE system
%
%_____________________________________________________________
function F= nonlinear(x)
SBPtot= 103*10^(-6) %Molar quantity of total SBP incubated
SH3tot= 50*10^(-6) %Molar quantity of total SH3 domains in 1mg/ml
spheres
%x(1)= equilibrium quantity of GLP-1-SBP
%x(2)= equilibrium quantity of SH3
%x(3)= equilibrium quantity of complex
% kf Association constant e.g. SBP2[=] 1/Ms
% kr Dissociation constant e.g. SBP2[=] 1/s
F= kf*x(1)*x(2)-kr*x(3);
SBPtot-x(1)-x(3);
SH3tot-x(2)-x(3)];
end
```

REFERENCES

(1) A BCC Research Biotechnology Report. *Biologic Therapeutic Drugs : Technologies and Global Markets*; 2015.

(2) Fosgerau, K.; Hoffmann, T. Peptide Therapeutics: Current Status and Future Directions. *Drug Discov. Today* **2015**, *20*, 122–128.

(3) Mitragotri, S.; Burke, P. A.; Langer, R. Overcoming the Challenges in Administering Biopharmaceuticals: Formulation and Delivery Strategies. *Nat. Rev. Drug Discov.* **2014**, *13*, 655–672.

(4) Danhier, F.; Ansorena, E.; Silva, J. M.; Coco, R.; Le Breton, A.; Préat, V. PLGA-Based Nanoparticles: An Overview of Biomedical Applications. *J. Control. Release* **2012**, *161*, 505–522.

(5) Kumari, A.; Yadav, S. K.; Yadav, S. C. Biodegradable Polymeric Nanoparticles Based Drug Delivery Systems. *Colloids Surfaces B Biointerfaces* **2010**, *75*, 1–18.

(6) Lin, C. C.; Metters, A. T. Hydrogels in Controlled Release Formulations: Network Design and Mathematical Modeling. *Adv. Drug Deliv. Rev.* **2006**, *58*, 1379–1408.

(7) de Las Heras Alarcon, C.; Pennadam, S.; Alexander, C. Stimuli Responsive Polymers for Biomedical Applications. *Chem. Soc. Rev.* **2005**, *34*, 276–285.

(8) Ulery, B. D.; Nair, L. S.; Laurencin, C. T. Biomedical Applications of Biodegradable Polymers. *J. Polym. Sci. Part B Polym. Phys.* **2011**, *49*, 832–864.

(9) Fu, K.; Klibanov, A. M.; Langer, R. Protein Stability in Controlled-Release Systems. *Nat. Biotechnol.* **2000**, *18*, 24–25.

(10) Lee, K.; Silva, E. A.; Mooney, D. J. Growth Factor Delivery-Based Tissue Engineering: General Approaches and a Review of Recent Developments. *J. R. Soc. Interface* **2011**, *8*, 153–170.

(11) Ramirez, F.; Rifkin, D. B. Cell Signaling Events: A View from the Matrix. *Matrix Biol.* **2003**, *22*, 101–107.

(12) Czyz, J.; Wobus, A. Embryonic Stem Cell Differentiation: The Role of Extracellular Factors. *Differentiation* **2001**, *68*, 167–174.

(13) Schultz, G. S.; Wysocki, A. Interactions between Extracellular Matrix and Growth Factors in Wound Healing. *Wound Repair Regen.* **2009**, *17*, 153–162.

(14) Sakiyama-Elbert, S. E.; Hubbell, J. A. Controlled Release of Nerve Growth Factor from a Heparin-Containing Fibrin-Based Cell Ingrowth Matrix. *J. Control. Release*

2000, *69*, 149–158.

(15) Sakiyama-Elbert, S. E.; Hubbell, J. A. Development of Fibrin Derivatives for Controlled Release of Heparin-Binding Growth Factors. *J. Control. Release* **2000**, *65*, 389–402.

(16) Zisch, A. H.; Schenk, U.; Schense, J. C.; Sakiyama-Elbert, S. E.; Hubbell, J. A. Covalently Conjugated VEGF-Fibrin Matrices for Endothelialization. *J. Control. Release* **2001**, *72*, 101–113.

(17) Kiick, K. L. Peptide- and Protein-Mediated Assembly of Heparinized Hydrogels. *Soft Matter* **2008**, *4*, 29–37.

(18) Wong, C. T. S.; Foo, P.; Seok, J.; Mulyasasmita, W.; Parisi-amon, A.; Heilshorn, S. C. Hydrogels for Cell Encapsulation. *Cell* **2009**, *106*, 22067–22072.

(19) Pakulska, M. M.; Vulic, K.; Shoichet, M. S. Affinity-Based Release of Chondroitinase ABC from a Modified Methylcellulose Hydrogel. *J. Control. Release* **2013**, *171*, 11–16.

(20) Vulic, K.; Shoichet, M. S. Tunable Growth Factor Delivery from Injectable Hydrogels for Tissue Engineering. *J. Am. Chem. Soc.* **2012**, *134*, 882–885.

(21) Martino, M. M.; Briquez, P. S.; Ranga, A.; Lutolf, M. P.; Hubbell, J. a. Heparin-Binding Domain of Fibrin(ogen) Binds Growth Factors and Promotes Tissue Repair When Incorporated within a Synthetic Matrix. *Proc. Natl. Acad. Sci. U. S. A.* **2013**, *110*, 4563–4568.

(22) Belair, D. G.; Khalil, A. S.; Miller, M. J.; Murphy, W. L. Serum-Dependence of Affinity-Mediated VEGF Release from Biomimetic Microspheres. *Biomacromolecules* **2014**, *15*, 2038–2048.

(23) Decher, G. Fuzzy Nanoassemblies: Toward Layered Polymeric Multicomposites. *Science (80-.).* **1997**, *277*, 1232–1237.

(24) Borges, J.; Mano, J. Molecular Interactions Driving the Layer-by-Layer Assembly of Multilayers. *Chem. Rev.* **2014**, *114*, 8883–8942.

(25) Lvov, Y.; Ariga, K.; Ichinose, I.; Kunitake, T. Assembly of Multicomponent Protein Films by Means of Electrostatic Layer-by-Layer Adsorption. *J. Am. Chem. Soc.* **1995**, *117*, 6117–6123.

(26) Caruso, F.; Mohwald, H. Protein Multilayer Formation on Colloids through a Stepwise Self-Assembly Technique Protein Multilayer Formation on Colloids through a Stepwise Self-Assembly Technique. *J. Am. Chem. Soc.* **1999**, 6039–6046.

(27) Ventura, J.; Eron, S. J.; Gonzalez-Toro, D. C.; Raghupathi, K.; Wang, F.; Hardy, J.

A.; Thayumanavan, S. Reactive Self-Assembly of Polymers and Proteins to Reversibly Silence a Killer Protein. *Biomacromolecules* **2015**, *16*, 3161–3171.

(28) Pike, D. B.; Cai, S.; Pomraning, K. R.; Firpo, M. A.; Fisher, R. J.; Shu, X. Z.; Prestwich, G. D.; Peattie, R. A. Heparin-Regulated Release of Growth Factors in Vitro and Angiogenic Response in Vivo to Implanted Hyaluronan Hydrogels Containing VEGF and bFGF. *Biomaterials* **2006**, *27*, 5242–5251.

(29) Soontornworajit, B.; Zhou, J.; Shaw, M. T.; Fan, T.-H.; Wang, Y. Hydrogel Functionalization with DNA Aptamers for Sustained PDGF-BB Release. *Chem. Commun. (Camb).* **2010**, *46*, 1857–1859.

(30) Pakulska, M. M.; Miersch, S.; Shoichet, M. S. Designer Protein Delivery: From Natural to Engineered Affinity-Controlled Release Systems. *Science (80-.).* **2016**, *351*, aac4750-9.

(31) Centers for Disease Control and Prevention. *National Diabetes Statistics Report: Estimates of Diabetes and Its Burden in the United States*; 2014.

(32) Holst, J. J. The Physiology of Glucagon-like Peptide 1. *Physiol. Rev.* **2007**, 1409–1439.

(33) Meier, J. J. GLP-1 Receptor Agonists for Individualized Treatment of Type 2 Diabetes Mellitus. *Nat. Rev. Endocrinol.* **2012**, *8*, 728–742.

(34) Kwak, H. H.; Shim, W. S.; Hwang, S.; Son, M. K.; Kim, Y. J.; Kim, T. H.; Yoon, Z. H.; Youn, H. J.; Lee, G. Il; Kang, S. H.; *et al.* Pharmacokinetics and Efficacy of a Biweekly Dosage Formulation of Exenatide in Zucker Diabetic Fatty (ZDF) Rats. *Pharm. Res.* **2009**, *26*, 2504–2512.

(35) Harkiolaki, M.; Lewitzky, M.; Gilbert, R. J. C.; Jones, E. Y.; Bourette, R. P.; Mouchiroud, G.; Sondermann, H.; Moarefi, I.; Feller, S. M. Structural Basis for SH3 Domain-Mediated High-Affinity Binding between Mona/Gads and SLP-76. *EMBO J.* **2003**, *22*, 2571–2582.

(36) Urry, D. W.; Trapane, T. L.; Prasad, K. U. Phase-Structure Transitions of the Elastin Polypentapeptide- Water System Within the Framework of Composition-Temperature Studies. **1985**, *24*, 2345–2356.

(37) Bourette, R. P.; Arnaud, S.; Myles, G. M.; Blanchet, J. P.; Rohrschneider, L. R.; Mouchiroud, G. Mona, a Novel Hematopoietic-Specific Adaptor Interacting with the Macrophage Colony-Stimulating Factor Receptor, Is Implicated in Monocyte/macrophage Development. *EMBO J.* **1998**, *17*, 7273–7281.

(38) Liu, S. K.; McGlade, C. J. Gads Is a Novel SH2 and SH3 Domain-Containing Adaptor Protein That Binds to Tyrosine-Phosphorylated Shc. *Oncogene* **1998**, *17*, 3073–3082.

(39) Mayer, B. J. SH3 Domains: Complexity in Moderation. *J. Cell Sci.* **2001**, *114*, 1253–1263.

(40) Pawson, T. Protein Modules and Signalling Networks. *Nature*, 1995, *373*, 573–580.

(41) Karatan, E.; Merguerian, M.; Han, Z.; Scholle, M. D.; Koide, S.; Kay, B. K. Molecular Recognition Properties of FN3 Monobodies That Bind the Src SH3 Domain. *Chem. Biol.* **2004**, *11*, 835–844.

(42) Meyer, D. E.; Chilkoti, A. Purification of Recombinant Proteins by Fusion with Thermally-Responsive Polypeptides. *Nat. Biotechnol.* **1999**, *17*, 1112–1115.

(43) Na, K.; Jung, J.; Lee, J.; Hyun, J. Thermoresponsive Pore Structure of Biopolymer Microspheres for a Smart Drug Carrier. *Langmuir* **2010**, *26*, 11165–11169.

(44) Park, W. M.; Champion, J. A. Thermally Triggered Self-Assembly of Folded Proteins into Vesicles. *J. Am. Chem. Soc.* **2014**, *136*, 17906–17909.

(45) Koria, P.; Yagi, H.; Kitagawa, Y.; Megeed, Z.; Nahmias, Y.; Sheridan, R.; Yarmush, M. L. Self-Assembling Elastin-like Peptides Growth Factor Chimeric Nanoparticles for the Treatment of Chronic Wounds. *Proc. Natl. Acad. Sci. U. S. A.* **2011**, *108*, 1034–1039.

(46) Dreher, M. R.; Simnick, A. J.; Fischer, K.; Smith, R. J.; Patel, A.; Schmidt, M.; Chilkoti, A. Temperature Triggered Self-Assembly of Polypeptides into Multivalent Spherical Micelles. *J. Am. Chem. Soc.* **2008**, *130*, 687–694.

(47) Betre, H.; Liu, W.; Zalutsky, M. R.; Chilkoti, A.; Kraus, V. B.; Setton, L. A. A Thermally Responsive Biopolymer for Intra-Articular Drug Delivery. *J. Control. Release* **2006**, *115*, 175–182.

(48) Lim, D. W.; Nettles, D. L.; Setton, L. A.; Chilkoti, A. In Situ Cross-Linking of Elastin-like Polypeptide Block Copolymers for Tissue Repair. *Biomacromolecules* **2008**, *9*, 222–230.

(49) Xu, G.; Stoffers, D. A.; Habener, J. F.; Bonner-Weir, S. Exendin-4 Stimulates Both Beta-Cell Replication and Neogenesis, Resulting in Increased Beta-Cell Mass and Improved Glucose Tolerance in Diabetic Rats. *Diabetes* **1999**, *48*, 2270–2276.

(50) Stoffers, D. A.; Desai, B. M.; DeLeon, D. D.; Simmons, R. A. Neonatal Exendin-4 Prevents the Development of Diabetes in the Intrauterine Growth Retarded Rat. *Diabetes* **2003**, *52*, 734–740.

(51) Zhou, J.; Wang, X.; Pineyro, M. A.; Egan, J. M. Glucagon-like Peptide 1 and Exendin-4 Convert Pancreatic AR42J Cells Into Glucagon- and Insulin-Producing Cells. *Diabetes* **1999**, *48*, 2358–2366.

(52) Baggio, L.; Kieffer, T. J.; Drucker, D. J. Glucagon-like Peptide-1, but Not Glucose-Dependent Insulinotropic Peptide, Regulates Fasting Glycemia Nad Nonenteral Glucose Clearance in Mice. *Endocrinology* **2000**, *141*, 3703–3709.

(53) Anini, Y.; Brubaker, P. L. Muscarinic Receptors Control Glucagon-like Peptide 1 Secretion by Human Endocrine L Cells. *Endocrinology* **2003**, *144*, 3244–3250.

(54) Nauck, M. A.; Heimesaat, M. M.; Behle, K.; Holst, J. J.; Nauck, M. S.; Ritzel, R.; Hüfner, M.; Schmiegel, W. H. Effects of Glucagon-like Peptide 1 on Counterregulatory Hormone Responses, Cognitive Functions, and Insulin Secretion during Hyperinsulinemic, Stepped Hypoglycemic Clamp Experiments in Healthy Volunteers. *J. Clin. Endocrinol. Metab.* **2002**, *87*, 1239–1246.

(55) Flint, A.; Raben, A.; Astrup, A.; Holst, J. J. Glucagon-like Peptide 1 Promotes Satiety and Suppresses Energy Intake in Humans. *J. Clin. Invest.* **1998**, *101*, 515–520.

(56) Goke, R.; Larsen, P. J.; Mikkelsen, J. D.; Sheikh, S. P. Distribution of GLP-1 Binding Sites in the Rat Brain: Evidence That Exendin-4 Is a Ligand of Brain GLP-1 Binding Sites. *Eur. J. Neurosci.* **1995**, *7*, 2294–2300.

(57) Read, N.; French, S.; Cunningham, K. The Role of the Gut in Regulating Food Intake in Man. *Nutr. Rev.* **1994**, *52*, 1–10.

(58) Wettergren, A.; Schjoldager, B.; Mortensen, P. E.; Myhre, J.; Christiansen, J.; Holst, J. J. Truncated GLP-1 (Proglucagon 78-107-Amide) Inhibits Gastric and Pancreatic Functions in Man. *Dig. Dis. Sci.* **1993**, *38*, 665–673.

(59) Verdich, C.; Toubro, S.; Buemann, B.; Lysgård Madsen, J.; Juul Holst, J.; Astrup, A. The Role of Postprandial Releases of Insulin and Incretin Hormones in Meal-Induced Satiety--Effect of Obesity and Weight Reduction. *Int. J. Obes. Relat. Metab. Disord.* **2001**, *25*, 1206–1214.

(60) Rask, E.; Olsson, T.; Soderberg, S.; Johnson, O.; Seckl, J.; Holst, J. J.; Ahrén, B. Impaired Incretin Response after a Mixed Meal Is Associated with Insuline Resistance in Nondiabetic Men. *Diabetes Care* **2001**, *24*, 1640–1645.

(61) Nauck, M. A.; Heimesaat, M. M.; Orskov, C.; Holst, J. J.; Ebert, R.; Creutzfeldt, W. Preserved Incretin Activity of Glucagon-like Peptide 1 [7-36 Amide] but Not of Synthetic Human Gastric Inhibitory Polypeptide in Patients with Type- 2 Diabetes Mellitus. *J. Clin. Invest.* **1993**, *91*, 301–307.

(62) Vilsbøll, T.; Krarup, T.; Madsbad, S.; Holst, J. J. Defective Amplification of the Late Phase Insulin Response to Glucose by Gip in Obese Type II Diabetic Patients. *Diabetologia* **2002**, *45*, 1111–1119.

(63) Deacon, C. F.; Johnsen, A. H.; Holst, J. J. Degradation of Glucagon-like Peptide-1 by Human Plasma in Vitro Yields an N-Terminally Truncated Peptide That Is a

Major Endogenous Metabolite in Vivo. *J. Clin. Endocrinol. Metab.* **1995**, *80*, 952–957.

(64) Deacon, C. F.; Plamboeck, A.; Møller, S.; Holst, J. J. GLP-1-(9-36) Amide Reduces Blood Glucose in Anesthetized Pigs by a Mechanism That Does Not Involve Insulin Secretion. *Am. J. Physiol. Endocrinol. Metab.* **2002**, *282*, E873-9.

(65) Eng, J.; Kleinman, W. A.; Singh, L.; Singh, G.; Raufman, J. P. Isolation and Characterization of Exendin-4, an Exendin-3 Analogue, from Heloderma Suspectum Venom: Further Evidence for an Exendin Receptor on Dispersed Acini from Guinea Pig Pancreas. *J. Biol. Chem.* **1992**, *267*, 7402–7405.

(66) Simonsen, L.; Holst, J. J.; Deacon, C. F. Exendin-4, but Not Glucagon-like Peptide-1, Is Cleared Exclusively by Glomerular Filtration in Anaesthetised Pigs. *Diabetologia* **2006**, *49*, 706–712.

(67) Amiram, M.; Luginbuhl, K. M.; Li, X.; Feinglos, M. N.; Chilkoti, A. A Depot-Forming Glucagon-like Peptide-1 Fusion Protein Reduces Blood Glucose for Five Days with a Single Injection. *J. Control. Release* **2013**, *172*, 144–151.

(68) Silverman, B. R.; Champion, J. A. Presentation of Fibronectin Fragments Using Affinity Protein Interactions for Enhanced Retention and Function. *Acta Biomater.* **2014**, *10*, 4956–4960.

(69) Yang, P.-Y.; Zou, H.; Chao, E.; Sherwood, L.; Nunez, V.; Keeney, M.; Ghartey-Tagoe, E.; Ding, Z.; Quirino, H.; Luo, X.; *et al.* Engineering a Long-Acting, Potent GLP-1 Analog for Microstructure-Based Transdermal Delivery. *Proc. Natl. Acad. Sci.* **2016**, *113*, 4140–4145.

(70) Huang, Y.; Chen, Z.; Chen, Y. Preparation and Characterization of a Novel Exendin-4 Human Serum Albumin Fusion Protein Expressed in Pichia Pastoris. *J. Pept. Sci.* **2008**, 588–595.

(71) Lee, S.; Lee, S.; Youn, Y. S.; Na, D. H.; Chae, S. Y.; Byun, Y.; Coon Lee, K. Synthesis , Characterization , and Pharmacokinetic Studies of PEGylated Glucagon-like Peptide-1. *Bioconjug. Chem.* **2005**, 377–382.

(72) Kim, H.; Lee, J.; Kim, T. H.; Lee, E. S.; Oh, K. T.; Lee, D. H.; Park, E. S.; Bae, Y. H.; Lee, K. C.; Youn, Y. S. Albumin-Coated Porous Hollow Poly(lactic-Co-Glycolic Acid) Microparticles Bound with Palmityl-Acylated Exendin-4 as a Long-Acting Inhalation Delivery System for the Treatment of Diabetes. *Pharm. Res.* **2011**, *28*, 2008–2019.

(73) Lim, S. M.; Eom, H. N.; Jiang, H. H.; Sohn, M.; Lee, K. C. Evaluation of PEGylated Exendin-4 Released from Poly (Lactic-Co-Glycolic Acid) Microspheres for Antidiabetic Therapy. *J. Pharm. Sci.* **2015**, *104*, 72–80.

(74) Vulic, K.; Shoichet, M. Affinity-Based Drug Delivery Systems for Tissue Repair

and Regeneration. *Biomacromolecules* **2014**, *15*, 3867–3880.

(75) Maxwell, D. J.; Hicks, B. C.; Parsons, S.; Sakiyama-Elbert, S. E. Development of Rationally Designed Affinity-Based Drug Delivery Systems. *Acta Biomater.* **2005**, *1*, 101–113.

(76) Kim, H. Y.; Hwang, J.-I.; Moon, M. J.; Seong, J. Y. A Novel Long-Acting Glucagon-Like Peptide-1 Agonist with Improved Efficacy in Insulin Secretion and β-Cell Growth. *Endocrinol. Metab. (Seoul, Korea)* **2014**, *29*, 320–327.

(77) Arya, A.; Yeng Looi, C.; Chuen Cheah, S.; Rais Mustafa, M.; Ali Mohd, M. Anti-Diabetic Effects of Centratherum Anthelminticum Seeds Methanolic Fraction on Pancreatic Cells, Beta-TC-6 and Its Alleviating Role in Type 2 Diabetic Rats. *J. Ethnopharmacol.* **2012**, *144*, 22–32.

(78) Crank, J. *The Mathematics of Diffusion*; Second.; Oxford University Press: Oxford, 1975.

(79) Saltzman, W. M.; Radomsky, M. L.; Whaley, K. J.; Cone, R. A. Antibody Diffusion in Human Cervical Mucus. *Biophys. J.* **1994**, *66*, 508–515.

(80) Miranda, L. P.; Winters, K. A.; Gegg, C. V; Patel, A.; Aral, J.; Long, J.; Zhang, J.; Diamond, S.; Guido, M.; Stanislaus, S.; *et al.* Design and Synthesis of Conformationally Constrained Glucagon-like Peptide-1 Derivatives with Increased Plasma Stability and Prolonged in Vivo Activity. *J. Med. Chem.* **2008**, *51*, 2758–2765.

(81) Kim, J.; Baggio, L. L.; Bridon, D. P.; Castaigne, J.; Robitaille, M. F.; Benquet, C.; Drucker, D. J. Development and Characterization of a Glucagon-Like Peptide 1-Albumin Conjugate: The Ability to Activate the Glucagon-like Peptide 1 Receptor in Vivo. *Diabetes* **2003**, *52*, 751–759.

(82) Pai, S. S.; Tilton, R. D.; Przybycien, T. M. Poly(ethylene Glycol)-Modified Proteins: Implications for Poly(lactide-Co-Glycolide)-Based Microsphere Delivery. *AAPS J.* **2009**, *11*, 88–98.

(83) Meyer, D. E.; Chilkoti, A. Protein Purification by Inverse Transition Cycling. In *Protein-Protein Interactions: A Molecular Cloning Manual*; 2002; pp. 329–344.

(84) Hassouneh, W.; Fischer, K.; MacEwan, S. R.; Branscheid, R.; Fu, C. L.; Liu, R.; Schmidt, M.; Chilkoti, A. Unexpected Multivalent Display of Proteins by Temperature Triggered Self-Assembly of Elastin-like Polypeptide Block Copolymers. *Biomacromolecules* **2012**, *13*, 1598–1605.

(85) Baggio, L. L.; Kim, J. G.; Drucker, D. J. Chronic Exposure to GLP-1R Agonists Promotes Homologous GLP-1 Receptor Desensitization in Vitro but Does Not Attenuate GLP-1R-Dependent Glucose Homeostasis in Vivo. *Diabetes* **2004**, *53*, 205–214.

(86) Jaques, F.; Jousset, H.; Tomas, A.; Prost, A. L.; Wollheim, C. B.; Irminger, J. C.; Demaurex, N.; Halban, P. A. Dual Effect of Cell-Cell Contact Disruption on Cytosolic Calcium and Insulin Secretion. *Endocrinology* **2008**, *149*, 2494–2505.

(87) Hectors, T. L. M.; Vanparys, C.; Pereira-Fernandes, A.; Martens, G. A.; Blust, R. Evaluation of the INS-1 832/13 Cell Line as a Beta-Cell Based Screening System to Assess Pollutant Effects on Beta-Cell Function. *PLoS One* **2013**, *8*, 1–10.

(88) Vulic, K.; Pakulska, M. M.; Sonthalia, R.; Ramachandran, A.; Shoichet, M. S. Mathematical Model Accurately Predicts Protein Release from an Affinity-Based Delivery System. *J. Control. Release* **2015**, *197*, 69–77.

(89) Moscarelli, P.; Boraldi, F.; Bochicchio, B.; Pepe, A.; Salvi, A. M.; Quaglino, D. Structural Characterization and Biological Properties of the Amyloidogenic Elastin-like Peptide (VGGVG)3. *Matrix Biol.* **2014**, *36*, 15–27.

(90) Li, N. K.; Quiroz, F. G.; Hall, C. K.; Chilkoti, A.; Yingling, Y. G. Molecular Description of the Lcst Behavior of an Elastin-like Polypeptide. *Biomacromolecules* **2014**, *15*, 3522–3530.

(91) Ye, F.; Baldursdottir, S.; Hvidt, S.; Jensen, H.; Larsen, S. W.; Yaghmur, A.; Larsen, C.; Østergaard, J. Role of Electrostatic Interactions on the Transport of Druglike Molecules in Hydrogel-Based Articular Cartilage Mimics: Implications for Drug Delivery. *Mol. Pharm.* **2016**, *13*, 819–828.

(92) Nie, T.; Baldwin, A.; Yamaguchi, N.; Kiick, K. L. Production of Heparin-Functionalized Hydrogels for the Development of Responsive and Controlled Growth Factor Delivery Systems. *J. Control. Release* **2007**, *122*, 287–296.

(93) Chung, Y.-I.; Tae, G.; Hong Yuk, S. A Facile Method to Prepare Heparin-Functionalized Nanoparticles for Controlled Release of Growth Factors. *Biomaterials* **2006**, *27*, 2621–2626.

(94) Zhang, Z.-Z.; Yang, S.-S.; Dou, H.; Mao, J.-F.; Li, K.-S. Expression, Purification, and C-Terminal Amidation of Recombinant Human Glucagon-like Peptide-1. *Protein Expr. Purif.* **2004**, *36*, 292–299.

(95) Yin, X.; Wei, D.; Yi, L.; Tao, X.; Ma, Y. Expression and Purification of Exendin-4, a GLP-1 Receptor Agonist, in Escherichia Coli. *Protein Expr. Purif.* **2005**, *41*, 259–265.

(96) King, W. J.; Toepke, M. W.; Murphy, W. L. Facile Formation of Dynamic Hydrogel Microspheres for Triggered Growth Factor Delivery. *Acta Biomater.* **2011**, *7*, 975–985.

(97) Gilroy, C. A.; Luginbuhl, K. M.; Chilkoti, A. Controlled Release of Biologics for the Treatment of Type 2 Diabetes. *J. Control. Release* **2016**, 1–13.

(98) Yin, D.; Lu, Y.; Zhang, H.; Zhang, G.; Zou, H.; Sun, D.; Zhong, Y. Preparation of Glucagon-like Peptide-1 Loaded PLGA Microspheres: Characterizations, Release Studies and Bioactivities in Vitro/in Vivo. *Chem. Pharm. Bull. (Tokyo)*. **2008**, *56*, 156–161.

(99) Choi, S.; Baudys, M.; Kim, S. W. Control of Blood Glucose by Novel GLP-1 Delivery Using Biodegradable Triblock Copolymer of PLGA-PEG-PLGA in Type 2 Diabetic Rats. *Pharm. Res.* **2004**, *21*, 827–831.

(100) Huotari, A.; Xu, W.; Mönkäre, J.; Kovalainen, M.; Herzig, K. H.; Lehto, V. P.; Järvinen, K. Effect of Surface Chemistry of Porous Silicon Microparticles on Glucagon-like Peptide-1 (GLP-1) Loading, Release and Biological Activity. *Int. J. Pharm.* **2013**, *454*, 67–73.

(101) Chilkoti, A.; Dreher, M. R.; Meyer, D. E. Design of Thermally Responsive, Recombinant Polypeptide Carriers for Targeted Drug Delivery. *Adv. Drug Deliv. Rev.* **2002**, *54*, 1093–1111.

(102) Amiram, M.; Luginbuhl, K. Injectable Protease-Operated Depots of Glucagon-like Peptide-1 Provide Extended and Tunable Glucose Control. *Proc. Natl. Acad. Sci.* **2013**, *110*, 2792–2797.

(103) Ho, Y. C.; Mi, F. L.; Sung, H. W.; Kuo, P. L. Heparin-Functionalized Chitosan-Alginate Scaffolds for Controlled Release of Growth Factor. *Int. J. Pharm.* **2009**, *376*, 69–75.

(104) Lee, J. S.; Go, D. H.; Bae, J. W.; Lee, S. J.; Park, K. D. Heparin Conjugated Polymeric Micelle for Long-Term Delivery of Basic Fibroblast Growth Factor. *J. Control. Release* **2007**, *117*, 204–209.

(105) Chung, H. J.; Kim, H. K.; Yoon, J. J.; Park, T. G. Heparin Immobilized Porous PLGA Microspheres for Angiogenic Growth Factor Delivery. *Pharm. Res.* **2006**, *23*, 1835–1841.

(106) Shih, H.; Lin, C. C. Photoclick Hydrogels Prepared from Functionalized Cyclodextrin and Poly(ethylene Glycol) for Drug Delivery and in Situ Cell Encapsulation. *Biomacromolecules* **2015**, *16*, 1915–1923.

(107) Wei, Q.; Sun, Y. Q.; Zhang, J. Exendin-4, a Glucagon-like Peptide-1 Receptor Agonist, Inhibits Cell Apoptosis Induced by Lipotoxicity in Pancreatic Beta-Cell Line. *Peptides* **2012**, *37*, 18–24.

(108) Skelin, M.; Rupnik, M.; Cencic, A. Pancreatic Beta Cell Lines and Their Applications in Diabetes Mellitus Research. *ALTEX* **2010**, *27*, 105–113.

(109) Masur, K.; Tibaduiza, E. C.; Chen, C.; Ligon, B.; Beinborn, M. Basal Receptor Activation by Locally Produced Glucagon-like Peptide-1 Contributes to Maintaining Beta-Cell Function. *Mol. Endocrinol.* **2005**, *19*, 1373–1382.

(110) Drucker, D. J.; Philippe, J.; Mojsov, S.; Chick, W. L.; Habener, J. F. Glucagon-like Peptide I Stimulates Insulin Gene Expression and Increases Cyclic AMP Levels in a Rat Islet Cell Line. *Proc. Natl. Acad. Sci. U. S. A.* **1987**, *84*, 3434–3438.

(111) Salic, A.; Mitchison, T. J. A Chemical Method for Fast and Sensitive Detection of DNA Synthesis in Vivo. *Proc. Natl. Acad. Sci. U. S. A.* **2008**, *105*, 2415–2420.

(112) Anderson, J. M.; Rodriguez, A.; Chang, D. T. Foreign Body Reaction to Biomaterials. *Semin Immunol* **2008**, *20*, 86–100.

(113) Zandstra, J.; Hiemstra, C.; Petersen, A. H.; Zuidema, J.; van Beuge, M. M.; Rodriguez, S.; Lathuile, A. A. R.; Veldhuis, G. J.; Steendam, R.; Bank, R. A.; *et al.* Microsphere Size Influences the Foreign Body Reaction. *Eur. Cells Mater.* **2014**, *28*, 335–347.

(114) Wei, Y.; Wang, Y.; Kang, A.; Wang, W.; Ho, S. V.; Gao, J.; Ma, G.; Su, Z. A Novel Sustained-Release Formulation of Recombinant Human Growth Hormone and Its Pharmacokinetic, Pharmacodynamic and Safety Profiles. *Mol. Pharm.* **2012**, *9*, 2039–2048.

(115) Aderem, A.; Underhill, D. Mechanisms of Phagocytosis in Macrophages. *Annu. Rev. Immunol.* **1999**, *17*, 593–623.

(116) Shukla, A.; Gulumian, M.; Hei, T. K.; Kamp, D.; Rahman, Q.; Mossman, B. T. Multiple Roles of Oxidants in the Pathogenesis of Asbestos-Induced Diseases. *Free Radic. Biol. Med.* **2003**, *34*, 1117–1129.

(117) Toyokuni, S. Role of Iron in Carcinogenesis: Cancer as a Ferrotoxic Disease. *Cancer Sci.* **2009**, *100*, 9–16.

(118) Wang, N. S.; Jaurand, M. C.; Magne, L.; Kheuang, L.; Pinchon, M. C.; Bignon, J. The Interactions between Asbestos Fibers and Metaphase Chromosomes of Rat Pleural Mesothelial Cells in Culture. A Scanning and Transmission Electron Microscopic Study. *Am. J. Pathol.* **1987**, *126*, 343–349.

(119) Ault, J. G.; Cole, R. W.; Jensen, C. G.; Jensen, L. C. W.; Bachert, L. A.; Reider, C. L. Behavior of Crocidolite Asbestos during Mitosis in Living Vertebrate Lung Epithelial Cells. *Cancer Res.* **1995**, *55*, 792–798.

(120) Donaldson, K.; Murphy, F. A.; Duffin, R.; Poland, C. A. Asbestos, Carbon Nanotubes and the Pleural Mesothelium: A Review of the Hypothesis Regarding the Role of Long Fibre Retention in the Parietal Pleura, Inflammation and Mesothelioma. *Part. Fibre Toxicol.* **2010**, *7*, 5.

(121) Zeidler-Erdely, P. C.; Calhoun, W. J.; Ameredes, B. T.; Clark, M. P.; Deye, G. J.; Baron, P.; Jones, W.; Blake, T.; Castranova, V. In Vitro Cytotoxicity of Manville Code 100 Glass Fibers: Effect of Fiber Length on Human Alveolar Macrophages. *Part. Fibre Toxicol.* **2006**, *3*, 5.

(122) Goodglick, L. A.; Kane, A. B. Cytotoxicity of Long and Short Crocidolite Asbestos Fibers in Vitro and in Vivo. *Cancer Res.* **1990**, *50*, 5153–5163.

(123) Schinwald, A.; Murphy, F. A.; Prina-Mello, A.; Poland, C. A.; Byrne, F.; Movia, D.; Glass, J. R.; Dickerson, J. C.; Schultz, D. A.; Jeffree, C. E.; *et al.* The Threshold Length for Fiber-Induced Acute Pleural Inflammation: Shedding Light on the Early Events in Asbestos-Induced Mesothelioma. *Toxicol. Sci.* **2012**, *128*, 461–470.

(124) Stanton, M. F.; Layard, M. W. Carcinogenicity of Natural and Man-Made Fibers. *Adv. Clin. Oncol.* **1978**, *1*, 181–187.

(125) Murphy, F. A.; Schinwald, A.; Poland, C. A.; Donaldson, K. The Mechanism of Pleural Inflammation by Long Carbon Nanotubes: Interaction of Long Fibres with Macrophages Stimulates Them to Amplify pro-Inflammatory Responses in Mesothelial Cells. *Part. Fibre Toxicol.* **2012**, *9*, 8.

(126) Miller, B. G.; Searl, A.; Davis, J. M. G.; Donaldson, K.; Cullen, R. T.; Bolton, R. E.; Buchanan, D.; Soutar, C. A. Influence of Fibre Length , Dissolution and Biopersistence on the Production of Mesothelioma in the Rat Peritoneal Cavity. *Ann. Occup. Hyg.* **1999**, *43*, 155–166.

(127) Donaldson, K.; Brown, G. M.; Brown, D. M.; Bolton, R. E.; Davis, J. M. Inflammation Generating Potential of Long and Short Fibre Amosite Asbestos Samples. *Br. J. Ind. Med.* **1989**, *46*, 271–276.

(128) Davis, J. M. G.; Addison, J.; Bolton, R. E.; Donaldson, K.; Jones, A. D.; Smith, T. The Pathogenicity of Long versus Short Fibre Samples of Amosite Asbestos Administered to Rats by Inhalation and Intraperitoneal Injection. *Br. J. Exp. Pathol.* **1986**, *67*, 415–430.

(129) Blake, T.; Castranova, V.; Schwegler-Berry, D.; Baron, P.; Deye, G. J.; Li, C.; Jones, W. Effect of Fiber Length on Glass Microfiber Cytotoxicity. *J. Toxicol. Environ. Health. A* **1998**, *54*, 243–259.

(130) Ye, J.; Shi, X.; Jones, W.; Rojanasakul, Y.; Cheng, N.; Schwegler-Berry, D.; Baron, P.; Deye, G. J.; Li, C.; Castranova, V. Critical Role of Glass Fiber Length in TNF-Alpha Production and Transcription Factor Activation in Macrophages. *Am. J. Physiol.* **1999**, *276*, 426–434.

(131) Donaldson, K.; Miller, B. G.; Sara, E.; Slight, J.; Brown, R. C. Asbestos Fibre Length-Dependent Detachment Injury to Alveolar Epithelial Cells in Vitro: Role of a Fibronectin-Binding Receptor. *Int. J. Exp. Pathol.* **1993**, *74*, 243–250.

(132) Mossman, B. T.; Lippmann, M.; Hesterberg, T. W.; Kelsey, K. T.; Barchowsky, A.; Bonner, J. C. Pulmonary Endpoints (Lung Carcinomas and Asbestosis) Following Inhalation Exposure to Asbestos. *J. Toxicol. Environ. Health. B. Crit. Rev.* **2011**, *14*, 76–121.

(133) Hansen, K.; Mossman, B. T. Generation of Superoxide (O2-) from Alveolar Macrophages Exposed to Asbestiform and Nonfibrous Particles. *Cancer Res.* **1987**, *47*, 1681–1686.

(134) Yang, H.; Bocchetta, M.; Kroczynska, B.; Elmishad, A. G.; Chen, Y.; Liu, Z.; Bubici, C.; Mossman, B. T.; Pass, H. I.; Testa, J. R.; *et al.* TNF-Alpha Inhibits Asbestos-Induced Cytotoxicity via a NF-kappaB-Dependent Pathway, a Possible Mechanism for Asbestos-Induced Oncogenesis. *Proc. Natl. Acad. Sci. U. S. A.* **2006**, *103*, 10397–10402.

(135) Philip, M.; Rowley, D. A.; Schreiber, H. Inflammation as a Tumor Promoter in Cancer Induction. *Semin. Cancer Biol.* **2004**, *14*, 433–439.

(136) Searl, A.; Buchanan, D.; Cullen, R. T.; Jones, A. D.; Miller, B. G.; Soutar, C. A. Biopersistence and Durability of Nine Mineral Fibre Types in Rat Lungs over 12 Months. *Ann. Occup. Hyg.* **1999**, *43*, 143–153.

(137) Davis, J. M. G. The Role of Clearance and Dissolution in Determining the Durability or Biopersistence of Mineral Fibers. *Environ. Health Perspect.* **1994**, *102*, 113–117.

(138) Morgan, A.; Holmes, A.; Davison, W. Clearance of Sized Glass Fibres from the Rat Lung and Their Solubility In Vivo. *Ann. Occup. Hyg.* **1982**, *25*, 317–331.

(139) Lippmann, M.; Yeates, D. B.; Albert, R. E. Deposition, Retention, and Clearance of Inhaled Particles. *Br. J. Ind. Med.* **1980**, *37*, 337–362.

(140) Cho, K. J.; Turkevich, L.; Miller, M.; McKay, R.; Grinshpun, S. A.; Ha, K.; Reponen, T. Penetration of Fiber versus Spherical Particles through Filter Media and Faceseal Leakage of N95 Filtering Facepiece Respirators with Cyclic Flow. *J. Occup. Environ. Hyg.* **2013**, *10*, 109–115.

(141) Ku, B. K.; Deye, G.; Turkevich, L. A. Characterization of a Vortex Shaking Method for Aerosolizing Fibers. *Aerosol Sci. Technol.* **2014**, *47*, 1293–1301.

(142) Ku, B.; Deye, G.; Turkevich, L. Efficacy of Screens in Removing Long Fibers from an Aerosol Stream--Sample Preparation Technique for Toxicology Studies. *Inhal. Toxicol.* **2014**, *26*, 70–83.

(143) Sohaebuddin, S. K.; Thevenot, P. T.; Baker, D.; Eaton, J. W.; Tang, L. Nanomaterial Cytotoxicity Is Composition, Size, and Cell Type Dependent. *Part. Fibre Toxicol.* **2010**, *7*, 22.

(144) Xu, A.; Zhou, H.; Yu, D. Z.; Hei, T. K. Mechanisms of the Genotoxicity of Crocidolite Asbestos in Mammalian Cells: Implication from Mutation Patterns Induced by Reactive Oxygen Species. *Environ. Health Perspect.* **2002**, *110*, 1003–1008.

(145) Müller, L.; Riediker, M.; Wick, P.; Mohr, M.; Gehr, P.; Rothen-Rutishauser, B. Oxidative Stress and Inflammation Response after Nanoparticle Exposure: Differences between Human Lung Cell Monocultures and an Advanced Three-Dimensional Model of the Human Epithelial Airways. *J. R. Soc. Interface* **2010**, *7*, 27–40.

(146) Huang, Z.-F.; Massey, J. B.; Via, D. P. Differential Regulation of Cyclooxygenase-2 (COX-2) mRNA Stability by Interleukin-1β (IL-1β) and Tumor Necrosis Factor-α (TNF-α) in Human in Vitro Differentiated Macrophages. *Biochem. Pharmacol.* **2000**, *59*, 187–194.

(147) Champion, J. A.; Mitragotri, S. Role of Target Geometry in Phagocytosis. *Proc. Natl. Acad. Sci. U. S. A.* **2006**, *103*, 4930–4934.

(148) Champion, J. A.; Walker, A.; Mitragotri, S. Role of Particle Size in Phagocytosis of Polymeric Microspheres. *Pharm. Res.* **2008**, *25*, 1815–1821.

(149) Mbawuike, I. N.; Herscowitz, H. B. MH-S, a Murine Alveolar Macrophage Cell Line: Morphological, Cytochemical, and Functional Characteristics. *J. Leukoc. Biol.* **1989**, *46*, 119–127.

(150) Matsunaga, K.; Klein, T. W.; Friedman, H.; Yamamoto, Y. Alveolar Macrophage Cell Line MH-S Is Valuable as an in Vitro Model for Legionella Pneumophila Infection. *Am. J. Respir. Cell Mol. Biol.* **2001**, *24*, 326–331.

(151) Bignon, J.; Saracci, R.; Touray, J. C. Introduction: INSERM-IARC-CNRS Workshop on Biopersistence of Respirable Synthetic Fibers and Minerals. *Environ. Health Perspect.* **1994**, *102*, 3–5.

(152) McDonald, J. C. Epidemiological Significance of Mineral Fiber Persistence in Human Lung Tissue. *Environ. Health Perspect.* **1994**, *102*, 221–224.

(153) Dodson, R. F.; Atkinson, M. A. L.; Levin, J. L. Asbestos Fiber Length as Related to Potential Pathogenicity: A Critical Review. *Am. J. Ind. Med.* **2003**, *44*, 291–297.

(154) Nagai, H.; Toyokuni, S. Biopersistent Fiber-Induced Inflammation and Carcinogenesis: Lessons Learned from Asbestos toward Safety of Fibrous Nanomaterials. *Arch. Biochem. Biophys.* **2010**, *502*, 1–7.

(155) Schinwald, A.; Chernova, T.; Donaldson, K. Use of Silver Nanowires to Determine Thresholds for Fibre Length-Dependent Pulmonary Inflammation and Inhibition of Macrophage Migration in Vitro. *Part. Fibre Toxicol.* **2012**, *9*, 47.

(156) McDonald, J. C.; Armstrong, B. G.; Edwards, C. W.; Gibbs, A. R.; Lloyd, H. M.; Pooley, F. D.; Ross, D. J.; Rudd, R. M. Case-Referent Survey of Young Adults with Mesothelioma: I. Lung Fibre Analyses. *Ann. Occup. Hyg.* **2001**, *45*, 519–523.

(157) Nagai, H.; Okazaki, Y.; Chew, S. H.; Misawa, N.; Yamashita, Y.; Akatsuka, S.;

Ishihara, T.; Yamashita, K.; Yoshikawa, Y.; Yasui, H.; *et al.* Diameter and Rigidity of Multiwalled Carbon Nanotubes Are Critical Factors in Mesothelial Injury and Carcinogenesis. *Proc. Natl. Acad. Sci. U. S. A.* **2011**, *108*, 1330–1338.

(158) Ray, P. D.; Huang, B. W.; Tsuji, Y. Reactive Oxygen Species (ROS) Homeostasis and Redox Regulation in Cellular Signaling. *Cell. Signal.* **2012**, *24*, 981–990.

(159) Kamp, D. W.; Weitzman, S. A. The Molecular Basis of Asbestos Induced Lung Injury. *Thorax* **1999**, *54*, 638–652.

(160) Mossman, B. T.; Churg, A. Mechanisms in the Patheogenesis of Asbestosis and Silicosis. *Am J Rep* **1998**, *157*, 1666–1689.

(161) Dostert, C.; Pétrilli, V.; Bruggen, R. Van; Steele, C.; Mossman, B. T.; Tschopp, J. Innate Immune Activation through Nalp3 Inflammasome Sensing of Asbestos and Silica. *Science (80-.).* **2008**, *320*, 674–677.

(162) Rhee, S. G. H2O2 , a Necessary Evil for Cell Signaling. *Science (80-.).* **2006**, *312*, 1882–1883.

(163) Morgan, M. J.; Liu, Z. Crosstalk of Reactive Oxygen Species and NF-κB Signaling. *Cell Res.* **2011**, *21*, 103–115.

(164) Manke, A.; Wang, L.; Rojanasakul, Y. Mechanisms of Nanoparticle-Induced Oxidative Stress and Toxicity. *Biomed Res. Int.* **2013**, *2013*, 1–15.

(165) Sharma, C. S.; Sarkar, S.; Periyakaruppan, A.; Barr, J.; Wise, K.; Thomas, R.; Wilson, B. L.; Ramesn, G. T. Single-Walled Carbon Nanotubes Induces Oxidative Stress in Rat Lung Epithelial Cells. *J Nanosci Nanotechnol* **2007**, *7*, 2466–2472.

(166) Brown, D. M.; Kinloch, I. A.; Bangert, U.; Windle, A. H.; Walter, D. M.; Walker, G. S.; Scotchford, C. A.; Donaldson, K.; Stone, V. An in Vitro Study of the Potential of Carbon Nanotubes and Nanofibres to Induce Inflammatory Mediators and Frustrated Phagocytosis. *Carbon N. Y.* **2007**, *45*, 1743–1756.

(167) Dinarello, C. A. Interleukin-1. *Cytokine Growth Factor Rev.* **1997**, *8*, 253–265.

(168) Arnoldussen, Y. J.; Skogstad, A.; Skaug, V.; Kasem, M.; Haugen, A.; Benker, N.; Weinbruch, S.; Apte, R. N.; Zienolddiny, S. Involvement of IL-1 Genes in the Cellular Responses to Carbon Nanotube Exposure. *Cytokine* **2015**, *73*, 128–137.

(169) Dong, J.; Porter, D. W.; Batteli, L. A.; Wolfarth, M. G.; Richardson, D. L.; Ma, Q. Pathologic and Molecular Profiling of Rapid-Onset Fibrosis and Inflammation Induced by Multi-Walled Carbon Nanotubes. *Arch. Toxicol.* **2015**, *89*, 621–633.

(170) Fettelschoss, A.; Kistowska, M.; LeibundGut-Landmann, S.; Beer, H.-D.; Johansen, P.; Senti, G.; Contassot, E.; Bachmann, M. F.; French, L. E.; Oxenius, A.; *et al.* Inflammasome Activation and IL-1β Target IL-1α for Secretion as

Opposed to Surface Expression. *Proc. Natl. Acad. Sci. U. S. A.* **2011**, *108*, 18055–18060.

(171) Gross, O.; Yazdi, A. S.; Thomas, C. J.; Masin, M.; Heinz, L. X.; Guarda, G.; Quadroni, M.; Drexler, S. K.; Tschopp, J. Inflammasome Activators Induce Interleukin-1α Secretion via Distinct Pathways with Differential Requirement for the Protease Function of Caspase-1. *Immunity* **2012**, *36*, 388–400.

(172) Palomäki, J.; Välimäki, E.; Sund, J.; Vippola, M.; Clausen, P. A.; Jensen, K. A.; Savolainen, K.; Matikainen, S.; Alenius, H. Long, Needle-like Carbon Nanotubes and Asbestos Activate the NLRP3 Inflammasome through a Similar Mechanism. *ACS Nano* **2011**, *5*, 6861–6870.

(173) Hillegass, J. M.; Miller, J. M.; MacPherson, M. B.; Westbom, C. M.; Sayan, M.; Thompson, J. K.; Macura, S. L.; Perkins, T. N.; Beuschel, S. L.; Alexeeva, V.; *et al.* Asbestos and Erionite Prime and Activate the NLRP3 Inflammasome That Stimulates Autocrine Cytokine Release in Human Mesothelial Cells. *Part. Fibre Toxicol.* **2013**, *10*, 39.

(174) Yazdi, A. S.; Guarda, G.; Riteau, N.; Drexler, S. K.; Tardivel, A.; Couillin, I.; Tschopp, J. Nanoparticles Activate the NLR Pyrin Domain Containing 3 (Nlrp3) Inflammasome and Cause Pulmonary Inflammation through Release of IL-1α and IL-1β. *Proc. Natl. Acad. Sci. U. S. A.* **2010**, *107*, 19449–19454.

(175) Schinwald, A.; Donaldson, K. Use of Back-Scatter Electron Signals to Visualise Cell/nanowires Interactions in Vitro and in Vivo; Frustrated Phagocytosis of Long Fibres in Macrophages and Compartmentalisation in Mesothelial Cells in Vivo. *Part. Fibre Toxicol.* **2012**, *9*, 34.

(176) Lee, J. K.; Sayers, B. C.; Chun, K.-S.; Lao, H.-C.; Shipley-Phillips, J. K.; Bonner, J. C.; Langenbach, R. Multi-Walled Carbon Nanotubes Induce COX-2 and iNOS Expression via MAP Kinase-Dependent and -Independent Mechanisms in Mouse RAW264.7 Macrophages. *Part. Fibre Toxicol.* **2012**, *9*, 14.

(177) Gilroy, D. W.; Colville-Ash, P. R.; Willis, D.; Chivers, J.; Paul-Clark, M. J.; Willoughby, D. A. Inducible Cyclooxygenase May Have Anti-Inflammatory Properties. **1999**, *5*, 10–13.

(178) Poligone, B.; Baldwin, A. S. Positive and Negative Regulation of NF-kappaB by COX-2: Roles of Different Prostaglandins. *J. Biol. Chem.* **2001**, *276*, 38658–38664.

(179) Krombach, F.; Münzing, S.; Allmeling, A. M.; Gerlach, J. T.; Behr, J.; Dörger, M. Cell Size of Alveolar Macrophages: An Interspecies Comparison. *Environ. Health Perspect.* **1997**, *105*, 1261–1263.